Università degli Studi dell'Insubria
Dipartimento di Scienza e Alta Tecnologia

Jets and accretion in heavy black holes across cosmic time

Dissertation submitted for the degree of

Philosophiæ Doctor

Ph.D. Candidate:

Tullia Sbarrato

Supervisors:

Dr. Gabriele Ghisellini
Dr. Paolo Padovani

Abstract

Blazars are Active Galactic Nuclei (AGN) characterized by relativistic jets launched in the vicinity of the central engine (i.e. a supermassive black hole; SMBH), that are oriented close to our line of sight.

How jets in AGN form, collimate and accelerate is still an open issue, but a connection with the accretion process is sometimes suggested. We first investigated this issue, finding that in jetted AGN the SMBH can accrete both through a radiatively efficient, optically thick, geometrically thin accretion disc, and through a radiatively inefficient, geometrically thick hot accretion flow. The occurrence of these two accretion regimes depends on the accretion rate: if it is larger than $\dot{M} \sim 0.1\dot{M}_{\rm Edd}$, the accretion is radiatively efficient, while if it is less than $\sim 0.1\dot{M}_{\rm Edd}$ the accretion is inefficient.

After this first insight on accretion and jets, we used these components as tools to study the extremely massive black hole population at high redshift (i.e. $M_{\rm BH} > 10^9 M_\odot$, $z > 4$). A deep knowledge of these objects can provide fundamental clues to the models of formation and growth of the first supermassive black holes ($10^6 M_\odot < M_{\rm BH} < 10^9 M_\odot$). The peculiar orientation of blazars makes them the most effective tracers of their parent population,

namely all the jetted AGN with similar intrinsic properties, but oriented in random directions. For this reason, we set up a systematic search of blazar candidates from a large quasar sample, in order to collect a complete sample of high–redshift blazars. We selected a sample of 19 extremely radio–loud, high–redshift quasars. We characterized their nuclear features (i.e. SMBH mass and accretion rate) by fitting their accretion disc spectra: we find that our criteria are efficient in selecting very massive and fast accreting black holes. We started our classification campaign, through X–ray observations. We successfully classified three quasars from our sample as blazars, along with a serendipitously selected (but analogous) candidate from the same area of sky. This means that our criteria are efficient in selecting good blazar candidates.

Comparing our findings with the known distribution of non–jetted AGN, we find that there are different formation epochs for extremely massive black holes hosted in jetted ($z \sim 4$) and non–jetted systems ($z \sim 2.5$). This is not easy to explain, according to the current black hole formation models in the early Universe. The search of very high–redshift jetted sources must be pursued, to learn more about the early stages of heavy black hole formation.

Contents

Abstract i

List of Figures v

List of Tables viii

1 Active Galactic Nuclei 1

1.1 AGN Structure: The Unified Model 2

1.2 Main classification 7

1.2.1 Blazars 10

2 SuperMassive Black Holes 17

2.1 Accretion on SMBHs 17

2.1.1 Radiatively efficient accretion disc 18

2.1.2 Advection Dominated Accretion Flow 21

2.2 $M_{\rm BH}$ measurement methods 26

2.2.1 $M_{\rm BH} - \sigma_*$ 28

2.2.2 Virial methods 31

2.2.3 Accretion Disc SED fitting 36

3 The jet–disc connection **45**

3.1 The sample 46

3.1.1 The blazar samples 47

3.1.2 The radio–galaxy sample 49

3.1.3 Deriving the BLR Luminosity 52

3.2 The $L_{\rm BLR}$–L_{γ} relation 53

3.3 The $L_{\rm BLR}$–$L_{\rm radio}$ relation 58

3.4 Unveiling the Change in Accretion 61

3.4.1 The importance of viewing angles 67

4 Finding blazars in the Early Universe **71**

4.1 Sample Selection 75

4.1.1 GROND observations and data analysis 80

4.2 The IR to optical SED: studying the accretion disc 83

4.2.1 The disc luminosity 85

4.2.2 Black Hole Mass Estimates 88

4.2.3 A first glance at the other high–z AGN 95

4.3 Classification of blazar candidates 98

4.3.1 B2 1023+25: the second most distant blazar known . . . 99

4.3.2 Three blazars in the $4 < z < 5$ redshift bin 117

5 SMBHs in the early Universe **127**

5.1 Blazars as tracers of all jetted AGN 128

5.1.1 A lack of misaligned jetted AGN? 131

5.2 Two formation epochs for SMBHs? 133

5.2.1 Jets and fast accretion 135

6 Conclusions **139**

A BL Lacs from Shaw et al. (2013) **143**

B SEDs of $z > 4$ blazar candidates **149**

List of Figures

1.1 Unified model of AGN 3

1.2 Blazar sequence 13

2.1 ADAF spectrum 22

2.2 Photo–ionizing and accretion luminosity as a function of accretion rate 24

2.3 $M_{\rm BH} - \sigma_*$ relation 30

2.4 Models of velocity–delay maps 34

2.5 SED of a multicolor black body spectrum 42

3.1 $L_{\rm BLR}$ vs. L_γ and $L_{\rm BLR}/L_{\rm Edd}$ vs. $L_\gamma/L_{\rm Edd}$ 54

3.2 $L_{\rm BLR}$ vs. $L_{\rm radio}$ 58

3.3 $L_{\rm BLR}/L_{\rm Edd}$ vs. $L_{\rm radio}/L_{\rm Edd}$ 62

3.4 $L_{\rm BLR}$ vs. $L_{\rm radio}$ over all the radio–detected quasars 68

4.1 Blazars as tracers of all jetted quasars 72

4.2 UV–Optical–IR SED of B2 1023+25 84

4.3 Comparison of our results with canonical $L_{\rm d}$ and $M_{\rm BH}$ estimates 87

4.4 Distribution of black hole masses in the sample of blazar candidates 91
4.5 Distribution of black hole masses in the SDSS quasar sample . . 94
4.6 Comparison between high–z radio–loud and radio–quiet AGN . 97
4.7 Comparison between B2 1023+25 and Q0906+6930 102
4.8 X–ray spectrum of B2 1023+25 109
4.9 B2 1023+25 broad–band SED 115
4.10 UV–optical–IR and broad–band SEDs of PMN J2134–0419 118
4.11 Broad–band SEDs of SDSS J142048.01+120545.9 and SDSS J222032.50+002537.5 121
4.12 UV–optical–IR and broad–band SEDs of PMN J2134–0419 122
4.13 Comparison of the classified candidates with known blazars . . . 124

5.1 Comoving number density of SMBHs with $M_{\rm BH} > 10^9 M_\odot$ 134
5.2 Black hole mass evolution with simple assumptions 136

A.1 Sources reclassified as FS 144
A.2 Sources reclassified as BL/FS 145
A.3 Sources reclassified as BL/FS 146
A.4 Sources reclassified as BL/FS and BL Lacs 147
A.5 Sources reclassified as BL Lacs 148

B.1 IR–optical–UV SEDs of $z > 4$ blazar candidates 150
B.2 IR–optical–UV SEDs of $z > 4$ blazar candidates 151
B.3 IR–optical–UV SEDs of $z > 4$ blazar candidates 152

List of Tables

3.1 Sources from Shaw et al. (2013), as reclassified in this work . . 50

3.2 Partial correlation analysis of $L_{\rm BLR} - L_\gamma$ and $L_{\rm BLR}/L_{\rm Edd} - L_\gamma/L_{\rm Edd}$ relations 55

4.1 Composition of SDSS DR7 Quasar Catalog 77

4.2 Sources from the DR7 Quasar Catalog with $z > 4$ and $R > 100$. 78

4.3 Sources from the DR7 Quasar Catalog with $z > 4$ and $R > 100$, with X–ray data 79

4.4 Log of GROND observations 81

4.5 Observed GROND magnitudes 82

4.6 Sample of blazar candidates, with $M_{\rm BH}$ estimates 89

4.7 B2 1023+25 GROND magnitudes 107

4.8 B2 1023+25 X–ray spectral analysis 108

4.9 Parameters used to model B2 1023+25 SED 113

4.10 XRT and UVOT observations of the three $4 < z < 5$ candidates . 119

4.11 Parameters of the SED modeling of the three $4 < z < 5$ sources . 120

1 Active Galactic Nuclei

The term **Active Galactic Nuclei** (**AGN**) generally refers to the highly energetic phenomena that can be observed in the nuclei of galaxies. This kind of emission largely exceeds the total luminosity emitted from its host galaxy, showing typical luminosities in the range $\sim 10^{44} - 10^{48}\,\mathrm{erg\,s^{-1}}$. The radiation emitted from these nuclear regions, moreover, can cover the whole electromagnetic spectrum, from radio wavelengths to very high–energies. These features definitely cannot be attributed to stellar emission.

The current paradigm ascribes this peculiar phenomena to the accretion process of matter onto a **SuperMassive Black Hole** (**SMBH**), residing at the center of the host galaxy, and that has a typical mass that ranges between 10^6 and $10^{10} M_\odot$. The energy emitted is thought to be produced by the gravitational infall of matter inside an accreting structure, that is heated to extremely high temperatures and dissipates the stored heath with different levels of efficiency (see Section 2.1). The huge energy release of this central accretion process then affects the environment and the matter in the immediate vicinity, that contribute to the emission over the whole electromagnetic spectrum. In this sense, the SMBH represent the “central engine" of the AGN emission.

About the 10% of AGN show intense radio–emission. For this reason, they

are classified as **radio–loud AGN**. The criterion traditionally followed in order to classify these objects refers to the ratio between the rest–frame radio ($\nu \sim$ 5GHz) and optical (blue band B) fluxes: $R \equiv F_{5\mathrm{GHz}}/F_B$. Specifically, an AGN is defined *radio–loud* when $R > 10$, otherwise it is classified as a *radio–quiet*. Such a strong radio emission is generally associated with the presence of a **relativistic jet**, that can have a size in a range from a few tens of kpc to Mpc (Begelman, Blandford & Rees 1984).

1.1 AGN Structure: The Unified Model

Originally, AGN were classified in many different groups on the basis of observations. Between the 70s and the 80s, there was a huge proliferation of phenomenological classes, that at the beginning were not connected to the same physical process. A large collection of spectroscopically different sources were studied as different objects. Later on, it was understood that most of the phenomenological differences can be ascribed to the different viewing angles under which we observe a single class of objects. This is the basic assumption on which the *unified model of AGN* is based. This model was summarized in the work by Urry & Padovani (1995). Another factor that strongly concurs to the different observational properties is the different accretion rate, as was found not long ago (Ghisellini et al. 2011; Trump et al. 2011). Chapter 3 widely details this point. According to the unification scheme (Figure 1.1), every AGN contains the structures described in the following, and the different viewing angles under which we observe the single objects are responsible for the strong observational differences among them.

SuperMassive Black Hole (SMBH) with the accretion structure. This system is the main engine of the whole AGN: the accretion process is thought

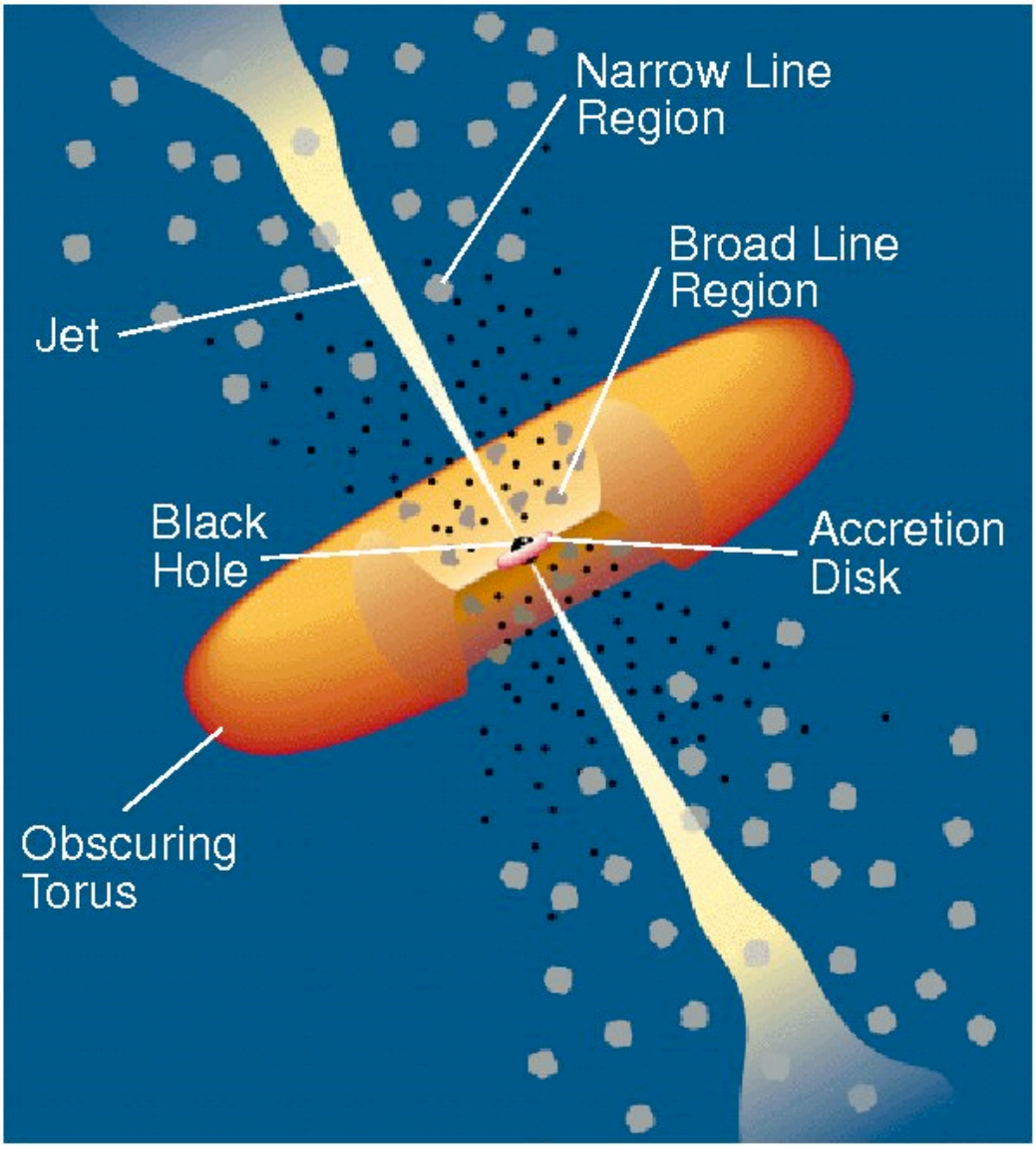

Figure 1.1: Cartoon that summarizes the unified model of AGN, described by Urry & Padovani (1995).

to be the main responsible for the overall emission. Many models have been proposed for the accretion process, describing both high– and low–accretion rate processes. We will detail some of these models in Section 2.1, but as a first raw description, at high accretion rates the most simple model is the Shakura & Sunyaev (1973) *geometrically thin, optically thick accretion disc*. According to this model, the matter is moving in quasi–Keplerian motion, induced by the SMBH gravitational force, and approaches the center of the disc by losing angular momentum thanks to turbulent motions and the presence of a magnetic field (later on modeled through magnetohydrodynamic processes).

Broad Line Region (BLR): this structure is formed by clouds of partially ionized plasma, with an electronic density $n \sim 10^9 \mathrm{cm}^{-3}$ and high orbital velocity ($v \sim 10^3 - 10^4 \,\mathrm{km\,s}^{-1}$). The plasma clouds that form this structure are in fact really close to the central black hole ($\sim 0.1 - 1$ pc), and therefore they are orbiting with a very high velocity around it. The plasma that forms this region produces broad emission lines by recombination, following the ionization from photons emitted mainly by the accretion structure. The efficiency of the ionization process clearly depends on the emission features of the accretion, and hence on its structure. The luminosity emitted from the BLR is hence a very good tracer of the ionizing luminosity of the accretion structure, and of its overall luminosity. The recombination lines are extremely broadened likely because of the high rotational velocity[1], and can be used to derive the plasma velocity itself, and the distance of the plasma clouds from the central engine. Radiation pressure and inclination could enhance (or decrease) the line broadening of a very small amount, but their contribution would not be

[1] Note that broadening due to infall or outflow motions is sometimes thought to contribute.

enough significant to be disentangled. Therefore, line width is mainly dependent on Doppler broadening.

Dusty Torus : obscuring dusty structure, not necessarily toroidal (contrary to what is suggested by the name). The distance of this structure (1–10 pc) from the central black hole allows the matter to be in dusty phase. By obscuring the optical emission from the innermost structures (i.e. BLR, accretion continuum emission) under some viewing angles, the torus is responsible of the different spectral features across the various AGN sub–classes. The broad emission lines produced by the plasma in the BLR, for example, can be completely obscured by the presence of this structure. The original unified model described this structure as an actual torus of dust, emitting in the IR wavelength range. This would mean that the presence or absence of broad emission lines could be directly linked with our viewing angle on the AGN. However, the most up–to–date models predict for this structure a different shape. The most discussed model describes a *clumpy* distribution of dust all around the nucleus (first introduced by Nenkova et al. 2002). This would ascribe the different spectral features also to the probability of a single clump of dust to be located along our line–of–sight. The obscuration would therefore be a statistical effect, linked to the possibility of finding a clump along the observer's line–of–sight. A number of models assume different distributions of the clumps, that could be not homogeneously spread all around the innermost parts of the AGN. These are the two most extreme hypotheses, but the most up–to–date models include a mixture of the two, with an anisotropic distribution of dusty clumps. This approach would still imply the dependence of the observed features on the viewing angle, along with a contribution from the probability to have the

clump along the observer's line–of–sight (see e.g. Stalevski et al. 2012).

Narrow Line Region (NLR): structure analogous to the BLR, formed by clouds of ionized plasma, but located at larger distance from the central black hole ($\sim$ 100pc). Compared to the BLR, the plasma density in this region is smaller ($n \sim 10^3 - 10^6 \mathrm{cm}^{-3}$), as is the velocity ($v \sim 100 - 500\,\mathrm{km\,s}^{-1}$). The smaller velocity can be easily derived from the definitely narrower emission lines emitted from the plasma in this region. Along with the different width, these lines can be clearly distinguished from those emitted by the BLR, because they include also "forbidden" lines, that can be produced only thanks to the lower–density conditions of the NLR itself, so that recombination can happen by spontaneous de–excitation, and not by collision events.

Relativistic Jet : it is present only in radio–loud AGN, and is responsible for their radio–loudness. The relativistic structure is formed by two relativistic ejections, a jet and a counterjet, emitted symmetrically with respect to the central AGN nucleus. The plasma inside the jets moves relativistically (Rees 1966), as can be inferred from the superluminal motion observed clearly in the collimated sections of these structures. Besides the relativistic *bulk* motion, the emitting plasma is relativistic also in the comoving frame of the jet. This allows it to emit at all frequencies, up to γ–rays. The main emission mechanisms are Inverse Compton (IC) and synchrotron emission. The IC process is responsible for the high–energy emission, while the lower–frequency emission (including the radio–emission) is ascribed to the synchrotron process. Jets extend up to Mpc scales, and usually terminate with extended structures called *lobes*, where the jets decelerate likely because of their interaction with

the surrounding matter. While the jet emission is highly anisotropic, because of relativistic beaming, the lobes emit a strong, isotropic radio–emission thanks to the plasma deceleration. The production mechanism of the relativistic jet is still unknown, and highly debated. The two main processes considered to be connected to the jet formation are the electromagnetic extraction of energy and angular momentum from an accretion disc (likely thanks to magnetic reconnection), and the extraction of rotational energy from the spinning SMBH (Blandford & Znajek 1977; Blandford & Payne 1982).

1.2 Main classification

Many classifications have been proposed from the first AGN discovered, and they were mainly based on observational differences. In fact, the viewing angle under which we observe an AGN highly affects its phenomenology. The emission from a relativistic jet is highly anisotropic because of relativistic beaming, and therefore its observed flux will be very different under different viewing angles. From another point of view, the presence of a dusty structure affects the optical emission. If the dust is located along our line–of–sight, the optical emission from the most central region will be partially or completely absorbed by the torus itself, and re–emitted in the IR. This affects also the spectral features in this wavelength range. For this reason, one of the first classifications introduced for AGN was indeed based on differences observed in the optical spectrum.

The first classification based on the optical spectra was made on a small set of spiral galaxies characterized by a bright core (Seyfert 1943): they are named **Seyfert galaxies**. Seyfert noticed the presence of deeply different sets

of emission lines in the optical spectra of these objects. In fact, they could be clearly divided in two different groups, depending on their optical spectral features: *Type 1* Seyfert galaxies show both broad and narrow emission lines, while *Type 2s* only the narrow components. Antonucci & Miller (1985) first showed in an extensive study of a Type 2 Seyfert galaxy that this could be an effect of different orientations. They performed spectropolarimetry observations of the bright Type 2 Seyfert NGC 1068. The polarized light coming from this source showed the broad emission lines that were missing from the total light spectrum. This led to the idea that all Seyferts were intrinsically equal, with the dusty torus intercepting the optical-UV continuum and the broad lines for large viewing angles. The broad emission lines are in fact emitted from a central region, and therefore can be absorbed by a dusty torus that surrounds the innermost AGN regions. This obscuring structure, though, cannot absorb the narrow emission lines, that are emitted by plasma located farther away from the centre. Therefore, Type 2 Seyfert galaxies could show only the narrow lines because we observe them under a line–of–sight that intercepts a dusty structure. In this case, there is the possibility that some fraction of the light emitted from the innermost region is scattered by free electrons in the direction of the observer. This scattered light would leave its signature in polarized light, as it happens in the case of NGC 1068. Later on, this same feature was found in many other Seyfert 2 galaxies, confirming the hypothesis about these sources (e.g. Miller & Goodrich 1986; Ward, Wright & Blanco 1988).

As already mentioned, AGN can be divided in *radio–loud* and *radio–quiet* AGN, according to the radio dominance over the optical emission. The radio luminosity is in fact mainly produced by the relativistic jet, while the optical emission comes from the accretion structure. In other words, the R parameter

used to parametrize the AGN radio–loudness, measures how much the radio emission dominates over the accretion luminosity. Therefore, radio–loud AGN are commonly associated with jetted sources.

The radio–loud AGN whose radio emission can be resolved were historically divided in two classes, according to the definition introduced by Fanaroff & Riley (1974). This was at first a merely morphological classification, based on the relative position of the hot spots on the radio map of a galaxy that showed radio emission, commonly called *radio–galaxy*. Fanaroff & Riley parametrized their classification using the ratio between the hotspot distance and the overall dimension of the AGN on its radio map. The objects with this parameter smaller than 0.5 are classified as FRI, while the others are FRII. Fanaroff & Riley found that this first morphological classification actually corresponds to a marked difference in the luminosities of these two classes. Observing the AGN at 178 MHz, in fact, all the FRI AGN have luminosities below the dividing value $L_{178\mathrm{MHz}} = 10^{25}\mathrm{W\,Hz^{-1}sr^{-1}}$, while the FRII lie above this threshold. The two classes show two different jet behaviors on the kpc scale: on that scale, in FRI jets the plasma seem to propagate more slowly than in FRII. From this point of view, no difference between the two classes seem to occur at parsec scale. Nevertheless, it is not clear at what distance the plasma deceleration happens. By repeating later this classification, it has been found that is not sharp, but radio–galaxies seem to be distributed continuously between the two classes.

Hypotheses that connected the different FRI/II features to the central engine (i.e. accretion) were introduced, to explain the observed differences. Specifically in the nineties, many spectral–based classifications were proposed, also comparing the emission line luminosities to the radio power, and trying to study the connection between the line emission and the jet luminosity (e.g.

Baum & Heckman 1989a,b; Rawlings et al. 1989; Rawlings & Saunders 1991; Morganti et al. 1997; Labiano 2008; Willott et al. 1999). Ghisellini & Celotti (2001) found that, along with the different jet features, FRI and FRII differ on the basis of their accretion efficiency. FRI were shown to have generally a lower accretion rate than FRII. Laing et al. (1994) introduced a sub–classification of FRII sources into high–excitation (HEG) and low–excitation galaxies (LEG), but this was found to be applicable also to some FRI. Therefore, Buttiglione et al. (2009; 2010) decided to perform an extended investigation of the spectroscopic properties of radio–galaxies, using a homogeneous sample. They found that all HEG are FRII, while LEG can be both FRI and FRII. While a ionization–based classification seems to be more physically relevant also in the case of radio–galaxies, an univocal, physically based classification method is not yet commonly accepted.

The radio–loud AGN whose radio emission cannot be resolved are classified as *radio compact objects*. The lack of extended emission is often ascribed to the peculiar orientation of the jet with respect to our line–of–sight, even though true compact objets have been observed. Those AGN that are thought to have their relativistic jets directed towards us are classified as **blazars**. Radio–galaxies are therefore thought to be the *parent population* of blazars.

1.2.1 Blazars

According to the current paradigm, **blazars** are radio–loud AGN characterized by a radio–compact nucleus and a pronounced variability at all frequencies. High optical and radio polarization is often observed in their emission. This, along with the extreme variability at all scales and the superluminal motion observed in the radio emission (Rees 1966; Gubbay et al. 1969), is considered a clear signature of the beaming of a relativistic jet, when observed along our

line–of–sight.

Blazars are generally divided in **Flat–Spectrum Radio Quasars** (**FSRQs**) and **BL Lacertae Objects** (**BL Lacs**). As generally happens with all kinds of AGN, blazars were classified on a purely observational basis. In fact, they are classified depending on the rest–frame equivalent width (EW) of their broad emission lines: BL Lacs have $EW < 5$Å, while FSRQs $EW > 5$Å (Urry & Padovani 1995). The EW–based classification, beside being easy to apply, could be ascribed to the different accretion mechanisms. The ionizing photons responsible for the broad line emission are produced by the accretion structure, and therefore a difference in the broad emission lines reflects a difference in the accretion luminosity. In the case of an efficient accretion (as the Shakura–Sunyaev disc), the BLR produces extremely luminous emission lines. On the other hand, a radiatively inefficient accretion mechanism would not induce the BLR to produce emission lines. Since the EW can be considered a good measure of the line emission dominance over the underlying continuum, the descriptive EW–based classification could correspond to a physical intrinsic difference between the two classes. FSRQs show strong emission lines, being therefore linked to a radiatively efficient accretion process, such as a Shakura–Sunyaev disc, while the lineless BL Lacs were connected to inefficient accretion, like the *Advection–Dominated Accretion Flow* (*ADAF*).

Nevertheless, there are many examples of BL Lacs that temporarily show faint emission lines in their optical spectra, along with FSRQs whose broad emission lines disappear or become fainter. This change can be so drastic for the single sources, to be able to change their EW–based classification. These dramatic changes in the EW are possible because the continuum measured is not produced by the same thermal emission that ionizes the BLR, but in that wavelength range is emitted from the jet. The jet emission shows a non–

simultaneous variability with respect to the nuclear emission (i.e. accretion and BLR). Therefore, during these variability events, an intrinsically efficiently accreting blazar can be disguised as a BL Lac because of a temporarily small EW. This clearly cannot be a physically reliable sub–classification.

In Ghisellini et al. (2011) and Sbarrato et al. (2012a), a different classification method was suggested. To follow the idea of a difference in the accretion mechanism, a different tracer for the accretion was chosen. Instead of using the broad emission line EW, a more reliable tracer is the BLR luminosity, derived from the luminosity of the single broad emission lines. The line luminosity is more reliable, since is a direct fraction of the luminosity emitted from the accretion structure, without being subject to the jet variability. From those two works, a more physical classification can be drawn: the FSRQs always have line luminosities that suggest an efficient accretion structure like the Shakura–Sunyaev standard accretion disc, while lines in BL Lacs have too small luminosities to be associated to an efficient disc. Specifically, FSRQs always have broad line luminosities $L_{\rm BLR}/L_{\rm Edd} \gtrsim 5 \times 10^{-4}$, corresponding to $L_{\rm d}/L_{\rm Edd} \gtrsim 0.005 - 0.01$, while BL Lacs are always below that value. Further discussion and a deeper study of this topic can be found in Chapter 3.

Spectral Energy Distribution of Blazars

Blazar emission is dominated by the non–thermal continuum component, i.e. the jet emission. This feature is clearly evident from the **Spectral Energy Distribution** (SED), that in these objects presents two characteristic prominent peaks. The first systematic analysis of the whole blazar spectrum has been performed by Fossati et al. (1998) and this analysis led to the definition of the **blazar sequence** (Figure 1.2). In their work, the authors constructed a set of averaged SEDs for 126 blazars, divided by radio–luminosity classes, regard-

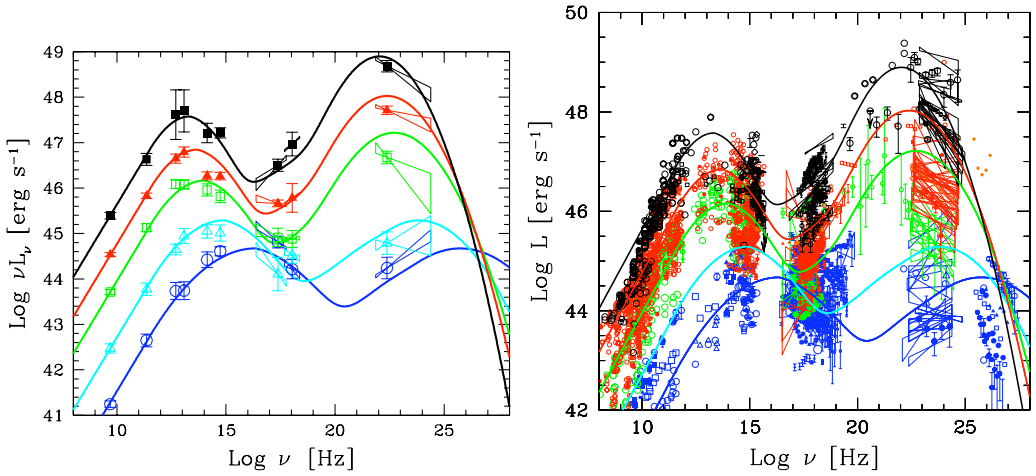

Figure 1.2: Representations of the blazar sequence by Fossati et al. (1998) and Donato et al. 2001. *Left panel:* the original blazar sequence drawn from the original sample of 126 blazars. The different colors are the different luminosity classes. *Right panel:* SEDs of the blazars detected by *Fermi*/LAT in the first 3 months of operation. Different colors indicates different γ–ray luminosities. The solid lines are the same as the left panel.

less the canonical classifications. The results show a homogeneus SED shape, characterized by two components, the first peaked at frequencies in the range $10^{13} - 10^{17}$ Hz, the second at about $10^{21} - 10^{24}$ Hz. The division based only on luminosity shows an evident trend: the most powerful sources have the peaks at lower energies, while low luminosity ones peak at much higher energies.

The high polarization degree of the emitted radiation suggests that the low energy component is produced by synchrotron process. Hence, the first peak likely traces synchrotron emissions. The wavelength of this first peak anticorrelates with the ratio of X–ray to radio flux. On this basis, Padovani & Giommi (1995) introduced a further classification among the BL Lacs. They divided them into *high–frequency peaked* (HBL) and *low–frequency peaked* (LBL) objects, according to wether α_{RX} (i.e. the broad band spectral index from 5 GHz to 1 keV) is < 0.75 or > 0.75, respectively.

On the other hand, the high energy photons are likely produced by Inverse Compton (IC) scatterings. Therefore, the second peak can be ascribed

to the IC emission. Different high–emission models have been introduced to justify this high–energy component. Most models agree on the fact that the IC scattering involves the same electronic population that is responsible for the synchrotron emission (one–zone leptonic models). Depending on which photon population is involved in the process, the models are divided in two classes: *Synchrotron–Self Compton* (SSC) and *External Compton* (EC) models. The SSC models connect directly synchrotron and IC emissions. It assumes that the photons scattered in the second process are part of the population emitted in the first (Maraschi et al. 1992). On the contrary, the EC models assume that the photons involved in the IC interactions come from the central zones of the AGN (i.e. directly from the accretion disc) or have been reprocessed in the BLR or the dusty torus. The two mechanisms are likely both present in blazars, maybe with different weight depending on which sub–class of blazar is considered. The FSRQs, indeed, show thermal components that can be the source of seed photons for the EC process. Hence in these objects there is likely an EC dominance. The absence of any evident thermal emission in BL Lacs suggests that in these objects there are less sources of external photons, to be used as seeds for the inverse Compton scattering process. Hence the γ–ray emission in BL Lacs is more likely produced by the SSC mechanism.

The blazar global emission is produced not only by the synchrotron and IC processes. All the elements included in the structure described according to the unified model make their own contribution, even though not dominating the bolometric luminosity. Hence, a complete model for the blazar SED has to take them into account.

The different combination of emission mechanisms that characterizes the blazar sub–classes leads to different SED shapes. Hence, one can expect to classify a blazar by modeling its SED and analysing its features. The al-

ready cited BL Lac classification introduced by Padovani & Giommi (1995) is based on this concept. The fundamental classification criteria are based on whether the synchrotron component or the high–energy peak dominate the global emission and on the X–ray spectral shape (see also Ghisellini et al. 2011).

FSRQ are those sources whose high–energy peak dominates the entire emission and where the X–ray spectrum belongs to the high–energy peak itself (i.e. the energy spectral index is $\alpha_x < 1$, where $F(\nu) \propto \nu^{-\alpha_x}$).

LBL have the high–energy and synchrotron peaks comparable in their luminosities and the X–ray belongs to the high–energy component.

IBL (i.e. intermediate BL Lacs; Padovani & Giommi 1995) have a peculiar X–ray spectrum shape. In the X–ray energy interval, indeed, the spectrum is steep at low frequencies and hardens at higher frequencies.

HBL have the X–ray emission dominated by the synchrotron component and present a steep X–ray spectrum.

2 SuperMassive Black Holes

2.1 Accretion on SMBHs

Different models have been proposed to describe the accretion of matter on black holes. They can be grouped in two different categories: *cold* and *hot* accretion flows, which correspond to accretion at high and low accretion rates, respectively.

Cold accretion flows consist of cool optically thick gas accreting in a disc–like geometry. The two most prominent examples are the standard *α–disc* that occurs at a consistent fraction of the Eddington mass accretion rate (Shakura & Sunyaev 1973; Novikov & Thorne 1973; Lynden–Bell & Pringle 1974), and the *slim disc* occurring at super–Eddington rates (Katz 1977; Begelman 1979; Begelman & Meier 1982; Abramowicz et al. 1988; Oshuga et al. 2005).

On the other hand, hot accretion flows are virially hot and optically thin. They occur at low mass accretion rates, and are generally characterized by lower radiative efficiency than the standard thin disc. Moreover, their radiative efficiency strongly decreases by decreasing the mass accretion rate. The thermal stability of these structures is generally guaranteed by energy advection. The most popular model for hot accretion flows is the *advection–*

dominated accretion flow (*ADAF*; Ichimaru 1977; Narayan & Yi 1994, 1995a, 1995b; Abramowicz et al. 1995; Chen et al. 1995). Another hypothesis, based on ion–electron decoupling in case of inflow with angular momentum, is the *ion–supported torus* (Rees et al. 1982), where ions remains at virial temperature, allowing electrons to cool via synchrotron and Compton processes.

2.1.1 Radiatively efficient accretion disc

Shakura & Sunyaev (1973) introduced for the first time an accretion model based on the formation of a disc around the black hole. Their model was firstly formulated to describe the accretion mechanism onto the compact objects in binary systems, but it can be extended to SMBHs in AGN. During accretion, matter is moving in a geometrically thin and optically thick disc. The plasma moves in Keplerian motion, and approaches the central black hole only if there is an efficient mechanism to transfer outwards the angular momentum. The magnetic field transport driven by the infalling matter, along with the turbulent motions of the matter itself, enable the angular momentum transfer. The authors parametrized this process with a generic α parameter, that names the model as α–disc. This parameter represents the efficiency of the angular momentum transfer itself. Viscosity processes are often invoked to simplify and explain the accretion process, but they are not a realistic description, since the matter is in a plasma state. Magnetohydrodynamics must be included in the model, to correctly describe the turbulent processes governing the accretion inside a disc (Balbus & Hawley 1991).

Matter can spiral towards the black hole with a Keplerian circular velocity, thanks to angular momentum transfer. This motion makes the system release gravitational energy, that turns into thermal energy and is radiated from the disc surface. Clearly, the total energy release and therefore the spectrum of

the emitted radiation are determined mainly by the mass accretion flow, i.e. the rate of matter inflow $\dot{M}$. Hence, the total disc luminosity $L_{\rm d}$ is given by the gravitational energy release through the relation:

$$L_{\rm d} = \eta \dot{M} c^2 \tag{2.1}$$

where η is the efficiency of the whole process. In the original formulation, Shakura & Sunyaev used $\eta \simeq 0.06$ (that descends from the assumption on the black hole, assumed to be a Schwarzschild black hole), but later formulations of the model claim slightly larger values, like $\eta \sim 0.08 - 0.1$. An upper critical luminosity is defined by the *Eddington luminosity* $L_{\rm Edd}$. This is the luminosity at which radiation pressure is intense enough to stop the gravitational infall, and therefore accretion itself (defined in spherical geometry). In this sense, the Eddington luminosity is generally assumed as an upper stability limit of the Shakura–Sunyaev disc.

$$L_{\rm Edd} = 1.3 \times 10^{38} \frac{M_{\rm BH}}{M_\odot} \ {\rm erg\,s^{-1}} \tag{2.2}$$

Corresponding to $L_{\rm Edd}$, an *Eddington accretion rate* can be defined as

$$\dot{M}_{\rm Edd} = \frac{L_{\rm Edd}}{c^2} \tag{2.3}$$

When $\dot{M} > \dot{M}_{\rm Edd}$, the accretion is defined *super–Eddington*. According to the original model, this represents a stability limit: no super–Eddington accretion is expected in the standard thin disc hypothesis. This accretion range, instead, is described by the *slim disc* model (Katz 1977; Begelman 1979; Begelman & Meier 1982; Abramowicz et al. 1988; Oshuga et al. 2005). According to these models, when $\dot{M}$ approaches and exceeds $\dot{M}_{\rm Edd}$, the accreting gas becomes too

optically thick to radiate all the dissipated energy locally. Therefore, radiation is trapped and transferred inwards with the accretion flow. This lowers the radiative efficiency, and therefore the disc luminosity becomes progressively smaller relative to the associated $\dot{M}$, instead of increasing linearly with the accretion rate as happens in the standard thin disc.

The spectrum emitted by a standard accretion disc has a very simple profile. Because of the density and the optical thickness of the plasma, each element of the disc emits as a black body. The temperature of each element is determined by its distance from the central black hole, and the closer to the black hole, the hotter the element is. Therefore, the most central regions of the disc are responsible for the most intense emission. The convolution of the black bodies with different temperatures and surface areas is a *multicolor black body* (for details, see Section 2.2.3). In the case of a black hole with a mass $M_{\rm BH} \sim 10^6 - 10^9 M_\odot$, the spectrum peaks in the UV–soft X range. Photons with this energy are the most efficient in the ionization of plasma with the same features as the BLR. The fraction of accretion luminosity that ionizes the plasma in the BLR, i.e. the photo–ionizing luminosity, $L_{\rm ion}$, depends on the geometry of the disc, and hence on its radiation efficiency. The covering factor of the plasma clouds forming the BLR with respect to the disc is thought to be $\sim 10\%$, hence this is the fraction of the radiation emitted by the disc that is intercepted and re–emitted through the broad emission lines (Baldwin & Netzer 1978; Smith et al. 1981). In other words, the emission from the BLR can be thought as:

$$L_{\rm BLR} = 10\%\, L_{\rm ion} \simeq 10\%\, L_{\rm d} \tag{2.4}$$

and therefore the luminosity emitted from the BLR is a very good tracer of the accretion luminosity.

2.1.2 Advection Dominated Accretion Flow

In the standard disc model, at very low accretion rates the particle density is so low that the energy exchange time scale between electrons and protons becomes larger than the accretion time scale. Most of the dissipated energy remains stored within the gas itself, and an effective radiating disc model is no more plausible. Following the original Shakura & Sunyaev hypothesis, the radiative disc model should occur only at accretion rate values larger than a critical value $\dot{m}_c$, i.e.

$$\dot{m} = \dot{M}/\dot{M}_{\rm Edd} > \dot{m}_c \tag{2.5}$$

where $\dot{M}_{\rm Edd} = L_{\rm Edd}/c^2$ and $\dot{m}_c \sim 0.1$ (Narayan & Yi 1995b). Another hypothesis for the critical value was introduced by Sharma et al. (2007). These authors suggested instead that the disc remains radiatively efficient for $\dot{m}_c \gtrsim 10^{-4}$. The accretion structure would change its dissipative features at much lower accretion rates than what expected in the original model.

Shapiro et al. (1976) first introduced a hot accretion flow model for the low accretion rate regime, where the plasma temperature is almost virial, while the gas is optically thin. The first mention to *advection* was advanced by Ichimaru (1977), who showed that the viscously dissipated accretion energy can heat the accretion flow rather than being radiated away, as happens in the case of a standard disc. This is the fundamental feature of the **Advection Dominated Accretion Flow** (**ADAF**; Narayan & Yi 1994, 1995a, 1995b; Abramowicz et al. 1995; Chen et al. 1995).

With the assumption of radiation pressure dominance, Narayan & Yi (1994) obtained a model with a definitely not disc–like morphology. The ADAF structure, indeed, is nearly spherical, and from this point of view is more similar to a Bondi accretion model (1952) than to a proper disc. Since

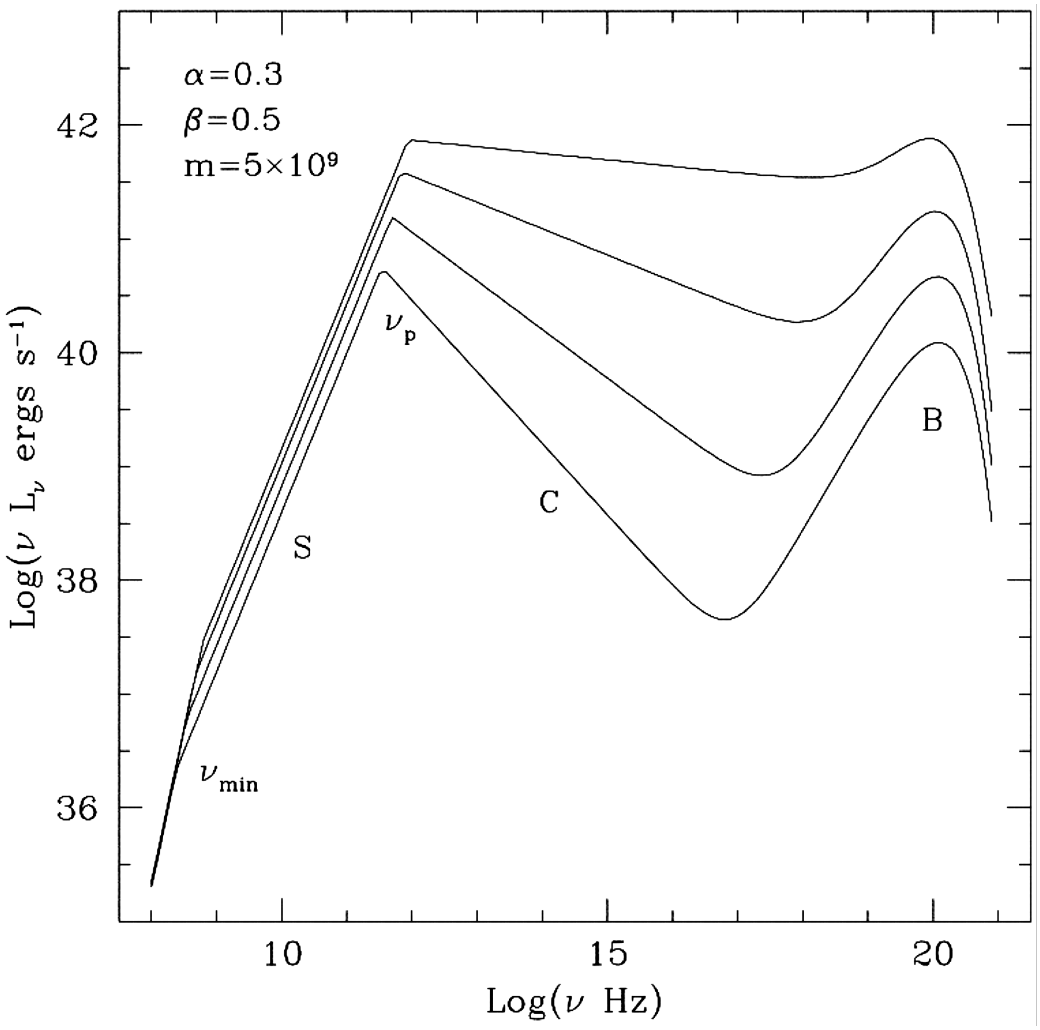

Figure 2.1: ADAF spectrum simulated by Mahadevan (1997). The three curves represent the model computed with three different accretion rates: the highest the accretion rate, the most luminous is the spectrum. The components emitted by the different processes are labelled: synchrotron (S), inverse Compton scattering (C) and bremsstrahlung (B).

the pressure is much larger than in a Shakura–Sunyaev disc, gravity is partially balanced and therefore the gas moves with a circular velocity extremely sub–Keplerian. The advection mechanism guarantees the motion of the matter towards the central black hole, allowing the accretion. The radial accretion velocity achieved through this mechanism is typically higher along the equatorial plane, where is concentrated the bulk of the accretion, and it is generally much larger than a standard thin disc.

As already mentioned, the process does not provide an effective cooling process, and the accretion energy is not radiated away, but it remains stored in the accreting gas. In other words, the system is highly underluminous relatively to its mass accretion rate. The emitted radiation is not a black body, because the hot gas is optically thin. Its emission is instead dominated by processes like synchrotron, bremsstrahlung and inverse Compton scattering. Mahadevan (1997) described for the first time the details of the emitted spectrum (see Figure 2.1) of an ADAF. The first peak of the spectrum is produced by synchrotron emission from thermal electrons. This emission is self–absorbed and is very sensitive to the electron temperature. Synchrotron photons are Compton–upscattered by the hot electrons, producing hard radiation. The importance of this Compton component depends on $\dot{m} = \dot{M}/\dot{M}_{\rm Edd}$: at high values of $\dot{m}$ it dominates the spectrum, but as $\dot{m}$ decreases it becomes softer and bolometrically weaker. At sufficiently low $\dot{m}$, the X–ray spectrum is dominated by the bremsstrahlung emission, since the inverse Compton component becomes less and less luminous and softer.

The dominant cooling process, therefore, strongly depends on the accretion rate. Under this condition, the radiation efficiency depends on the accretion rate too, instead of being just a fixed value. The exact value of the accretion efficiency depends on the electron heating. Unfortunately, there is

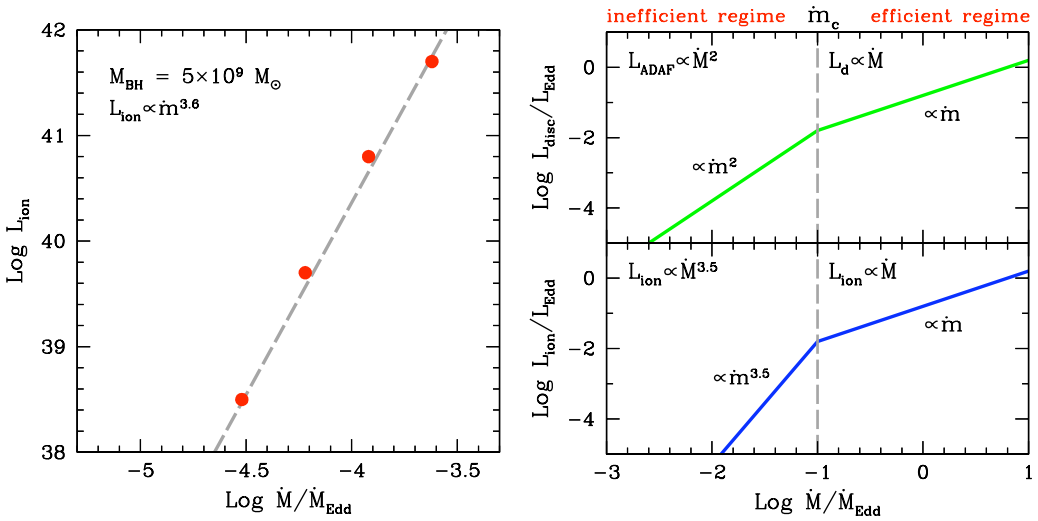

Figure 2.2: *Left:* The relation between the photo–ionizing luminosity $L_{\rm ion}$ and the accretion rate $\dot{m} = \dot{M}/\dot{M}_{\rm Edd}$, as derived from the work by Mahadevan (1997). The data points show the ionizing luminosities and accretion rates relative to the different spectra showed in the Figure 2.1. *Right:* Overall picture of accretion luminosity (upper panel) and ionizing luminosity (lower panel) as functions of the accretion rate. The break is fixed at $\dot{m}_{\rm c} = 0.1$ (i.e. $L_{\rm d}/L_{\rm Edd} = 10^{-2}$), following the standard model by Shakura & Sunyaev (1973). Note the different dependences of disc and ionizing luminosity in the inefficient accretion regime: $L_{\rm ion}$ has a steeper dependence on $\dot{m}$ than $L_{\rm ADAF}$.

no consensus on the exact heat content of electrons, yet. Simulations based on magnetic reconnection or on magnetohydrodynamic turbulence give different result, but the energy distribution of the hot electrons is still uncertain. According to Narayan, Garcia & McClintock (1997), the radiative efficiency should be directly proportional to the accretion rate itself, and therefore the overall emitted luminosity should be:

$$L_{\rm ADAF} = \eta \dot{M} c^2 \propto \dot{M}^2 c^2. \tag{2.6}$$

Therefore, an interesting issue to explore in the case of a hot accretion flow is the photo–ionizing luminosity that can be emitted. While in a standard thin disc the ionizing luminosity is always a fixed and relevant fraction of the overall disc luminosity (see Section 2.1.1), in the case of an ADAF the

shape of the emitted spectrum changes with the accretion rate. Studying the model proposed by Mahadevan (1997; Figure 2.1), and assuming that most of the ionizing luminosity is emitted in the UV–soft X range, the photo–ionizing luminosity scales with the accretion rate through the relation (Figure 2.2):

$$L_{\rm ion} \propto \left(\frac{\dot{M}}{\dot{M}_{\rm Edd}} \right)^{3.6} . \tag{2.7}$$

It is worth noticing that the ADAF structure is much less efficient in the BLR photo–ionization process with respect to a standard thin disc. In fact, while in the Shakura & Sunyaev model the photo–ionizing and the total luminosities are comparable, in this case the photo–ionization luminosity is only a small fraction of the total emission. This feature, along with the clear spectral change that occurs varying the accretion rate, has to provoke a sharp phenomenological change. In other words, if the photo–ionization of the BLR plasma is guaranteed mostly by the emissions from the accretion structure, a sharp change in the broad line luminosity behavior has to be expected (as can be seen in Figure 2.2, right panel).

2.2 $M_{\rm BH}$ measurement methods

Reliable estimates of supermassive black hole masses are getting easier thanks to the advent of suitable technology for high angular resolution spectroscopy and imaging. Reliable estimates of SMBH masses would allow to determine the mass function of this interesting class of black holes, and hence to understand their evolution, parallel to the evolution of their host galaxy population.

Masses of black holes in galaxies are generally measured by observing how they accelerate test masses in their vicinity. The same approach is valid for AGN. Test masses are usually stars or gas located in the nuclear regions. Both these cases have important advantages and disadvantages. Stellar dynamics has the advantage that stars respond to gravitational force only, therefore stellar motion is a direct tracer of SMBH gravitational potential. On the other hand, high angular resolution is required to resolve the black hole radius of influence. At higher distances, in fact, more matter contributes to the gravitational field tested through stars, and stellar motion is no more a good tracer of the SMBH gravitational potential. Gas dynamics, instead, do not require high angular resolution to be performed, since gas can be studied up to larger distances from the central engine. The disadvantage of this method, however, is that gas responds to other forces along with gravity, and therefore the modeling is more complicated.

In order to understand reliability and limits of all the various methods to estimate SMBH masses, a clear classification is necessary. The primary distinction that can be drawn is between *direct* and *indirect* methods.

Direct measurements are those where the mass is derived from the dynamics of stars or gas accelerated by the black hole itself, like just explained. Study of stellar and gas dynamics, along with reverberation mapping,

can be listed as direct measurements.

Indirect methods are based on observables that are correlated with the central black hole mass. This includes methods based on correlations between the black hole and its host galaxy properties, such as the well known connection with the velocity dispersion of bulge stars ($M_{\rm BH} - \sigma_*$; Ferrarese & Merritt 2000) or the relation between black hole and bulge luminosity (Kormendy & Richstone 1995; Magorrian et al. 1998). The BLR radius–luminosity relationship (Kaspi et al. 2000) found specifically for AGN is an indirect method, too.

Another common classification is based on the number of assumption required and on how much a method relies on different models to be calibrated. According to this distinction, mass measurements can be divided in *primary* and *secondary* methods. Primary methods require fewer assumptions, and have almost no model dependence. Good examples of primary methods are those based on dynamics of individual sources, such as the most accurately measured mass, i.e. the black hole in Sgr A* at the Galactic Center, based on proper motions and radial velocities of individual stars (e.g. Genzel et al. 2010; Meyer et al. 2012). Another remarkable primary method is the study of proper motions and radiative velocities of megamasers around the central black hole, like in the case of NGC 4258 (Miyoshi et al. 1995). A good example of secondary mass measurement method is reverberation mapping, since it relies on other methods to fix a zero point of the mass scale. This is a good example of how a mass measurement method can be a direct but secondary method.

In the following, I will detail two of the most classical approaches to black hole mass measurements, the $M_{\rm BH} - \sigma_*$ relation and the virial methods, along

with the method that was used for this work, i.e. the direct fitting of the accretion disc emission.

2.2.1 $M_{\rm BH} - \sigma_*$

In order to study the relation between the central black hole and its host galaxy, Ferrarese & Merritt (2000) derived a crucial relation between $M_{\rm BH}$ and the stellar velocity dispersion (σ_*) in the host bulge or elliptical galaxy. They found a remarkable correlation, that according to the original paper has the form:

$$\mathrm{Log}\left(\frac{M_{BH}}{M_\odot}\right) = (4.80 \pm 0.54)\,\mathrm{Log}\left(\frac{\sigma_*}{\mathrm{km\,s^{-1}}}\right) - (2.9 \pm 1.3) \qquad (2.8)$$

The sample used to derive this correlation has masses obtained through gas kinematics and water maser studies, along with the proper motion measurements in the SgrA* area (Genzel et al. 2000)[1]. To homogenize the mass measures, and specifically to avoid biases in the velocity measurements possibly due to methodological errors, two different methods were used to estimate the velocity dispersion. The main method was the direct measure of the *central velocity dispersion* (σ_c) of stars, measured in an aperture of few arcseconds in diameter. Ferrarese & Merritt obtained these values from literature. Therefore, to bring all the values to a consistent and common system, the authors normalized all the velocity dispersions to an equivalent aperture radius of $r_e/8$, where r_e is the effective radius of the galaxy or bulge (in case of elliptical or spiral galaxies, respectively), i.e. the radius inside which half of the total light observed in the galaxy (or bulge) is emitted. The other method that was used to estimate the velocity dispersion was the measurement of the *rms velocity* at

[1] As already pointed out, these are the most reliable measures of a black hole mass, and also at the time of the $M_{\rm BH} - \sigma_*$ derivation they were the most reliable.

a fixed distance $r_e/4$ from the centre of the galaxy. The rms velocity is defined as $v_{rms} = \left[\left(\sigma^2 + {}^{v_r^2}/_{\sin^2 i}\right)_{r_e/4}\right]^{1/2}$, where σ and v_r are the measured stellar velocity dispersion and the mean line–of–sight velocity, respectively. The angle i is defined as the inclination angle between the rotation axis and the line–of–sight itself. This method has the clear advantage of avoiding possible issues deriving from the aperture corrections, instead necessary to homogenize σ_c. On the other hand, the estimate of the inclination angle i is still not easy. A wrong estimate of this parameter would increase the scatter in the $M_{\rm BH} - \sigma_*$ relation and bias its slope.

It is worth noticing that the results obtained through these two different methods are consistent. Specifically, the slopes in the $M_{\rm BH} - \sigma_*$ relations are consistent whether v_{rms} or σ_c is used (see Figure 2.3). The consistency of the two slopes suggests that the tight relation between $M_{\rm BH}$ and σ_* is not merely a trace of the black hole influence on stellar kinematics of the nucleus. In fact, the rms velocity is measured well beyond the influence radius of the central black hole. Therefore, in that case the stellar dynamics is not influenced only by the gravitational field from the central black hole. Whether the $M_{\rm BH} - \sigma_*$ relation is driven by the direct gravitational influence of the black hole or not, this does not affect the usefulness of the relation itself, since it actually is a good predictor of $M_{\rm BH}$.

If the correlation is not due to the direct gravitational influence of the black hole, a possible explanation of such a tight correlation could be connected to a fundamental connection between the black hole itself and the bulge mass. Indeed, scaling relationships between mass and luminosity of early–type galaxies had already been suggested, such as the relation $M_{\rm BH} \sim L^{5/4}$ by Faber et al. (1987). This relation, together with the Faber–Jackson (1976) relation between luminosity and velocity dispersion $L \sim \sigma_*^4$, provides a scaling $M_{\rm BH} \sim \sigma_*^5$,

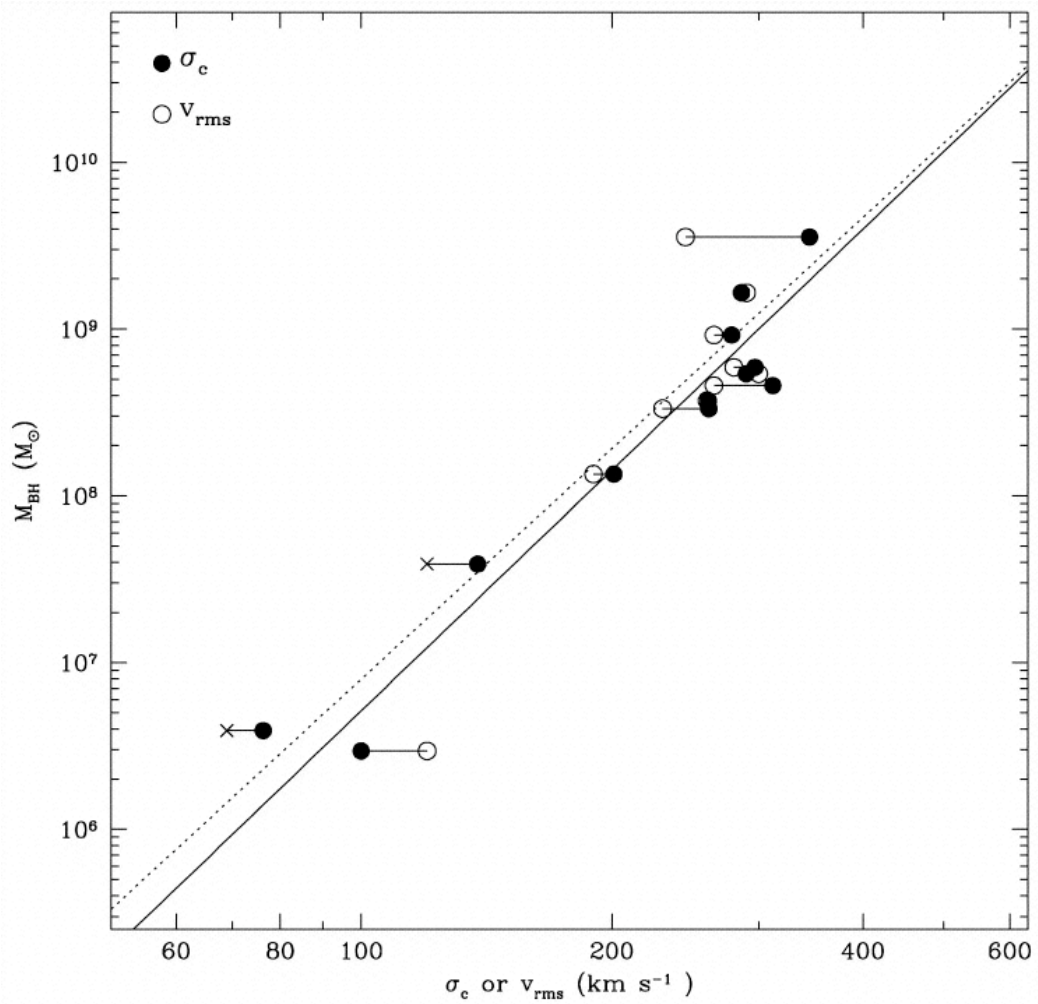

Figure 2.3: The $M_{\rm BH} - \sigma_*$ relation from the paper by Ferrarese & Merritt (2000). Filled circles represent values of σ_* derived from central velocity dispersion σ_c. Open circles indicate the ones obtained from rms velocity v_{rms}, while crosses indicate lower limits on rms velocity derivations. Solid and dashed lines are the best linear fits obtained using σ_c and v_{rms} respectively. Note that the correlations obtained with the two different velocity measures are consistent.

to be compared with the $M_{\rm BH} - \sigma_*$ relation itself. This is a clear hint that the relation introduced by Ferrarese & Merritt is a consequence of a deeper connection between the black hole and the bulge of its host. In any case, the relation

$$M \propto \sigma_*^{\alpha} \quad \text{with} \quad \alpha = 4.8 \pm 0.5 \tag{2.9}$$

is an excellent predictor of central black hole mass in AGN. This method, indeed, allows one to predict $M_{\rm BH}$ with an accuracy of $\sim 30\%$ or better from a single observation of a galaxy's velocity dispersion. Note however that deviations from the correlation have lately been found at very low and high black hole masses. The most extreme objects seem not to follow this relation. While the reasons of these discrepancies are under investigation, it is still true that this method statistically gives reliable estimates of $M_{\rm BH}$.

2.2.2 Virial methods

A widely used method to measure black hole masses in AGN is based on the *virial theorem*. This method is based on the assumption that the BLR dynamics are dominated by the central black hole mass, and therefore the "virial relationship" is valid:

$$M_{\rm BH} = f \left[\frac{(\Delta V)^2 R_{\rm BLR}}{G} \right] \tag{2.10}$$

where ΔV is the broad emission line width. To get a proper black hole mass estimate, however, it is necessary to trace $R_{\rm BLR}$ through an observable. This is possible by studying how the broad emission lines react to variations in the ionizing continuum. The line emitted from the BLR, in fact, reverberate to variations of the continuum emitted from the accretion disc. On this interesting AGN feature is based a black hole mass measurement method, i.e. the *reverberation mapping*.

Reverberation Mapping

Short time–scale variations in the continuum emission in AGN were observed since the early times of the discovery of quasars, but it was not until the 1980s that a strong connection between continuum and emission–line variability was established (e.g. Antonucci & Cohen 1983; Peterson et al. 1983; Ulrich et al. 1991). The first mathematical formalism was introduced by Blandford & McKee (1982), that first probed the emission line region structure by variability. Reverberation mapping is indeed a method to obtain estimate for the BLR size and the central black hole mass from the time–delayed response of the broad emission lines to continuum variations. Two observables are required in order to perform this analysis, the *emission time delay* response (τ) of the emission lines with respect to the continuum variations, and the *emission line width* (ΔV). Reverberation–based studies performed up to now show some important features about these two observables, and allow to draw important conclusions about BLR structure and dynamics (see for review Peterson 2014 and references therein):

- the emission lines respond rapidly to continuum changes, meaning that the BLR is small (because the light–travel time is short) and that the gas density in this region is high, i.e. the recombination time is shorter than the light–travel time itself. Moreover, the BLR dynamical timescale is much longer than the reverberation timescale, so the BLR is essentially stationary for reverberation mapping purposes.

- different emission lines have different response time–scales. Specifically, lines produced by higher ionization states respond first. This is an evidence for a stratified structure of the BLR. In fact, the response time–scale defines the distance of the plasma emitting the line, and the *size*

of the BLR can be inferred from each emission line time delay to be $R_{\rm BLR} = c\tau$.

- if the time delay is measured for multiple emission lines in a single source, a tight correlation is observed between ΔV and τ. From this relationship a constant product $(\Delta V)^2\tau$ is observed. This correspond to the **constant virial product** $(\Delta V)^2 R_{\rm BLR}$ expected from a BLR dynamics dominated by the SMBH gravitational potential. Note however that one could say more generally that the BLR responds to an inverse square force, or forces. In this view, a contribution from radiation pressure cannot be excluded (Marconi et al. 2008).

- the time delay between line and continuum variations is longer for more luminous objects. This suggests a strong relationship between the source luminosity and the size of the BLR. In fact, it was shown that the BLR size and the AGN continuum luminosity actually follow the relation $R_{BLR} \propto L_{\rm cont}^{1/2}$ (Bentz et al. 2006).

These results provide the possibility to estimate the mass enclosed in the BLR size $R_{\rm BLR} = c\tau$, that is clearly dominated by the central black hole mass. In fact, from the virial theorem already introduced, it can be obtained the relation:

$$M_{\rm BH} = f\left[\frac{(\Delta V)^2 c\tau}{G}\right]. \tag{2.11}$$

The dimensionless parameter f parametrizes the BLR intrinsic features, such as its structure, dynamics and orientation. Extremely detailed reverberation mapping programs can provide enough details to infer hypotheses on the BLR geometry and dynamics of a single source. According to simulations, the velocity–delay maps provided by reverberation mapping has extremely differ-

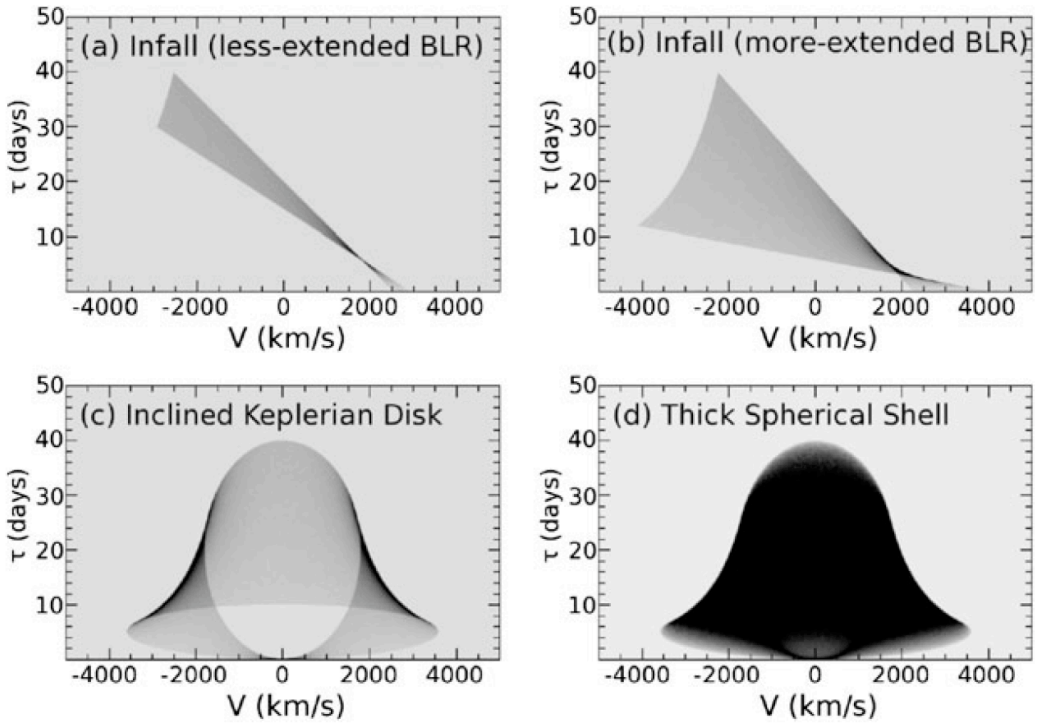

Figure 2.4: Toy models of velocity–delay maps from the review by Peterson (2014). *Top:* BLR in spherical infall, with different sizes (less extended on the left, more extended on the right). *Bottom left:* BLR clouds in motion along a Keplerian disc–like orbit. *Bottom right:* BLR clouds disposed in a spherical shell with Keplerian motion.

ent shapes depending on BLR specific features (see Figure 2.4). Nevertheless, reverberation mapping results with enough quality to detail these features are still few. An average value for f can be inferred by comparing reverberation mapping values of $M_{\rm BH}$ with independent estimates, obtained with different methods. A value of $\langle f \rangle \sim 5$ is commonly accepted in the latest studies (Onken et al. 2004; Park et al. 2012). The most recent analysis yields a value $\langle f \rangle = 5.25 \pm 1.21$ (Woo et al. 2010). It is worth pointing out, anyway, that this factor has a very specific value for each AGN, even if the small availability of data can only provide an average value up to now.

Single–epoch spectrum method

One of the main results of the reverberation mapping campaigns is the discovery of a tight correlation between BLR radius and AGN continuum luminosity:

$$R_{\rm BLR} \propto L_{\rm cont}^{\alpha} \quad \text{with} \quad \alpha \approx 0.5. \tag{2.12}$$

Note that this relation is consistent with a theoretical expectation deriving from photo–ionization models (see e.g. Davidson 1972; Ferland & Mushotzky 1982). Each photo–ionization model can in fact be parametrized by the shape of the continuum, the density of the ionized gas n_H, the elemental abundances and a photo–ionization parameter defined as:

$$U = \frac{Q(H)}{4\pi R^2 c\, n_H} \quad \text{with} \quad Q(H) = \int_0^{\infty} \frac{L_\nu}{h\nu}\, \mathrm{d}\nu \tag{2.13}$$

where $Q(H)$ is the number of ionizing photons produced per second by the ionizing source, and R is the distance between the photo–ionizing source and the ionized matter (in the case of broad line region $R \equiv R_{BLR}$). The similarity of AGN spectra over many orders of magnitude in luminosity suggests that U and n_H are approximately the same for all AGN. Assuming that $L_{\rm cont} \simeq L_{\rm ion} \propto Q(H)$, this leads to the theoretical prediction:

$$R_{BLR} = \left[\frac{Q(H)}{4\pi c\, n_H U}\right]^{1/2} \propto L_{\rm cont}^{1/2}. \tag{2.14}$$

This is consistent with the radius–luminosity relation obtained from reverberation mapping. Nevertheless, it must be kept in mind that the theoretical prediction is based on very simple assumptions, while up to now there is no self–consistent model of the BLR. However, this naïve prediction has been confirmed by observational results, that show remarkably consistent results (Kaspi

et al. 2000; Bentz et al. 2006).

The $R-L$ relation is now the basis of an easy method to estimate an AGN black hole mass, the *single epoch spectrum method*. In fact, once the continuum luminosity of an AGN has been measured, it is possible to infer the BLR radius through the $R-L$ relation. This can be combined with the broad emission line width in the virial product, in order to obtain an estimate of the black hole mass:

$$M_{\rm BH} = f\left[\frac{(\Delta V)^2 R_{BLR}}{G}\right] \propto f\left[\frac{(\Delta V)^2 L_{\rm cont}^{1/2}}{G}\right]. \tag{2.15}$$

where the full width at half maximum (FWHM) of the broad emission line can be used as ΔV. This method is referred to as the single–epoch spectrum method, since it is possible to obtain a reliable estimate of $M_{\rm BH}$ from a single spectrum. The strongest advantage of this method is that it is remarkably less difficult and time–consuming than the large reverberation mapping campaigns.

Note however that both reverberation mapping studies and virial methods are only calibrated in the local Universe, i.e. at low redshift, and on small samples. Reverberation mapping is too time–consuming to be performed on high–redshift objects. Virial methods are instead commonly used to measure black hole masses at any redshift, but they were probed only on small samples. Further calibrations would be needed.

2.2.3 Accretion Disc SED fitting

In those objects in which the accretion mechanism is most likely a Shakura–Sunyaev thin disc, the disc emission can be clearly visible at optical frequencies as long as it dominates over the synchrotron component. This feature can be used to model the disc emission and obtain direct measures of defining

quantities, such as the disc luminosity (linked to the accretion rate) and the black hole mass (e.g. Calderone et al. 2013). A detailed model for the SED emitted from the disc is needed.

In Section 2.1.1, the optically thick geometrically thin accretion disc introduced by Shakura & Sunyaev (1973) is described in details. Because of the density and optical depth of this accretion structure, each emitting element of a Shakura–Sunyaev accretion disc emits as a black body. The detailed shape of a model that describes a *multicolor black body* spectrum can be obtained through the convolution of the single black body spectra emitted at different temperatures and distances from the central black hole. The black body emission is described by the Planck spectrum:

$$B_\nu \, \mathrm{d}\nu = \frac{2h\nu^3}{c^2} \frac{\mathrm{d}\nu}{e^{\frac{h\nu}{kT}} - 1} \tag{2.16}$$

where h is the Planck's constant, k is the Boltzmann constant and c is the speed of light. For each emitting element, the temperature T is a function of the distance from the central black hole (R) through the mass of the black hole ($M_{\rm BH}$) and the accretion rate on it ($\dot{M}$). The dependence of T from the distance R can be obtained from the relation, that is described for example in Frank, King & Raine (1985):

$$T = T(R; M_{\rm BH}, \dot{M}) = \left\{ \frac{3G}{8\pi\sigma} \frac{M_{\rm BH}\dot{M}}{R^3} \left[1 - \left(\frac{R_{\rm in}}{R} \right)^{1/2} \right] \right\}^{1/4} \tag{2.17}$$

where G is the gravitational constant, σ the Stefan–Boltzmann radiative constant and $R_{\rm in}$ is the inner radius of the disc. In order to define the innermost disc radius, it is worth introducing the *Innermost Stable Circular Orbit* (ISCO), i.e. the nearest point to the central black hole on which the matter can follow a stable orbit. This radius is generally thought to define the innermost disc

radius ($R_{\rm in} = R_{\rm ISCO}$). Assuming a Schwarzschild metric to describe the immediate black hole surroundings, i.e. assuming a non–rotating black hole, the ISCO is fixed at three times the Schwarzschild radius ($R_{\rm S}$):

$$R_{\rm in} = R_{\rm ISCO} = 3\,R_{\rm S} = 3\,\frac{2\,G M_{\rm BH}}{c^2} \tag{2.18}$$

Assuming a different black hole metric, such as a Kerr geometry in case of a spinning black hole, the ISCO would have a different value, that in the maximally spinning cases is $R_{\rm ISCO} = R_{\rm S}/2$ if the disc and the black hole are corotating, and $R_{\rm ISCO} = 9R_{\rm S}/2$ if they are counterrotating. For our purposes, in the following we will always assume a Schwarzschild metric.

The relation of the temperature in each emitting element with its distance from the black hole and with the black hole mass defines the dependence of each Planck spectrum from R and M_{BH}:

$$B_\nu[T(R;\,M_{\rm BH},\dot{M})]\,{\rm d}\nu = \frac{2h\nu^3}{c^2}\,\frac{{\rm d}\nu}{\exp\left(\frac{h\nu}{k\,T(R;M_{\rm BH},\dot{M})}\right)-1} \tag{2.19}$$

In order to switch from a single element to the spectrum of the whole Shakura–Sunyaev disc, all the Planck spectra emitted from all the elements that form the disc have to be convolved:

$$L(\nu;\,M_{\rm BH},\dot{M})\,{\rm d}\nu = 2\int_{R_{\rm in}}^{R_{\rm out}} 2\,\pi R{\rm d}R \int_0^{90^\circ} 2\,\pi\,\cos\theta\,\sin\theta\,{\rm d}\theta\;B_\nu[T(R;M_{\rm BH},\dot{M})]\,{\rm d}\nu \tag{2.20}$$

Specifically, integrating over a range of radii one derives the emission from a section of the disc surface. $R_{\rm in}$ has the same definition as previously ($R_{\rm in} = R_{\rm ISCO}$), while $R_{\rm out}$ is generally considered to correspond[2] to $\sim 10^3 R_{\rm S}$. The

[2]The outer edge of the disc is hard to model. Nevertheless, it does not contribute significantly to the emission, and therefore we simply assume a large value for this parameter.

integral over angle θ accounts for the directions in which each surface element of a single face of the disc emits. The fact that each element of the disc emits on both the disc sides as a black body is accounted for with the factor 2 that opens the formula.

The final shape of the multicolor black body model is given by the relation:

$$L(\nu;\, M_{\rm BH}, \dot{M})\,{\rm d}\nu = 4\pi^2 \int_{R_{\rm in}}^{R_{\rm out}} R\, B_\nu[T(R; M_{\rm BH}, \dot{M})]\,{\rm d}\nu\,{\rm d}R \tag{2.21}$$

$M_{\rm BH}$ and $\dot{M}$ are the two fundamental parameters of the model. Both can be connected with observable features. In fact, $\dot{M}$ is easily obtained from its relation with the total disc luminosity (already introduced in Section 2.1.1) $L_{\rm d} = \eta \dot{M} c^2$, where η is the radiative efficiency of the emitting process. For a non–rotating black hole, the emission efficiency is $\eta = 0.06$ (corresponding to the gravitational efficiency of a single particle approaching the black hole with non–zero angular momentum; Shapiro & Teukolsky 1983), but an approximated value $\eta = 0.08$ can be assumed, roughly equivalent to the energy release of infalling matter per unit mass:

$$\eta \simeq \frac{GM_{\rm BH}}{2R_{\rm in}c^2} \simeq 0.08. \tag{2.22}$$

With the accretion rate expressed as a function of the disc luminosity, the parameters of the model can be connected to observable features, and the black hole mass can be obtained by fitting observational data with this relation.

As can be noticed from the explicit expression for the emitting temperature, the inner regions of the disc are hotter than the outer ones. Moreover, the peak of each Planck spectrum is determined by the temperature of the emitting element, in the sense that the exponential cut–off imposed by the $\left[\exp\left({}^{h\nu}/_{kT}\right) - 1\right]^{-1}$ term occurs at frequencies that are higher for higher tem-

peratures. Hence, the elements located at the inner radius produce the black body spectra with the maximum temperatures, that hence peak at the higher frequencies. On the other hand, the elements in the outer radius provides the lowest temperatures and their Planck spectra peak at the lowest frequencies. Indeed, taking into consideration that the multicolor black body spectrum is a convolution of Planck spectra, the shape of the emitted spectrum presents three different behaviours.

Low frequencies: the spectrum rises following the shape of the black body spectrum emitted at the outer radius. The spectrum changes its trend when it reaches the frequencies at which the black body emitted by the outer regions should peak. The asymptothic behaviour of this section of the spectrum is:

$$h\nu \ll k\,T(R_{out}) \quad \Longrightarrow \quad L(\nu) \propto \nu^2 \tag{2.23}$$

Intermediate frequencies: the spectrum is actually the convolution of the black body peaks of all the Planck spectra emitted from the whole disc. This convolution leads to a trend that follows the relation:

$$k\,T(R_{out}) < h\nu < k\,T(R_{in}) \quad \Longrightarrow \quad L(\nu) \propto \nu^{1/3} \tag{2.24}$$

High frequencies: the spectrum presents an exponential cut–off brought by the high frequencies component of the black body spectrum emitted in the inner regions of the disc:

$$h\nu \gg k\,T(R_{in}) \quad \Longrightarrow \quad L(\nu) \propto \exp\left(-\frac{h\nu}{k\,T}\right) \tag{2.25}$$

The multicolor black body spectrum shape is clearly visible in Figure 2.5, along with the asymptotic behaviours.

Note that R_{in} is defined by the geometry assumed for the accreting black hole. Since the inner radius defines the peak frequency of the whole spectrum, in principle this method could be also used to estimate the black hole spin, with a very good data coverage in the peak frequencies (as done for stellar mass black holes).

There are three fundamental parameters that control the specific shape of the multicolor black body spectrum: the outer radius (R_{out}), the accretion rate ($\dot{M}$), directly traced by the disc luminosity (L_d), and the black hole mass (M_{BH}). Changes in these defining parameters lead to variations in the multicolor black body spectrum, leaving the asymptotic behaviours unaltered (see Figure 2.5).

Black hole mass For fixed values of accretion rate and outer radius[3], changes in M_{BH} produce simple rigid shifts in frequency of the whole spectrum. In fact, changes in black hole mass only lead to temperature variations. Temperature influences only the position of the multicolor black body spectrum, through the relation $T \propto M_{BH}^{-1/2}$ (see Eq. 2.17, assuming constant $\dot{M}$).

Accretion rate Variations in $\dot{M}$ correspond to variation in L_d, hence in the fitting process this parameter can be controlled through an observable: the luminosity itself. For fixed values of R_{out} and M_{BH}, variations of the accretion rate intervene in the temperature of the emitting region, as in the previous case, following the relation $T \propto \dot{M}^{1/4} \propto L_d^{1/4}$ (see again Eq. 2.17, for a fixed M_{BH} value). Nevertheless, $\dot{M}$ is directly linked to the disc luminosity, and its variations produce changes in the overall

[3]The outer radius is considered fixed in terms of Schwarzschild radius.

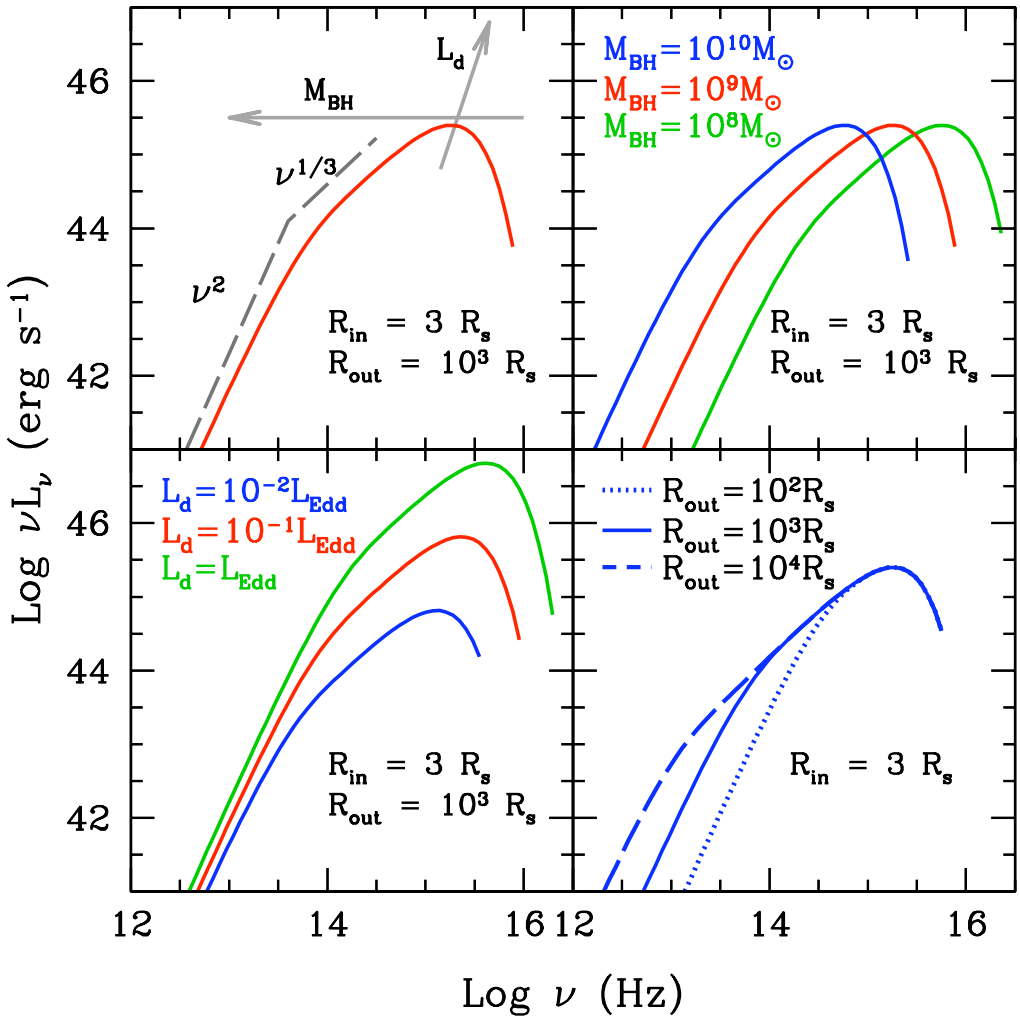

Figure 2.5: The SED of a multicolor black body spectrum, emitted by a Shakura–Sunyaev accretion disc. *Top left:* the spectrum shape (red solid line), along with its asymptotic behaviours described in the text (dashed grey line). The arrows show how the spectrum varies by varying the values of black hole mass and disc luminosity (i.e. accretion rate). *Top right:* effect of variations in black hole mass on a multicolor blackbody spectrum, for constant accretion rate. Note that a higher mass value provokes just a rigid shift toward lower frequencies of the whole spectrum, while the asymptotic trends remain unaltered. *Bottom left:* effect of disc luminosity variations, that correspond to variations in accretion rate, for a constant black hole mass. A larger accretion rate corresponds clearly to a more luminous disc, and also shifts the peak of the emission towards larger frequencies. *Bottom right:* effect of variations in the outer radius of the accretion disc. The outer radius emits the coldest black body in the whole structure, and therefore determines the frequency of the break between the $\propto \nu^2$ and $\propto \nu^{3.5}$ trends.

luminosity emitted from the accretion disc. Clearly, higher accretion rates correspond to more luminous spectra.

Outer radius It is worth reminding that this quantity represents the maximum distance at which the radiative emission is still significant. At this distance the lowest temperature black body is emitted, and hence the emitted spectrum accounts for the first break in the multicolor black body slope. Therefore, for fixed values of $\dot{M}$ ($L_{\rm d}$) and $M_{\rm BH}$, a variation in $R_{\rm out}$ implies a change in the length of the intermediate frequency branch of the multicolor black body spectrum. Larger radii correspond to shorter $\propto \nu^2$ branches and slope changes located at lower frequencies, as evident from Figure 2.5.

In practical terms, the low frequency range of the disc emission is most likely not visible, superposed to other components or simply not luminous enough to be well sampled. Therefore, variations given by the outer radius are not observable in a fitting process. The other two defining parameters, instead, can be used as free parameters to fit this model to suitable data. In particular, if the data to be fitted in the IR–optical–UV range cover the peak of the emitted spectrum, the total disc luminosity can be directly derived from the peak luminosity $\nu_{\rm p} L_{\nu_{\rm p}}$ ($L_{\rm d} = 2\nu_{\rm p} L_{\nu_{\rm p}}$; Calderone et al. 2013). In this specific case, the only free parameter left would be the black hole mass. From this point of view, the accretion disc SED fitting is a very effective mass measurement method. Moreover, by fixing $L_{\rm d}$ this method achieves an average error of a factor 2. This is an important improvement compared to the commonly used virial methods, that only get to an average uncertainty of a factor 3.5–4.

In some cases, a reliable estimate of $\nu_{\rm p} L_{\nu_{\rm p}}$ cannot be obtained. This happens if the available data do not cover properly the whole wavelength range, or if the IR–optical–UV continuum is not purely emitted from the accretion

disc, but is contaminated by other components, such as synchrotron emission from the jet. In this case, broad line region luminosity can provide an estimate of $L_{\rm d}$. As explained in Section 2.1.1 (and specifically in Eq. 2.4), the luminosity emitted from the BLR is $\sim 10\%$ of the disc luminosity. If an optical spectrum is available, the total $L_{\rm BLR}$ can be derived from the luminosity of the individual broad lines, following a spectral templates that report line ratios, such as Francis et al. (1991) or Vanden Berk et al. (2001). In this case, the uncertainty on $L_{\rm d}$ would be influenced by the uncertainty on the covering factor of BLR plasma with respect to the disc. The assumed value is generally 10%, but it could vary for individual sources in a range $5 - 20\%$, that one must add to the intrinsic uncertainty of the assumed spectral template. In this case, then, the overall uncertainty associated to the $L_{\rm d}$ value would be of a factor 3.5–4, comparable to the error associated to virial methods.

3

The jet–disc connection

The connection between accretion structure and jet emission in AGN is a crucial point to understand the physics behind the launching process of the jet. A matter of debate regards the presence and behavior of the relativistic jet relative to the different accretion regimes. The canonical sub–classification scheme applied to blazars (see Section 1.2.1) is commonly interpreted as a hint for different accretion regimes. FSRQs, that are classified as blazars with prominent broad emission lines ($EW > 5$Å), accrete through a radiatively efficient accretion disc, while BL Lacs are generally thought to be characterized by an inefficient accretion flow, and this should be the reason of broad emission lines with smaller equivalent width ($EW < 5$Å).

However, the EW–based classification cannot be a reliable tracer of a difference in the accretion regime. The EW is in fact a measure of the line dominance over the continuum. In the case of blazars, the overall continuum is generally heavily contaminated by the non–thermal emission from the relativistic jet (see Section 1.2.1). For this reason, the equivalent width cannot be considered a measure of line strength. This misclassification clearly does not help in understanding whether jet and specific accretion modes are coexistent in AGN, nor if there is an intrinsic difference between FSRQs and BL Lacs.

Another classification must be considered.

Ghisellini et al. (2011) suggested a classification that truly relies on the accretion rate of the sources: dividing blazars depending on their Eddington ratios, traced by the luminosity emitted from the broad line region. We managed to enlarge the blazar sample later on (Sbarrato et al. 2012a), finding that indeed an EW–based classification can be misleading to understand the accretion features of blazars. In that work, in fact, we managed to classify FSRQs as those γ–ray detected blazars characterized by $L_{\rm BLR}/L_{\rm Edd} > 5 \times 10^{-4}$, while BL Lacs have values lower than that threshold.

This is certainly a hint that FSRQs and BL Lacs accrete on average at different rates, but to understand if there is actually a difference in the accretion regime, one must test the behaviour of broad emission lines compared to the accretion rate itself. Since the jet power is thought to be proportional to the accretion rate itself, to study the BLR luminosity as a function of $\dot{M}$, we can *compare the jet and BLR emissions* (Sbarrato et al. 2014b). We first tried to investigate this relation in the blazar class, using the γ–ray luminosity as a tracer for the jet emission. Since we are not able to reach very low accretion rates by considering only blazars (see Section 3.2), we then extend our study to a sample of low–accreting radio–galaxies, using instead the radio luminosity to trace the jet emission (Section 3.3).

3.1 The sample

We are interested in studying the relationship between jet and accretion in AGN, through γ–ray or radio luminosity and broad line region luminosity, respectively. We first tried to study it among the blazar subclass, by collecting a complete sample of γ–ray detected blazars, with measurements of the lumi-

nosity of broad lines obtained through optical spectroscopy. We then extended our sample to radio–galaxies intrinsically without broad emission lines (but with known redshift), to investigate the jet–accretion relationship in the inefficient accretion regime. Even if not complete, the radio–galaxy sample we describe in Section 3.1.2 is the most useful for our purposes, as the ionization status of every member is throughly studied.

3.1.1 The blazar samples

The Large Area Telescope (LAT) onboard the *Fermi Gamma-Ray Space Telescope* (*Fermi*; Atwood et al. 2009) has detected a large amount of blazars in the γ–rays. In two different papers (Shaw et al. 2012 and Shaw et al. 2013), Shaw and collaborators obtained optical spectroscopic data for all the FSRQs (Shaw et al. 2012) and most of the BL Lacs (Shaw et al. 2013) included in the Second Catalog of AGN Detected by the Fermi LAT (2LAC; Ackermann et al. 2011). We collected from these two papers all the blazars that show broad emission lines in their optical spectra.

In Shaw et al. (2012), the authors analyzed the optical spectra of 229 FSRQs: they obtained new spectra for 165 FSRQs included in the First Catalog of AGN detected by *Fermi* (1LAC; Abdo et al. 2010), and re–analyzed Sloan Digital Sky Survey (SDSS; York et al. 2000) spectra of 64 other FSRQs (not all with γ–ray data). Along with spectroscopic data, the authors derived virial black hole masses for all their objects. In order to have a complete description of the sources, we selected only the FSRQs with enough data to fit the entire SED. We are left with 191 objects. We cross–correlated this sample with the 2LAC. When the objects were not included in the 2LAC, we collected data from the 1LAC. The sample was completed including radio data from the Combined Radio All-Sky Targeted Eight GHz Survey (CRATES; Healey et al. 2007). When

sources were not included in CRATES (only 5 objects), we obtained radio data at frequencies close to 8 GHz from the ASI Science Data Center (ASDC[1]). We are then left with a sample of 180 FSRQs with optical spectroscopy, along with γ–ray and radio data.

In Shaw et al. (2013), instead, the BL Lac objects are directly selected from the 2LAC sample. 2LAC includes 475 BL Lacs, among which only 209 have redshift information. We consider here only those objects with broad emission lines, in order to be able to derive an estimate of $L_{\rm BLR}$, avoiding upper limits. We are left with 26 objects. All of them have 2LAC γ–ray and CRATES radio data. Shaw et al. (2013) did not derive the black hole masses for these objects. We can anyway assign an average $M_{\rm BH}$ value to these BL Lacs, from an adapted version of the $M_{\rm BH} - M_R$ relation (from Bettoni et al. 2003), that assumes a mass ratio between bulge and central black hole of 10^3. In fact, BL Lacs are typically hosted in massive and luminous elliptical galaxies, with a small dispersion in absolute magnitude ($\langle M_R \rangle = -22.8 \pm 0.5$; Sbarufatti, Treves & Falomo 2005). Therefore, we can derive an average value of their black hole mass:

$$\log\left(\frac{M_{\rm BH}}{M_\odot}\right) \simeq -0.5 \times M_R - 3 = 8.4. \tag{3.1}$$

Since we need the central black hole masses for our studies, we will apply this value to every object without a mass estimate. These BL Lacs and their relevant data are listed in Table 3.1.

We add to these new samples the objects that show broad emission lines studied in Sbarrato et al. (2012a). Specifically, we add the 45 FSRQs and 1 BL Lac (following our reclassification) that were included in Shen et al. (2011), along with the 15 BL Lacs with broad emission lines from Ghisellini

[1] http://tools.asdc.asi.it/

et al. (2011). In this work, we only consider the objects from Sbarrato et al. (2012a) that have broad emission lines detected, excluding then all the BL Lacs with only an upper limit on the BLR luminosity. In Sbarrato et al. (2012a), the upper limits were introduced to increase the number of BL Lacs, populating the low–luminosity branch of our sample. They followed the $L_{\rm BLR} - L_\gamma$ correlation already found only with the detections, therefore they were not very constraining. In our new work, we increased the number of BL Lacs with broad emission lines thanks to Shaw et al. (2013), and therefore we do not need the lineless BL Lacs.

In total, we have 225 FSRQs and 42 BL Lacs with detected broad emission lines, both γ–ray and radio counterparts, and a reliable estimate of the central black hole masses.

3.1.2 The radio–galaxy sample

We collected a sample of radio–galaxies without broad emission lines from the work by Buttiglione et al. (2010). The authors studied the optical spectroscopical and radio features of all the $z < 0.3$ radio–galaxies (Buttiglione et al. 2009) with $F_{178\rm MHz} > 9$Jy, $\delta > -5^\circ$ and an optical counterpart from the Third Cambridge radio catalogue (3CR; Spinrad et al. 1985). The authors classify the sources in high–excitation (HEG), low–excitation galaxies (LEG) and broad line objects (BLO) according to optical features. Specifically, BLOs clearly show broad emission lines, while HEGs and LEGs do not show any broad emission feature, but while the latter have an intrinsic lack of broad line emitting structures, the former show high–excitation fingerprints, suggesting obscuration of the broad line region more than a true absence. The introduction of radio–galaxies in our work aims at studying truly lineless jetted AGN, so we include in our sample the 37 LEGs from Buttiglione et al. (2010).

Name	Fermi Name	RA	DEC	z	Line	$\log L_{\rm BLR}$	$\log L_\gamma$	$\log L_{\rm radio}$
[1]	[2]	[3]	[4]	[5]	[6]	[7]	[8]	[9]
BL Lac								
GB6 J0013+1910	0013.8+1907	00 13 56.3	+19 10 41.5	0.477	MgII	42.691	45.441	43.043
PKS 0829+046	0831.9+0429	08 31 48.7	+04 29 38.2	0.174	Ha	42.614	45.520	42.923
RBS 0958	1117.2+2013	11 17 06.1	+20 14 07.6	0.138	Ha	41.722	44.723	41.622
PMN J1125-3556	1125.6-3559	11 25 31.3	-35 57 05.0	0.284	Ha	43.338	45.157	42.627
SBS 1200+608	1203.2+6030	12 03 03.4	+60 31 19.1	0.065	Ha	42.005	43.769	41.190
W Comae	1221.4+2814	12 21 31.6	+28 13 58.1	0.103	Ha	42.137	45.055	42.199
PG 1218+304	1221.3+3010	12 21 21.9	+30 10 36.2	0.184	Ha	42.063	45.174	41.734
OQ 530	1420.2+5422	14 19 46.5	+54 23 15.0	0.153	Ha	42.201	44.766	42.603
RGB J1534+372	1535.4+3720	15 34 47.2	+37 15 53.8	0.144	Ha	41.722	44.349	40.991
BL/FS								
PKS 0332-403	0334.2-4008	03 34 13.4	-40 08 26.9	1.357	MgII	45.046	47.711	44.967
TXS 0431-203	0434.1-2014	04 34 07.9	-20 15 17.2	0.928	MgII	43.153	46.511	43.758
PKS 0437-454	0438.8-4521	04 39 00.7	-45 22 23.9	2.017	CIV	45.201	47.661	45.363
PKS 0627-199	0629.3-2001	06 29 23.7	-19 59 19.7	1.724	CIV	44.060	47.740	45.036
4C +14.60	1540.4+1438	15 40 49.5	+14 47 46.5	0.606	MgII	43.575	45.966	44.229
PMN J1754-6423	1755.5-6423	17 54 41.8	-64 23 44.7	1.255	MgII	44.163	46.912	44.113
4C +56.27	1824.0+5650	18 24 07.0	+56 51 01.1	0.664	MgII	43.912	46.891	44.333
S3 2150+17	2152.4+1735	21 52 24.7	+17 34 37.9	0.874	MgII	44.168	46.333	44.310
PMN J2206-0031	2206.6-0029	22 06 43.2	-00 31 02.3	1.053	MgII	43.798	46.557	43.858
B2 2234+28A	2236.4+2828	22 36 22.3	+28 28 58.1	0.79	MgII	44.645	47.079	44.412
PKS 2244-002	2247.2-0002	22 47 30.1	+00 00 07.0	0.949	MgII	44.106	46.543	43.950
PKS 2312-505	2315.7-5014	23 15 44.2	-50 18 39.7	0.811	MgII	43.628	46.357	43.764
PKS 2351-309	2353.5-3034	23 53 47.3	-30 37 48.3	0.737	MgII	43.628	46.066	43.893
FS								
NVSS J020344+304238	0204.0+3045	02 03 44.1	+30 42 38.1	0.761	MgII	44.757	46.449	43.572
PKS 0516-621	0516.8-6207	05 16 44.5	-62 07 04.8	1.3	MgII	44.444	47.488	44.523
MG2 J201534+3710	2015.6+3709	20 15 28.6	+37 10 59.8	0.859	Hb	44.342	47.971	44.794
TXS 2206+650	2206.6+6500	22 08 03.3	+65 19 38.7	1.121	MgII	44.336	47.324	44.360

Table 3.1: Sources from the BL Lac sample in Shaw et al. (2013), divided according to their reclassification (see Section 3.2). Col. [1]: name; Col. [2]: *Fermi*/LAT counterpart [2FGLJ...]; Col. [3]: right ascension; Col. [4]: declination; Col. [5]: redshift; Col. [6]: line measured, from which $L_{\rm BLR}$ has been derived; Col. [7]: logarithm of the broad line region luminosity (in erg s^{-1}); Col. [8]: logarithm of the γ–ray luminosity from *Fermi* data (in erg s^{-1}); Col. [9]: logarithm of the radio luminosity, calculated at 8 GHz rest–frame (in erg s^{-1}).

Along with the optical spectral analysis, they performed a radio morphology study. The radio analysis provides information on the core power, which allows us to have a reliable tracer of the inner jet power, without contamination from the extended structures. In other words, the core power traces the same emission that is traced by the radio luminosity in the case of blazars, apart from the different beaming factor (due to the different orientation angles of the jet, see Section 3.3). Moreover, the authors provide a measure of the H magnitude, and a calibration to obtain from that the central black hole mass of the objects (Marconi & Hunt 2003):

$$\log\left(\frac{M_{\rm BH}}{M_{\odot}}\right) = -2.77 - 0.464 \times M_H. \tag{3.2}$$

The authors find different radio morphologies among the 37 LEGs: 12 FRI, 16 FRII and 9 unclassifiable sources. One object out of each radio group has no M_H information, so we cannot derive a black hole mass estimate. We exclude from our sample those objects.

We are then left with 11 LEGs FRI, 15 LEGs FRII and 8 LEGs without a radio classification (FR?), all with an estimate of the radio core power, with narrow emission line information that give upper limits on the broad emission lines (see Section 3.1.3), and black hole mass estimates. We also added to the radio–galaxy sample M87, a “classic" LEG FRI, taking the radio flux from the NASA/IPAC Extragalactic Database (NED), while the optical spectroscopic information is taken from Buttiglione et al. (2009). M87 does not show any broad emission line, so in the following we will treat it as the LEGs studied by Buttiglione et al. (2010).

3.1.3 Deriving the BLR Luminosity

To calculate the BLR luminosity, we need an estimate of the broad emission lines of each object, specifically of Lyα, Hα, Hβ, MgII or CIV. In the case of the FSRQs from Shaw et al. (2012), we take directly the emission lines fluxes listed in their work, as we did in Sbarrato et al. (2012a), while in the case of BL Lacs we directly fit the few broad emission lines present. Ghisellini et al. (2011) had already derived from literature the broad emission line values for the BL Lacs included in their sample. Note that the emission lines visible in Mkn421 and Mkn501 spectra have a FWHM ($\sim 1000\,\mathrm{km\,s^{-1}}$) that lies on the classification threshold between narrow lines and broad lines. Therefore, we rather put an upper limit on their broad line luminosities, to be more conservative. We nevertheless leave them in our sample, since they are usually listed as known BL Lacs with lines. The objects included in our radio–galaxy sample have the same issue, being explicitly selected as sources intrinsically lacking broad emission lines. They only show narrow emission lines, so we can obtain from them upper limits on broad emission line luminosities, taking as example quasars with both broad and narrow emission lines. Narrow line dominated (but with broad emission lines) quasars are in fact included in Shen et al. (2011). In their case, the ratio between narrow and broad Hα luminosities is:

$$\frac{L_{\mathrm{nH}\alpha}}{L_{\mathrm{bH}\alpha}} \lesssim 10. \tag{3.3}$$

In other words, if present, the broad emission lines have a luminosity that is at least 10% of the corresponding narrow line luminosity, or more. To be conservative, we choose to fix as a robust upper limit on the broad line luminosity, the luminosity associated to the corresponding detected narrow emission line.

From the broad emission line luminosities or from the upper limits col-

lected for our sample, we can then derive the overall luminosity emitted from the BLR. We follow Celotti et al. (1997) and set the Lyα flux contribution to 100, and the relative weights of the Hα, Hβ, MgII and CIV lines to 77, 22, 34 and 63, respectively (see Francis et al. 1991). The total broad line flux is fixed at 555. The $L_{\rm BLR}$ value of each source has been derived using these proportions. When more than one line is present, we calculate the logarithmic average of the $L_{\rm BLR}$ estimated from each line.

3.2 The $L_{\rm BLR}$–L_γ relation

Figure 3.1 shows how the jet–disc relation can be studied in blazars. The top panel shows the BLR luminosity as a function of the γ–ray luminosity. The bottom panel shows the same quantities divided by the Eddington luminosity ($L_{\rm Edd}$). The objects included in Sbarrato et al. (2012a) are marked as FSRQs or BL Lacs, according to how we classified them in our previous work. The new FSRQs from Shaw et al. (2012) are included as FSRQs, while the objects classified as BL Lacs in Shaw et al. (2013) are marked as BL Lacs, BL/FS or FS in the plots. Note that the correlation we found in Sbarrato et al. (2012a) is confirmed by the new data, both when directly comparing the two luminosities and when normalizing them by the Eddington luminosity. This clearly strengthens the hypothesis of a tight relation between the accretion rate and the jet power in blazars. As explained in Sections 2.1.1 and 2.1.2, the $L_{\rm BLR}$ is a very good tracer of the accretion rate, while the γ–ray luminosity traces well the jet power. We calculate the best fit of the relation between the two luminosities, both normalized by the Eddington luminosity and not. We find that both are consistent with the results found in Sbarrato et al. (2012a). We apply a partial correlation analysis, to take also into account the possible common

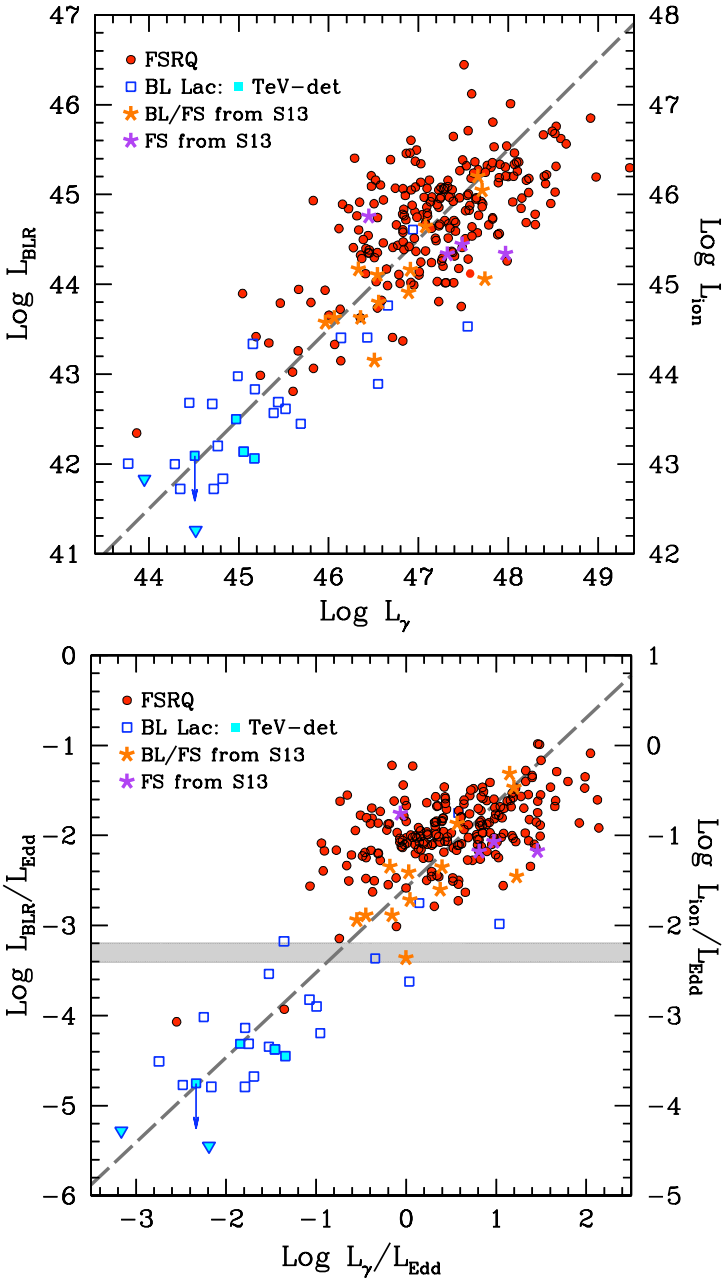

Figure 3.1: Broad line region luminosity as a function of γ–ray luminosity (top panel) and the same, normalized at the Eddington luminosity (bottom panel). Different symbols correspond to different classifications, as labelled. The dashed lines are the results of the least square fits described in Table 3.2. The grey stripe in the bottom panel indicates the luminosity divide between FSRQs and BL Lacs, located at $L_{\rm BLR}/L_{\rm Edd} \sim 5 \times 10^{-4}$.

	m	q	r
$x = \log L_\gamma$; $y = \log L_{\rm BLR}$			
(x, y)	0.92±0.19	1.2±14.8	0.81
(x, y), z	0.92±0.19	1.2±14.8	0.59
$x = \log(L_\gamma/L_{\rm Edd})$; $y = \log(L_{\rm BLR}/L_{\rm Edd})$			
(x, y)	0.84±0.20	–2.46±3.1	0.78
(x, y), z	0.84±0.20	–2.46±3.1	0.65
(x, y), z, M	0.84±0.20	–2.46±3.1	0.64

Table 3.2: Results of the partial correlation analysis of the $L_{\rm BLR} - L_\gamma$ and $L_{\rm BLR}/L_{\rm Edd} - L_\gamma/L_{\rm Edd}$ relations using a least square fit. The whole blazar sample is taken into account, i.e. 267 objects are considered in the analysis. Correlations are of the form $y = mx + q$. The listed slopes m refer to the bisector (of the two correlations x vs y and y vs x). r is the correlation coefficient obtained from the analysis. We list also the results when accounting for the common dependence on redshift and/or black hole mass. In all the cases, the probability that the correlation is random is $P < 4 \times 10^{-8}$, i.e. all the correlations are statistically relevant.

dependence on z and $M_{\rm BH}$ of the values. The $L_{\rm BLR} - L_\gamma$ and $L_{\rm BLR}/L_{\rm Edd} - L_\gamma/L_{\rm Edd}$ relations result linear and statistically relevant (see Table 3.2).

Contrary to our previous work, instead, the apparent 'divide' between FSRQs and BL Lacs (located at $L_{\rm BLR}/L_{\rm Edd} \sim 5 \times 10^{-4}$) seems no longer valid, since some BL Lacs from Shaw et al. (2013) are located in the high–luminosity branch of the correlation, in the area typically occupied by FSRQs (those BL Lacs are marked as purple and orange asterisks, or included among the blue empty squares in all the Figures). To understand this discrepancy with our previous results, we first inspected visually the overall SEDs of the BL Lacs from Shaw et al. (2013). We notice that the sources show three different SED behavior (as shown by the individual SEDs in the Appendix):

- nine have the synchrotron emission dominant or comparable to the high–energy component, and the thermal emission from the accretion structure completely swamped by the non–thermal jet emission. These features define a BL Lac, according to the classification scheme that con-

firmed analogous reclassifications in Ghisellini et al. (2011) and Sbarrato et al. (2012a), also presented in Padovani & Giommi (1995).

- four of them show a clear Compton dominance, and the emission from the accretion disc is clearly visible. We then classify them as FSRQs, and claim for a misclassification in Shaw et al. (2013). However, we highlight them differently and label them as 'FS', to keep track of them in the plots.

- thirteen objects have the high–energy component that slightly dominates the synchrotron emission, as in the case of non extreme FSRQs. On the other hand, the synchrotron component completely swamps the accretion emission, leading to a BL Lac–like optical appearance. We classify them as 'BL/FS', since they show both a FSRQ and a BL Lac fingerprint.

The objects classified as FS and FS/BL are labelled accordingly in all our Figures. From Figure 3.1, we immediately notice that all these "reclassified" BL Lacs are the BL Lacs from Shaw et al. (2013) that occupy the high–luminosity branch of our correlations. The FS have all the typical FSRQ features, so we expect to find them in the high–luminosity branch of the $L_{\rm BLR} - L_\gamma$ correlations (see Figure 3.1). Interestingly, all the other objects from Shaw et al. (2013) that were located in the FSRQ branch are the 13 that we classified as BL/FS. Their location allows us to better understand their peculiar SED features. We can in fact infer that they have an intrinsic powerful jet and a highly luminous accretion disc (i.e. high accretion rate), as common FSRQs, even if their optical spectroscopical features are BL Lac–like. In other words, the BL/FS were classified as BL Lacs because of an unusually powerful synchrotron emission that reduced the EW of their broad emission lines, but are instead FSRQs. Even a very luminous thermal continuum, with the related emission features,

can in fact be overcome by a very luminous non–thermal continuum (Giommi et al. 2012; 2013). Since the synchrotron emission is mainly driven by the energy density of the magnetic field, we can expect that these objects have it unusually high. This is confirmed by the SED modeling. We fitted the overall SEDs with a one–zone leptonic model (Ghisellini & Tavecchio 2009), and the results show that the energy density of the magnetic field of all the BL/FS is unusually high (detailed results will be shown in Ghisellini & Tavecchio 2014, *submitted*).

Considering the reclassification, the division between FSRQs and BL Lacs at $L_{\rm BLR}/L_{\rm Edd} \sim 5 \times 10^{-4}$ becomes even more relevant. The BL/FS are actually FSRQs “disguised" as BL Lacs and the canonical classification based on the equivalent width of their broad emission lines fails in classifying them. The division based on $L_{\rm BLR}/L_{\rm Edd}$ represents a more physical classifying system, since it discriminates the objects in terms of their accretion rate. However, the divide is not sharp, and again our blazar sample seems to be distributed continuously in both the $L_{\rm BLR} - L_\gamma$ and the $L_{\rm BLR}/L_{\rm Edd} - L_\gamma/L_{\rm Edd}$ planes.

Along with the divide, we are interested in studying at what accretion rate (and if) a change in the accretion structure happens. A standard Shakura–Sunyaev disc should occur for accretion rates larger than a critical value $\dot{m}_c$. Below that value, the accretion structure is no longer radiatively efficient, also ionizing less efficiently the plasma in the broad line region. This change in accretion should hence be reflected in a change of slope in the $L_{\rm BLR}/L_{\rm Edd} - L_\gamma/L_{\rm Edd}$ plot. The jet power is in fact directly correlated to the accretion rate at all values of the accretion rate itself (Celotti & Ghisellini 2008; Ghisellini et al. 2010b). In Sbarrato et al. (2012a), the low–luminosity branch of the $L_{\rm BLR}/L_{\rm Edd} - L_\gamma/L_{\rm Edd}$ plot was not populated enough to draw a firm conclusion. The new BL Lacs have increased the number of objects that

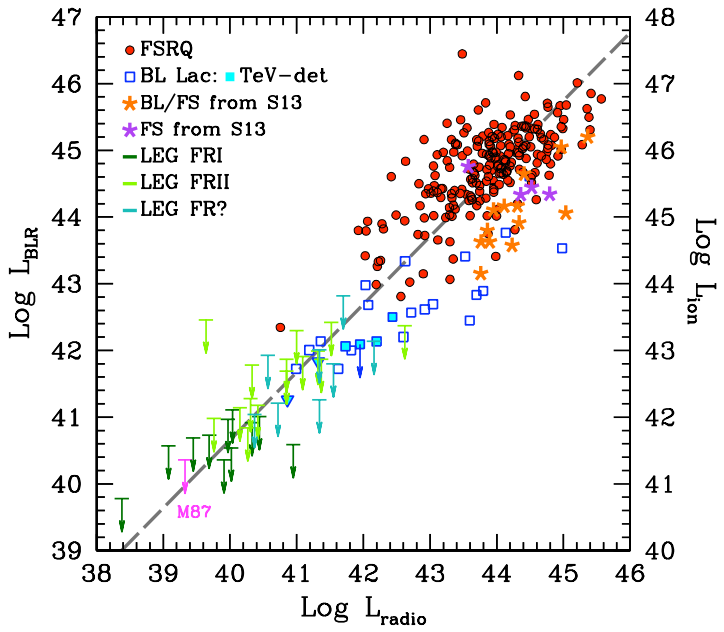

Figure 3.2: Broad line region luminosity as a function of radio luminosity. Different symbols correspond to different classification of the objects. The dashed line is the result of a least square fit calculated among the detection, i.e. the blazars.

could help in understanding the possible existence of a break in the relation, but the data are still too sparse to draw a firm conclusion. Hence, we try to have a new perspective on the problem, by introducing another tracer for the jet power, that allows us to reach smaller accretion rates and observe directly the behavior of the jet–disc system in the case of truly inefficient accretion structures, i.e. objects intrinsically without broad emission lines.

3.3 The $L_{\rm BLR}$–$L_{\rm radio}$ relation

We aim to introduce in our study objects that do not have broad emission lines, but with reliable estimates of z and $M_{\rm BH}$, and a direct proxy for the jet power. We also want to be able to derive an upper limit on their BLR luminosity, which we will use as a proxy for $L_{\rm ion}$. As we saw in BL/FS objects from Shaw et al.

(2013), the non–thermal continuum emitted from the jet, highly boosted because of relativistic effects, can dilute dramatically even strong broad emission lines. In the case of less luminous lines, this problem is obviously even bigger. In fact, the majority of γ–ray detected BL Lacs lacks a reliable redshift estimate, since their optical spectra are completely dominated by the non–thermal emission, and they do not show any emission features. This means that we cannot discriminate whether an object is genuinely lineless or its faint emission lines are simply not visible. Hence, to select only truly lineless object, we choose to introduce in our study a sample of radio–galaxies, i.e. jetted AGN in which the optical emission is not completely dominated by the non–thermal, boosted jet emission. We choose a group of LEGs, to be sure that their broad emission lines are not present, likely because of a radiatively inefficient accretion disc. Radio–galaxies are usually not γ–ray detected, so we cannot use the γ–ray luminosity as a tracer of the jet power. We then consider radio luminosity at 8 GHz rest–frame as an alternative jet tracer, with the following caveat: the radio luminosity is emitted from the jet (as stated by Buttiglione et al. 2010, that compiled the sample and collected the radio data), and is therefore beamed in the emission direction. We will take into account the different beaming factors that characterize blazars and radio–galaxies in the discussion.

Figure 3.2 shows the comparison between broad line region and radio luminosities in all the sources of our samples. All the radio–galaxies have upper limits on their $L_{\rm BLR}$ values, since they are explicitly selected to be lineless (see Section 3.1.3 for the upper limits derivation). Note that the radio luminosities calculated for blazars and radio–galaxies (and plotted in Figure 3.2) are differently beamed, because of different viewing angles. Therefore, the linear correlation over the whole luminosity range is only apparent. To properly study the $L_{\rm radio} - L_{\rm BLR}$ relation, we have to homogenize the beaming factors.

This is true also if we consider the two luminosities normalized to the Eddington luminosity, as shown in Figure 3.3, which we analyze in detail in Section 3.4.

Note that the objects reclassified as BL/FS are located at the highest radio luminosity edge of the correlation in both Figures 3.2 and 3.3. This clearly highlights their FSRQ nature, associated with an uncommonly luminous synchrotron emission, very well traced by the radio luminosity itself. They can easily be considered as the tail at high magnetic field energy density of the class of FSRQs.

Note that in both plots the radio–galaxies are located at $L_{\rm BLR}$ (normalised by $L_{\rm Edd}$ and not) lower than the BL Lacs, with a small overlap. By including these objects, we finally manage to achieve very low disc luminosities, and hence very low accretion rates, which is crucial for our understanding. We discuss the implications of this in Section 3.4. The upper limits hint also at a change in relationship between the tracers of $L_{\rm ion}$ and jet power but their presence in the low–luminosity branch of the sample prevents us from a proper parametric characterization of this relation. To understand if the relationship between $L_{\rm BLR}/L_{\rm Edd}$ and $L_{\rm radio}/L_{\rm Edd}$ is better explained by a single or a broken power–law, we do the following: we treat the upper limits as detections and, since these cluster mostly at the low power end, the slope of the power–law we get from the fit has to be considered as a lower limit (i.e., the true value will be steeper). With this approach, we can compare the two hypotheses of a single and a broken power–law by using an F–test. By minimizing the χ^2 values in the hypotheses of a single power–law

$$\log \frac{L_{\rm BLR}}{L_{\rm Edd}} = (0.87 \pm 0.12) \log \frac{L_{\rm radio}}{L_{\rm Edd}} + 0.28 \tag{3.4}$$

and a broken power–law with break at $L_{\rm radio}/L_{\rm Edd} \sim -4$, we infer that the

data are better described by a broken power–law with a 99.97% level of confidence[2]. The break value is fixed to correspond to the dividing value between FSRQs and BL Lacs in $L_{\rm BLR}/L_{\rm Edd}$ discussed in Section 3.2, following the single power–law. The broken power–law that better fits our data is described by the relation:

$$\log \frac{L_{\rm BLR}}{L_{\rm Edd}} = \begin{cases} (0.98 \pm 0.02) \log \frac{L_{\rm radio}}{L_{\rm Edd}} + 0.72; & \log \frac{L_{\rm radio}}{L_{\rm Edd}} < -4 \\ (0.81 \pm 0.03) \log \frac{L_{\rm radio}}{L_{\rm Edd}} + 0.04; & \log \frac{L_{\rm radio}}{L_{\rm Edd}} \geq -4 \end{cases} \tag{3.5}$$

This shows that a single power law is not a good representation of our data. We discuss in the next section the meaning of this result.

3.4 Unveiling the Change in Accretion

Figure 3.3 is the main result of our work. As we have already pointed out, the radio luminosity has a different physical meaning in the case of blazars and radio–galaxies, because of different beaming levels. To properly compare them, we have to beam the radio luminosity of the radio–galaxies, assuming an average bulk Lorentz factor (Γ) and a viewing angle ($\theta_{\rm v}$). This will shift them at higher radio luminosities, rejoining them with their aligned analogous AGN. Note that the different orientation of blazars and their parent population does not affect the BLR luminosity, since it is emitted isotropically. Therefore, the parent population of a group of blazars would be located at the same $L_{\rm BLR}/L_{\rm Edd}$, with a $L_{\rm radio}/L_{\rm Edd}$ smaller than the corresponding aligned blazars. From their position in Figures 3.2 and 3.3, the LEG FRI radio–galaxies are not

[2]The uncertainties on $\log L_{\rm BLR}/L_{\rm Edd}$, necessaries to calculate the χ^2, are derived from the uncertainties on the broad line luminosities and on the black hole mass measurements, and are typically $\sim$0.3dex.

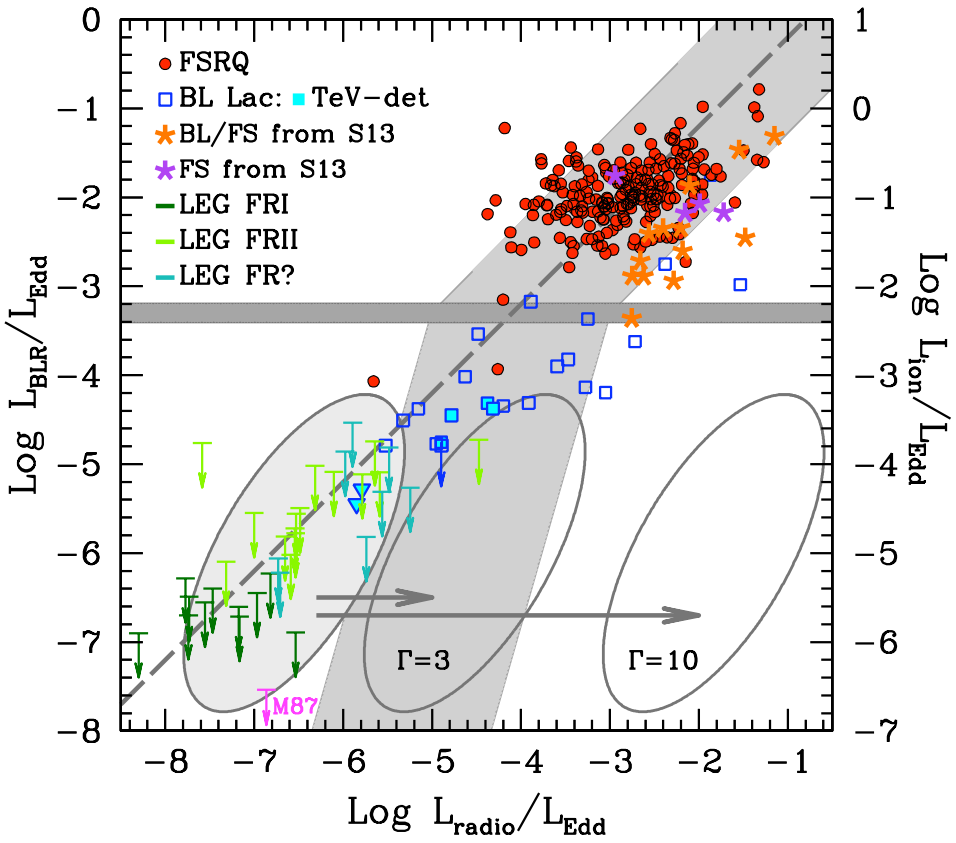

Figure 3.3: Luminosity of the broad line region (in Eddington units) for the sources from our samples as a function of the radio luminosity (in Eddington units). Different symbols correspond to different samples or a different classification of the sources, as labelled. The dashed lines indicate the bisector, rescaled to pass through the FSRQs. The dark grey horizontal stripe indicates the luminosity divide between FSRQs and BL Lacs at $L_{\rm BLR}/L_{\rm Edd} \sim 5 \times 10^{-4}$. The light grey stripe indicates the expected distribution of the luminosities if they were produced by a Shakura–Sunyaev accretion disc for $L_{\rm BLR}/L_{\rm Edd} \sim 5 \times 10^{-4}$ and an ADAF with a Mahadevan–like spectrum ($L_{\rm d} \propto \dot{m}^{3.5}$, see Sections 2.1.1, 2.1.2 and 3.4). The leftmost ellipse include the core of the radio–galaxies of our sample. The central and rightmost ellipses show where the radio–galaxies would be located if they were beamed according to Lorentz factors $\Gamma = 3$ or 10, respectively (as indicated by the arrows, and described in Section 3.4).

the parent population of the BL Lacs included in our study (and see Chiaberge et al. 2000). In fact, it is important to remember that the BL Lacs in our sample have broad emission lines, while the FRI we collected are intrinsically without broad emission lines. This spectral difference explains why our FRI and our BL Lacs are intrinsically different. There is likely a population of *truly lineless BL Lacs* of which these LEGs are actually the parent population, that we are not able to include in our study. In Sbarrato et al. (2012a) we tried to include lineless BL Lacs with known redshift (from Plotkin et al. 2011), but the SDSS spectral resolution did not allow to derive stringent upper limits. Up to now, none of the known BL Lacs with a measured redshift represent the re–oriented analogous of the LEG FRI.

However, we are considering only the tip of the iceberg of the BL Lac population: 2LAC includes 475 BL Lacs (after the additions due to the classification work by Shaw et al. 2013), and most of them do not have a reliable redshift estimate, since their optical spectra are completely featureless. Without a redshift estimate, we cannot derive their intrinsic luminosity in any band, nor calculate an upper limit on their broad line luminosity. Therefore, they cannot be compared to the other blazars in our work. Among them, there are most likely the truly lineless BL Lacs that would be necessary to study the very low accretion regimes, and of course they would be the aligned analogous to the LEGs that we include in our study. This makes the radio–galaxies without broad emission lines even more relevant for our work, since they are the only valid tracer of the low–accretion regime. But to use them to explore that regime, we have to uniform their beaming to the blazar one.

How much do we have to beam the radio luminosity of the LEGs in our sample to compare them with blazars? The beaming factor of a source

with generic Γ, β and θ_v is:

$$\delta = \frac{1}{\Gamma(1 - \beta \cos \theta_v)} \tag{3.6}$$

We take a fixed viewing angle $\theta_{LEG} \sim 40°$ for the LEGs, assuming that they are misaligned. We want to beam their radio luminosity as they were oriented as a blazar, i.e. with $\theta_{BL} \sim 3°$. Therefore we have to boost the radio luminosity by a factor:

$$\left(\frac{\delta_{BL}}{\delta_{LEG}}\right)^3 = \left(\frac{1 - \beta \cos \theta_{LEG}}{1 - \beta \cos \theta_{BL}}\right)^3 \tag{3.7}$$

The only unknown parameter left to determine the beaming factor is therefore the overall Lorentz factor Γ of the jets. We consider two options for the radio–galaxies we are interested to: a uniform jet with a large Lorentz factor $\Gamma \simeq 10$, and a structured jet with a smaller relativistic beaming for the radio emitting region.

Uniform jet: $\Gamma \simeq 10$ If we assume their jets are beamed with a Lorentz factor similar to a common blazar, i.e. $\Gamma \simeq 10$ (Ghisellini et al. 2010), the beaming factor would be $\sim 5 \times 10^4$, shifting the LEGs as drawn in Figure 3.3 (rightmost ellipse). None of the existing blazars could populate that region of the plot, even considering the BL Lacs without redshift. In fact, if we assign an arbitrary $z = 1$ to all BL Lacs without a redshift estimate in 2LAC, we obtain an average radio luminosity at 8 GHz rest–frame $\log L_{radio} \sim 43.2$, that would correspond to $\log(L_{radio}/L_{Edd}) \sim -3.3$. This would not be enough to populate the region occupied by the rightmost ellipse, i.e. the radio–galaxies beamed of a factor $\sim 5 \times 10^4$ due to $\Gamma \simeq 10$. To populate that region, one should postulate the existence of AGN with an extremely powerful and relativistic jet, associated with an accretion structure extremely radiatively inefficient, or even without

any accretion structure present. This beaming level seems then quite unlikely.

Structured jet: $\Gamma \simeq 3$ We can consider another beaming option. From VLBI studies, there is evidence that in strong TeV BL Lacs the pc–scale jets move slowly (Edwards & Piner 2002; Piner & Edwards 2004). At the same time, the extreme variability of their intense TeV luminosity implies that the jet should be highly relativistic, at least in the region where the TeV emission originates. To justify such a discrepancy, the two less demanding hypothesis that have been advanced are:
(i) a deceleration of the emitting region between the TeV and the radio locii (Georganopoulos & Kazanas 2004);
(ii) a spine–layer structure of the jet (Ghisellini et al. 2005).
Furthermore, detailed observations performed with the VLBI show a morphology that suggests the presence of a slower external layer, surrounding a faster core in the jet in the lineless BL Lac Mkn 501 (Giroletti et al. 2004). Similar results have also been obtained in the case of some radio–galaxies (Giovannini et al. 1999; Swain et al. 1998; Owen et al. 1989). Moreover, a velocity structure helps in explaining other features typical of radio–galaxies, such as the configuration of their magnetic field (Komissarov 1990; Laing 1993). According to this hypothesis, the radio emission should then be characterized by a rather small Lorentz factor $\Gamma \sim 3$, being emitted by the external layer. In this case, the LEG radio luminosity can be boosted by a smaller factor $(\delta_{\rm BL}/\delta_{\rm LEG})^3 \sim 100$.

The central ellipse in Figure 3.3 represents this last hypothesis. Such a beaming factor shifts the radio power of the LEGs by such an amount that in the $L_{\rm BLR}/L_{\rm Edd} - L_{\rm radio}/L_{\rm Edd}$ plane they now follow a much steeper relationship

than the almost linear best fit derived in Section 3.3 with the broken power–law. As previously done, we perform an F–test to compare the single and a broken power–law hypotheses, obtained as best fits of our data, all assumed as detections. The two best fits are

$$\log \frac{L_{\rm BLR}}{L_{\rm Edd}} = (0.89 \pm 0.19) \log \frac{L_{\rm radio}}{L_{\rm Edd}} + 0.36 \tag{3.8}$$

and again a broken power–law with break at $L_{\rm radio}/L_{\rm Edd} \sim -4$:

$$\log \frac{L_{\rm BLR}}{L_{\rm Edd}} = \begin{cases} (2.00 \pm 0.06) \log \frac{L_{\rm radio}}{L_{\rm Edd}} + 4.8; & \log \frac{L_{\rm radio}}{L_{\rm Edd}} < -4 \\ (0.78 \pm 0.03) \log \frac{L_{\rm radio}}{L_{\rm Edd}} - 0.08; & \log \frac{L_{\rm radio}}{L_{\rm Edd}} \geq -4 \end{cases} \tag{3.9}$$

The F–test shows that, again, a broken power–law provides a better description of the data at the $> 99.99\%$ level. We stress again that the slope derived with this method at values below the break provides *only a lower limit* to the true slope. In other words, at luminosities smaller than the break, jetted AGN follow a relation *steeper than*:

$$\frac{L_{\rm BLR}}{L_{\rm Edd}} \propto \left(\frac{L_{\rm radio}}{L_{\rm Edd}} \right)^2 \tag{3.10}$$

This clearly means that the jetted AGN highlight the break that we expect from standard theory of accretion discs, i.e. there is a change in the accretion process at $L_{\rm BLR}/L_{\rm Edd} \approx 10^{-3.5}$ (the light grey stripe in Figure 3.3). In fact, if we interpret the LEGs as the jetted AGN with lowest accretion rate, as suggested by their $L_{\rm BLR}$, they would follow a relation that is steeper than the one expected in the case of an efficient accretion structure (i.e. linear), as explained in Section 2.1.2:

$$\frac{L_{\rm BLR}}{L_{\rm Edd}} \propto \frac{L_{\rm ion}}{L_{\rm Edd}} \propto \dot{m}^{3.5}. \tag{3.11}$$

We find that such a transition occurs at $\dot{m}_c = \dot{M}/\dot{M}_{\rm Edd} \sim 0.1$, i.e. $L_{\rm BLR}/L_{\rm Edd} \sim 5 \times 10^{-4} - 10^{-3}$ if a radiative efficiency $\eta \sim 0.1$ is assumed. This threshold is consistent also with the accretion rate transition between FRI and FRII found by Ghisellini & Celotti (2001). The hypothesis of a transition at $\dot{m}_c \sim 10^{-4}$ would not be consistent with the beamed LEG data. In any case, we do not expect a sharp transition, but more likely a smooth one, since we do not observe a clear bimodality in the $L_{\rm BLR}/L_{\rm Edd}$ distribution. In this perspective, BL Lacs that show weak emission lines (empty blue squares in Figures 3.1, 3.2 and 3.3) could also be transition objects.

3.4.1 The importance of viewing angles

In the previous sections, the radio luminosity was used as a tracer of the jet power, instead of γ–ray luminosity. This allowed us to include also radio–galaxies in the study of connection between jet and accretion. Being emitted from the jet, we expect that the radio luminosity is beamed, and therefore a beaming correction is needed. As explained before, this correction strongly depends on the viewing angle under which a specific source is observed.

On the other hand, we do not expect that the broad line region luminosity is affected by beaming, since the broad line emitting clouds likely emit isotropically. Two analogous objects seen under different viewing angles would have the same nuclear observed properties (both from the disc and from the surrounding plasma clouds, such as BLR itself), and different observed luminosity emitted from the jet. Considering the radio luminosity, the two sources would differ by a factor (Dermer 1995; see also Section 4.3.2):

$$\left(\frac{\delta_1}{\delta_2}\right)^3 = \left(\frac{1-\beta\cos\theta_2}{1-\beta\cos\theta_1}\right)^3 \tag{3.12}$$

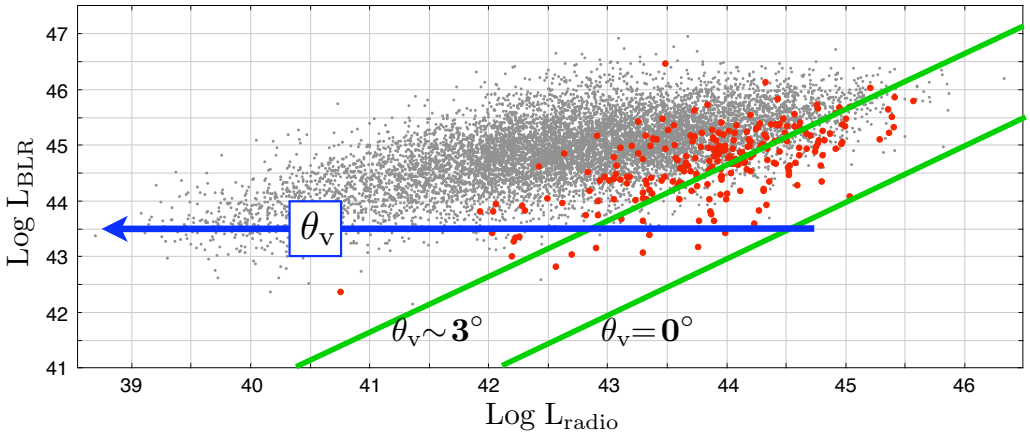

Figure 3.4: Luminosity of the broad line region as a function of the radio luminosity for FSRQ, BL/FS and FS from our sample (red dots), compared with all the radio–detected broad line quasars studied by Shen et al. (2011). Note that all the objects that have their jets oriented along our line of sight are located at higher radio luminosities. This is not an effect of a larger intrinsic jet power, but reflects a larger beaming factor operating on oriented jets. The two green lines and the blue arrow display how the viewing angle affects the radio luminosity.

where β is assumed to be the same, being the two sources completely analogous also in jet features, apart from their orientation. This could lead to a new approach to **estimate the viewing angle**.

Figure 3.4 shows the broad line region luminosity as a function of the radio luminosity for the 9376 radio–detected broad line quasars studied by Shen et al. (2011), with measured broad emission lines. The detection in radio, especially in a radio survey with a flux limit at the mJy level, should ensure the presence of a jet, for this kind of objects (Padovani et al. 2014). Therefore, most of the sources in Shen et al. (2011)[3] are misaligned jetted quasars. Figure 3.4 also includes the FSRQs that we included in the work studied in this Chapter. Compared to the objects in the sample by Shen et al. (2011), they have similar nuclear properties, namely they all show broad emission lines in their optical spectra. The only difference is related to jet orientation. The FSRQs we are considering, in fact, have all been detected

[3]A large fraction that excludes only the faintest objects in radio.

by *Fermi*/LAT, and this ensures that their jets are oriented towards us. As a confirmation that the radio luminosity is strongly affected by beaming, all the FSRQs are located in the highest radio luminosity end, in Figure 3.4.

$L_{\rm BLR}$ and $L_{\rm radio}$ are well correlated among the FSRQs, as we showed in the previous sections, and this correlation is also shown in Figure 3.4. **What can we learn by comparing this correlation with the overall broad–line jetted quasar distribution?** Objects with the same $L_{\rm BLR}$ have same accretion power (see Section 2.1.1, and its application in Sections 3.1.3, 3.2 and 3.3). This means that they also have the same bolometric jet luminosity (Section 3.2; Sbarrato et al. 2012a). The wide range in radio luminosities that corresponds to a single $L_{\rm BLR}$ value in Figure 3.4 is therefore given mainly by a different jet orientation, that implies a different strength in the observed flux.

Following the correlations in Section 3.2 and 3.3, we are able to derive the bolometric jet luminosity of a blazar from its accretion power, if traced by $L_{\rm BLR}$, not contaminated by other components. If the broad emission lines are unchanged by varying the viewing angle, as it seems, this means that we potentially have an univocal tracer for the jet luminosity of a generic source, without the need of estimating its viewing angle. On the other hand, in this way we can compare its bolometric jet luminosity with its observed radio luminosity, and therefore derive a reliable **estimate of its viewing angle**.

This is sometimes done considering the radio–loudness, as defined in Section 1.2. In fact, radio–loudness is a measure of how much the beamed radio emission from the jet is stronger than the isotropic emission from the nucleus. The problem in such a definition, though, is that the canonical radio–loudness is calculated from the observed flux at a fixed optical wavelength, that is often contaminated by non–thermal emission from the jet itself, or also from the host galaxy emission. Following this definition, a true comparison between

beamed and non–beamed emissions is not possible, and therefore an estimate of the viewing angle is also not precise. Using $L_{\rm BLR}$, instead, we are sure that the nuclear isotropic emission is not contaminated by other components. A more reliable estimate of the viewing angle should thus be possible. It is necessary to quantify at which level we can obtain such an estimate, but this is certainly an hypothesis that must be deeply investigated.

4

Finding blazars in the Early Universe

The peculiar orientation of blazars make them the perfect tracers for the whole family of jetted AGN. For each blazar observed and studied, we can assume the presence of a number of analogous jetted AGN with their jets oriented in other directions but the same features (black hole mass, accretion rate, jet power, ...). Knowing exactly the viewing angle ($\theta_{\rm v}$) and the jet beaming angle ($\theta_{\rm b}$) of a blazar allows us to estimate the number of jetted quasars included in its parent population ($N_{\rm parent}$). If we are observing an object with a viewing angle smaller than the beaming angle, in fact, we can estimate the number of objects with the same properties but pointing elsewhere. This estimate is set by the ratio between the all sky surface and the solid angle subtended by the jet beaming angle. This approach is qualitatively schematized in 2D in Figure 4.1, but a quantitative definition is needed.

We can assume that the emitting region is relativistically moving with an overall Lorentz factor $\Gamma = 1/\sqrt{1-\beta^2}$, and emitting isotropically in its own rest frame. Because of the relativistic aberration of light, according to an outside observer the region appears to emit half of its photons into a cone with semi–aperture $\theta_{\rm b}$ defined by $\sin\theta_{\rm b} = 1/\Gamma$ (Rybicki & Lightman 1985). The emitting region is highly relativistic, and therefore moves with $\beta = v/c \sim 1$.

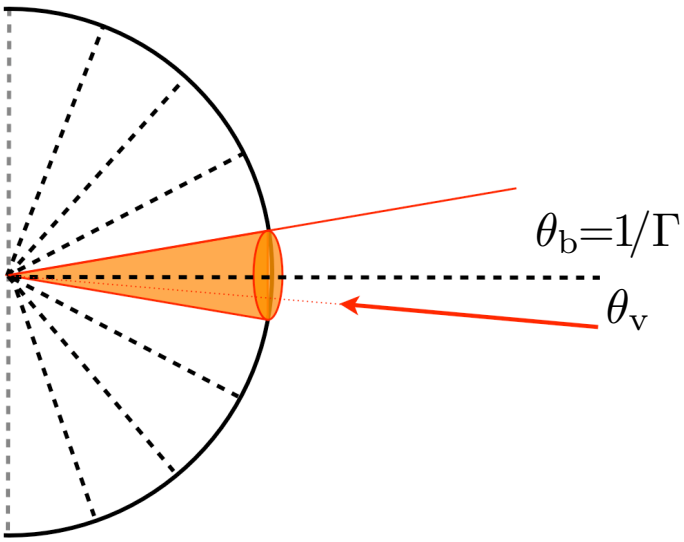

Figure 4.1: Cartoon that summarizes how we can infer a lower limit for the parent population of a blazar with known viewing angle θ_v and beaming angle $\theta_b = 1/\Gamma$.

This implies a very small value for θ_b, and therefore:

$$\sin\theta_b \sim \theta_b \sim \frac{1}{\Gamma}. \tag{4.1}$$

We therefore define the beaming angle of a relativistic jet as $\theta_b = 1/\Gamma$.

We can then derive the ratio between the number of objects observed with $\theta_v \lesssim 1/\Gamma$ and the total number of analogous jetted AGN, but randomly oriented. This estimate corresponds to the ratio f_Ω between the solid angle subtended by the jet beaming angle Ω_b and the all sky surface $\Omega_{4\pi}$. Note that the jetted emission from a single AGN is formed by a jet (that we actually see in the case of a blazar) and a counterjet. Therefore, we must take into account both jet and counterjet in the calculation (i.e. the solid angle subtended by the whole jet emission is $2\Omega_b$):

$$f_\Omega = \frac{2\Omega_b}{\Omega} = \frac{2\times 2\pi\int_0^{\arcsin(1/\Gamma)}\sin\theta\,\mathrm{d}\theta}{4\pi} = \int_\beta^1 \mathrm{d}\cos\theta = 1-\beta \tag{4.2}$$

From this result, we can express f_Ω only as a function of the Lorentz factor Γ:

$$\begin{aligned} f_\Omega &= 1-\beta && \times \frac{1+\beta}{1+\beta} \\ &= \frac{1-\beta^2}{1+\beta} && \text{with} \quad \beta \sim 1 \\ &\simeq \frac{1-\beta^2}{2} = \frac{1}{2\Gamma^2} \end{aligned} \tag{4.3}$$

f_Ω corresponds to the ratio between the number of objects seen at $\theta_v \lesssim 1/\Gamma$ and the total number of jetted objects with jets oriented randomly, i.e. $N_{\rm parent} = N_{\rm blazar}/f_\Omega$. Therefore, the number of analogous jetted AGN oriented in the others directions is:

$$N_{\rm parent} \simeq N_{\rm blazar} \times 2\Gamma^2 = 338 \left(\frac{\Gamma}{13}\right)^2 N_{\rm blazar} \tag{4.4}$$

where $\Gamma = 13$ is the typical value for a blazar. At low redshift this is not particularly more efficient than compiling a complete catalog of misaligned AGN to explore the parent population, since extensive studies and complete quasar catalogs are actually available. At high redshift, instead, a complete collection of jetted AGN is not yet available, and therefore blazars can be main actors in the systematic study of the jetted AGN population, thanks to their statistical relevancy.

The peculiar orientation of blazars, combined with the strong boosting of their jets, makes blazars extremely luminous, and therefore they should be in principle observable even at very high redshift. In principle, then, they should be easy to observe and extremely useful for high–redshift statistics. Nevertheless, only few of them are known at $z > 4$, and all of them were discovered serendipitously.

The systematic discovery of blazars is guaranteed at low–redshift by high–

energy instruments like *Fermi*/LAT. This instrument provides the largest γ–ray catalog of AGN (the Second Catalog of AGN detected by *Fermi*, 2LAC), that mostly include blazars, along with very few radio–galaxies and unclassified AGN. 2LAC includes 310 FSRQs and 395 BL Lacs, but they all have redshift $z \lesssim 3$. This cut is not due only to the sensitivity limit, though, but the high redshift and the blazar sequence are mostly responsible for it. At high redshift, in fact, we expect to see only the most luminous objects, and as explained in Section 1.2.1 and shown in Figure 1.2, the most luminous blazars have the SED peaks at smaller frequencies. This effect, along with the high redshift, shifts the high–energy hump of the SED below 100 MeV. The detection of this component by the *Fermi*/LAT becomes therefore unlikely. Instead, a powerful blazar can be more easily detected at frequencies just before the inverse Compton peak by hard X–ray instruments, like the Burst Alert Telescope (BAT) onboard the *Swift* satellite (Gehrels et al. 2004). This is true already at $z \sim 3$. Unfortunately the *Swift*/BAT has a very high sensitivity limit, and therefore is extremely limited to objects up to $z \sim 4$. At redshift higher than 4, a systematic search at high energies is therefore impossible to perform. A different approach is needed.

The same reason that prevents the compilation of a complete high–energy blazar catalog provides instead an alternative systematic search of blazar candidates, maybe helping to solve the problem. As happens in the case of the high–energy component of the SED, the high redshift and the blazar sequence shift at lower frequencies the low–frequency bump as well. Note however, that the blazar sequence concerns only the non–thermal emission from the relativistic jet. All the other emissions from the AGN are only normally redshifted. Specifically, the thermal emission from the accretion structure, that in the case of a thin Shakura–Sunyaev disc peaks in the UV wavelength range

(rest frame), is usually partially or completely covered by the synchrotron emission from the jet. At very high redshift, we expect to observe blazars powerful enough to shift the synchrotron component enough to leave “naked" the spectrum emitted from the accretion disc. In other words, in the optical–UV–soft X wavelength range the SEDs of these blazars are likely dominated by the thermal emission from the disc. This is particularly useful to set up a systematic search of blazar candidates, because that energy range will be dominated by the same structures that dominate in the case of non–jetted AGN or misaligned jetted ones. The blazars we want to identify are therefore indistinguishable from all the other AGN with the same central structures, at very high redshift. Therefore, *blazars can be found in large optical quasar catalogs*, and our search of high–redshift blazar candidates (Sbarrato et al. 2013a) is therefore based on this feature.

4.1 Sample Selection

At redshift larger than 4, blazars show in the IR–optical–UV the same emitting features as non–jetted and misaligned jetted quasars do. A systematic approach is possible if a complete quasar catalog is used as a starting point for searching for blazar candidates. This is feasible since only FSRQs can be observed at such high redshift: BL Lacs (if present) would not have reliable redshift estimates. Specifically in the optical range, therefore, we can be sure that the thermal emission from the accretion disc dominate the continuum emission, along with the emission lines from BLR and NLR that are visible in that wavelength range. For this reason, to systematically select good blazar candidates, we consider in this thesis the Quasar Catalog (Schneider et al. 2010) obtained from the 7^{th} Data Release (DR7) of the SDSS.

The **SDSS DR7 Quasar Catalog** is suitable for our project since it is a well defined sample, i.e. it is flux limited and covers a known portion of the sky. A systematic selection of candidates and their consequent classification lead to the compilation of a complete catalog of objects that could be easily compared to the complete blazar catalogs obtained thanks to high–energy telescopes at lower redshift. In this way, after the confirmation of our candidates, we will be able to reconstruct the number density not only of the confirmed blazars themselves, but also of their parent population, i.e. the misaligned jetted quasars. This was already done in the literature at lower redshift (see e.g. Ghisellini et al. 2010a; 2013).

The SDSS DR7 Quasar Catalog includes SDSS objects that have luminosities in the i–band larger than $M_i = -22$ (i.e. $\nu L_\nu(5100\text{Å}) > 10^{44}\,\text{erg}\,\text{s}^{-1}$), have at least one emission line with FWHM $> 1000\,\text{km}\,\text{s}^{-1}$ and a highly reliable redshift. Moreover, the SDSS DR7 Quasar Catalog has been spectroscopically analyzed by Shen et al. (2011), that derived continuum and line features in the wavelength ranges around Hα, Hβ, MgII and CIV lines. Various virial black hole mass estimates based on different calibration are derived for all the 105,783 quasars included in the catalog. Shen et al. (2011) cross–correlated the sample with the Faint Images of the Radio Sky at Twenty-Centimeters (FIRST; White et al. 1997) radio survey, providing the 1.4 GHz radio fluxes and the radio–loudnesses for all the SDSS quasars with a FIRST counterpart. Shen et al. (2011) choose to define the radio–loudness as

$$R \equiv \left[\frac{F_{1.4\text{GHz}}}{F_{2500\text{Å}}}\right]_{\text{rest frame}}. \tag{4.5}$$

In order to select good high–redshift blazar candidates, we limit our search to the quasars with $z > 4$ and the most extreme radio–loudness, namely $R >$

SDSS quasars	105,783
radio–detected	9399
$z > 4$	1248
radio–detected; $z > 4$	53
$R > 100$	31

Table 4.1: Numerical composition of the SDSS DR7 Quasar Catalog analyzed by Shen et al. (2011), focussed on the features we are interested in: extreme radio–loudness and high–redshift.

100. We introduce a radio–loudness requirement because it helps in selecting objects with jets close to our line–of–sight (Section 3.4.1). While the radio flux at 1.4 GHz is emitted anisotropically along the jet direction, in fact, the optical emission at 2500Å is emitted isotropically from the accretion structure. In the case of a radio–loud quasar, therefore, an extreme radio–loudness value measures the dominance of the jet emission over the accretion luminosity. This dominance is not only relative to the jet being more powerful than the disc, but since the observed radio luminosity is affected by beaming, it gets strongly enhanced by the direction of the jet. Therefore, the radio–loudness of a jetted quasar gets extreme in the case we observe the radio emission from a jet relativistically beamed.

Following these selection criteria, we obtain a sample of 31 high–redshift, extremely radio–loud quasars. Table 4.2 lists these objects, along with their most illustrative data. We include from Shen et al. (2011) redshift, radio–loudness, radio flux, bolometric and CIV line luminosities and the best black hole mass estimate, where available. For those where the CIV line was visible, we include the overall broad line region luminosity ($L_{\rm BLR}$), derived following the template by Francis et al. (1991). Note that 7 objects out of this list have already an X–ray detection. For those objects, we report in Table 4.3 the X–ray spectral index and flux (in the 0.3–10 keV band). 2 of them can be classified as blazars, thanks to their hard and intense X–ray fluxes (i.e. SDSS

RA DEC	z	R	$\log \nu_r F_{\nu_r}$	$\log L_{\rm bol}$	$\log L_{\rm CIV}$	$\log M_{\rm S11}$	$\log L_{\rm BLR}$
[1]	[2]	[3]	[4]	[5]	[6]	[7]	[8]
021043.16 –001818.4	4.733	140	–15.87	47.21	45.20	-	46.15
030437.21 +004653.5	4.305	2410	–15.43	46.91	44.71	9.65	45.65
081333.32 +350810.8	4.922	610	–15.78	47.25	45.76	10.65	46.71
083946.22 +511202.8	4.390	285	–15.23	47.53	45.00	9.95	45.94
085111.59 +142337.7	4.307	270	–15.64	47.17	44.11	-	45.05
091316.55 +591921.6	5.122	3599	–15.61	-	-	-	-
091824.38 +063653.3	4.192	189	–15.43	47.21	44.76	9.83	45.71
100645.58 +462717.2	4.444	131	–16.03	47.06	44.43	-	45.36
102623.61 +254259.5	5.304	5222	–14.47	-	-	-	-
103717.72 +182303.0	4.051	214	–15.72	46.75	45.01	8.45	45.95
105320.42 –001649.7	4.304	149	–15.71	47.2	45.42	8.83	46.36
111856.15 +370255.9	4.025	155	–16.05	47.26	45.13	9.16	46.08
114657.79 +403708.6	5.005	1013	–15.76	-	-	-	-
123142.17 +381658.9	4.137	264	–15.47	46.74	44.91	8.46	45.86
123503.03 –000331.7	4.723	1493	–15.59	46.68	44.60	9.18	45.55
124230.58 +542257.3	4.73	631	–15.55	47.10	44.94	-	45.89
130738.83 +150752.0	4.111	317	–15.76	47.09	44.66	9.62	45.61
130940.70 +573309.9	4.268	133	–15.80	47.08	45.05	8.32	45.99
131121.32 +222738.6	4.612	394	–16.04	46.79	44.89	9.29	45.84
132512.49 +112329.7	4.412	879	–15.00	47.44	45.42	9.46	46.37
141209.96 +062406.9	4.467	852	–15.22	47.25	44.29	9.86	45.24
142048.01 +120545.9	4.034	1904	–14.91	47.05	44.97	9.28	45.91
143003.96 +144354.8	4.834	391	–16.51	46.85	44.79	10.08	45.74
143413.05 +162852.7	4.195	121	–16.16	47.08	45.03	9.17	45.97
145212.86 +023526.3	4.889	365	–16.21	46.90	-	-	-
151002.92 +570243.3	4.309	13463	–14.45	47.08	44.87	8.51	45.82
152028.14 +183556.1	4.123	104	–16.01	47.07	44.61	9.28	45.43
165913.23 +210115.8	4.784	637	–15.39	47.10	44.12	-	45.06
172026.68 +310431.6	4.669	306	–15.83	46.96	44.80	9.73	45.74
172007.19 +602824.0	4.424	124	–16.15	46.98	44.84	8.85	45.79
222032.50 +002537.5	4.205	4521	–14.87	46.93	45.05	9.15	46.00

Table 4.2: Sources from the DR7 Quasar Catalog with $z > 4$ and radio–loudness $R > 100$. Col. [1]: right ascension and declination (i.e. SDSS name: "SDSS J..."); Col. [2]: redshift; Col. [3]: radio–loudness defined as by Shen et al. 2011 ($R = F_{\rm 5GHz}/F_{2500}$, fluxes rest frame); Col. [4]: logarithm of the radio flux in $\rm erg\,cm^{-2}\,s^{-1}$; Col. [5]: logarithm of the bolometric luminosity, as obtained by Shen et al. 2011 ($\rm erg\,s^{-1}$); Col. [6]: logarithm of the CIV luminosity, as obtained by Shen et al. 2011 ($\rm erg\,s^{-1}$); Col. [7]: logarithm of the BH mass, as derived by Shen et al. 2011 (solar masses); Col. [8]: logarithm of the broad line region luminosity, calculated from the CIV line luminosity ($\rm erg\,s^{-1}$).

RA DEC [1]	z [2]	$\log F_X$ [3]	Γ_X [4]	Ref [5]
021043.16 –001818.4	4.733	–13.07	2.03	Sh05
083946.22 +511202.8	4.390	–12.82	1.64	Ba04
091316.55 +591921.6	5.122	–14.32	1.64	Ba04
091824.38 +063653.3	4.192	–12.96	1.80	Ba04
130940.70 +573309.9	4.268	–13.19	1.80	Ba04
132512.49 +112329.7	4.412	–13.20	1.60	Ba04
151002.92 +570243.3	4.309	–12.27	1.51	Yo09

Table 4.3: Sources from the DR7 Quasar Catalog with $z > 4$ and radio–loudness $R > 100$, already observed in the X–rays. Col. [1]: right ascension and declination (i.e. SDSS name: "SDSS J..."); Col. [2]: redshift; Col. [3]: logarithm of the X–ray flux in the energy range 0.3–10keV, in erg cm^{-2} s^{-1}; Col. [4]: X–ray photon index; Col. [5]: references for X–ray data. Ba04 stands for Bassett et al. (2004), Sh05 for Shemmer et al. (2005), Yo09 for Young, Elvis & Risaliti (2009).

J083946.22+511202.8 and SDSS J151002.92+570243.3). Specifically, SDSS J151002.92+570243.3 is one of the firsts high redshift ($z > 4$) blazars ever discovered (Moran & Helfand, 1997).

Without these 7 quasars already observed in the X–rays, we are left with 24 high–redshift, extremely radio–loud quasars that were not observed in the X–rays. Since we want to use the blazars that we will identify as tracers of the most massive black holes in the early Universe, we are particularly interested in estimating their masses. At $z > 4$ the virial methods can rely only on the CIV emission line, that disappears from the SDSS optical range at $z = 4.7$. Therefore, to have coherent measures for the whole selection of quasars, we need a different approach. We take advantage of the SED peculiarity of blazars, that show a "naked" disc in the optical range, exactly like non–jetted and misaligned jetted quasars. In this way, we can *directly fit the SED emitted from the accretion disc*, with the procedure that is described in Section 2.2.3.

To reliably fit the emission from the accretion disc, a good coverage of the optical–IR wavelength range is needed. Public data cover the two extremes of this range, with SDSS spectroscopy for the optical part ($\lambda_{obs} \sim 3900 - 9000$Å)

and photometry from the Wide–field Infrared Survey Explorer (WISE[1]; Wright et al. 2010) to cover the far IR. To fill the gap between the wavelength ranges of these two releases, we observed our candidates from La Silla (Chile) with the Gamma–Ray Burst Optical Near–infrared Detector (GROND; Greiner et al. 2008), simultaneously in 3 NIR and 4 optical filters. The partial superposition of the GROND optical filters with the SDSS ones allows to reduce the problems due to the possible variability of the objects. GROND data are very important, because we expect that the peak of the accretion disc emission falls between this wavelength range and the optical band provided by the SDSS. Since only 19 out of the 24 radio–loud high–z quasars not observed in the X–rays of the original sample are visible from La Silla, we reduce our sample to these 19, listed in Tab. 4.6. These 19 sources have a very complete IR–optical coverage, and we focus on them to estimate the $M_{\rm BH}$ and also to compile a sample of good blazar candidates.

4.1.1 GROND observations and data analysis

The 7–band GROND imager is mounted at the 2.2m telescope of the Max-Planck-Gesellschaft (MPG), operated by MPG and ESO (European Southern Observatory) at La Silla (Chile). GROND is able to observe *simultaneously* in 7 filters, from the NIR $K_{\rm s}$ (2400 nm) to the g' band (450 nm), i.e. from 2200 to 360 nm.

We[2] carried out observations for all sources simultaneously in all 7 g',r', i', z', J, H, $K_{\rm s}$ bands. The log of the GROND observations and the related observing conditions are reported in Tab. 4.4.

The GROND optical and NIR image reduction and photometry were per-

[1]Data retrieved from http://irsa.ipac.caltech.edu/

[2]GROND observations and data analysis were performed by Dr. M. Nardini, and therefore I am reporting the procedure as in Sbarrato et al. (2013a).

Name	Date yyyy–mm–dd	Mid time [UTC]	Exp: opt/IR [s]	Seeing [arcsec]	Mean airmass
SDSS J021043.16-001818.4	2012-08-10	10:10:58	919/960	1.3	1.16
SDSS J030437.21+004653.6	2012-08-21	09:12:29	602/720	0.9	1.17
SDSS J085111.60+142337.8	2012-04-20	23:27:28	919/960	1.3	1.38
SDSS J091824.38+063653.3	2012-04-21	23:27:00	919/960	1.4	1.25
SDSS J102623.62+254259.6	2012-04-16	23:29:13	919/960	1.2	2.11
SDSS J103717.73+182303.1	2012-06-04	23:18:23	919/960	1.4	1.54
SDSS J105320.42-001649.5	2012-06-08	23:22:55	919/960	1.0	1.18
SDSS J123503.02-000331.6	2012-06-14	23:10:40	805/840	1.3	1.16
SDSS J130738.83+150752.1	2012-07-04	23:17:37	919/960	2.6	1.41
SDSS J131121.32+222738.6	2012-06-30	01:07:42	919/960	1.1	1.88
SDSS J132512.49+112329.7	2012-07-06	23:06:23	920/960	1.1	1.32
SDSS J141209.96+062406.8	2012-08-26	23:27:05	460/480	1.3	1.75
SDSS J142048.01+120546.0	2012-08-12	23:34:17	919/960	2.9	1.62
SDSS J143003.96+144354.8	2012-08-13	00:13:27	919/960	2.0	1.82
SDSS J143413.05+162852.7	2012-08-21	23:31:37	672/840	1.8	1.90
SDSS J145212.85+023526.4	2012-08-28	23:33:18	919/960	1.5	1.23
SDSS J152028.14+183556.1	2012-09-04	23:38:49	919/960	1.8	2.04
SDSS J165913.23+210115.8	2012-09-15	23:57:11	919/960	1.3	1.83
SDSS J222032.50+002537.5	2012-05-28	19:35:30	460/480	1.7	1.15

Table 4.4: Log of GROND observations. Exposures refer to optical/NIR filters while the average seeing is calculated in the r' band.

formed using standard IRAF tasks (Tody 1993), similar to the procedure described in Krühler et al. (2008). A general model for the point–spread function (PSF) of each image was constructed using bright field stars, and it was then fitted to the point source. The fields of all sources in our sample are covered by the SDSS (Smith et al. 2002) survey, therefore the absolute calibration of the g', r', i', z' bands was obtained with respect to the magnitudes of SDSS stars within the blazar field. For all sources the J, H, K_s bands calibrations were obtained with respect to magnitudes of the Two Micron All Sky Survey (2MASS) stars (Skrutskie et al. 2006).

Tab. 4.4 reports the log of the GROND observations while Tab. 4.5 reports the observed AB magnitudes, not corrected for the Galactic extinction listed in the last column and taken from Schlafly & Finkbeiner (2011).

Name	g'	r'	i'	z'	J	H	K_s	A_V
SDSS J021043.16-001818.4	22.75±0.13	20.30±0.02	19.34±0.02	19.17±0.02	19.28±0.05	19.13±0.07	18.96±0.14	0.080
SDSS J030437.21+004653.6	22.80±0.10	20.78±0.03	20.34±0.04	20.32±0.04	20.29±0.15	19.74±0.18	20.29±0.45	0.277
SDSS J085111.60+142337.8	22.28±0.07	20.45±0.02	19.86±0.02	19.52±0.02	19.12±0.07	18.93±0.10	18.48±0.16	0.105
SDSS J091824.38+063653.3	21.43±0.04	19.63±0.01	19.03±0.02	18.92±0.02	18.53±0.04	18.26±0.05	18.15±0.16	0.119
SDSS J102623.62+254259.6	24.51±0.56	22.07±0.08	19.97±0.03	19.86±0.04	19.50±0.10	19.23±0.15	19.07±0.21	0.064
SDSS J103717.73+182303.1	21.47±0.01	19.93±0.02	19.75±0.03	20.04±0.03	19.63±0.07	19.37±0.14	19.70±0.28	0.073
SDSS J105320.42–001649.5	21.93±0.03	19.42±0.01	19.35±0.01	19.21±0.02	18.92±0.05	18.58±0.06	18.22±0.09	0.146
SDSS J123503.02–000331.6	24.47±0.31	21.25±0.03	21.48±0.03	20.32±0.04	20.11±0.15	19.69±0.29	20.38±0.69	0.062
SDSS J130738.83+150752.1	21.20±0.06	19.99±0.02	19.84±0.04	19.77±0.04	19.43±0.10	19.32±0.12	19.25±0.16	0.103
SDSS J131121.32+222738.6	> 23.5	21.29±0.04	20.60±0.05	20.43±0.05	20.08±0.13	19.51±0.14	19.54±0.28	0.035
SDSS J132512.49+112329.7	22.15±0.06	19.51±0.01	19.35±0.01	18.94±0.02	19.02±0.05	18.56±0.06	18.63±0.09	0.065
SDSS J141209.96+062406.8	22.11±0.19	20.18±0.03	19.54±0.03	19.49±0.04	19.56±0.09	19.50±0.13	> 19.4	0.089
SDSS J142048.01+120546.0	21.21±0.03	19.93±0.02	19.55±0.03	19.69±0.03	19.64±0.11	19.39±0.17	19.24±0.40	0.076
SDSS J143003.96+144354.8	> 24.2	21.67±0.06	20.31±0.03	20.11±0.04	19.56±0.09	19.58±0.15	19.26±0.18	0.072
SDSS J143413.05+162852.7	22.09±0.15	20.14±0.02	20.13±0.05	20.23±0.07	19.74±0.12	19.71±0.20	19.75±0.31	0.066
SDSS J145212.85+023526.4	> 22.9	21.96±0.11	20.11±0.04	20.00±0.05	19.82±0.12	19.81±0.18	20.22±0.92	0.113
SDSS J152028.14+183556.1	21.21±0.05	19.74±0.02	19.41±0.02	19.32±0.03	19.41±0.11	19.33±0.15	19.23±0.29	0.148
SDSS J165913.23+210115.8	> 24.3	21.57±0.04	20.10±0.02	19.99±0.03	19.71±0.09	18.85±0.08	19.63±0.33	0.202
SDSS J222032.50+002537.5	22.31±0.10	20.24±0.02	19.67±0.06	20.01±0.04	19.67±0.12	19.56±0.19	19.32±0.58	0.183

Table 4.5: Observed magnitudes, not corrected for Galactic foreground reddening, in the AB system. Errors include systematics. The last column reports the value of the Galactic A_V from Schlafly & Finkbeiner (2011).

4.2 The IR to optical SED: studying the accretion disc

In Appendix B we show the IR to optical SEDs of 18 out of the 19 blazar candidates we selected. SDSS J102623.61+254259.5 (B2 1023+25 hereafter) is used in this Section to describe our method of accretion disc fitting as applied to the available data. The first evident feature of B2 1023+25 optical–IR SED (Figure 4.2), that is common to all our sources, is the Lyα forest, i.e. the prominent absorption clearly visible in the SDSS spectra (black line) and in the g' and sometimes r' band GROND photometric data (red points) at frequencies larger than $\log(\nu/\mathrm{Hz}) = 15.4$ (i.e. after the Lyα line, $\lambda = 1216$Å). The Lyα forest is caused by intervening Lyα clouds, present in random density and distance along each line of sight. Since the effects of this absorption are unlikely to be predicted, we do not try to fit the data at frequencies larger than the Lyα. [green, blue and cyan lines in Figure 4.2 become dashed at ν larger than $\log(\nu/\mathrm{Hz}) = 15.4$].

Another recurrent feature among all the analyzed sources (see Figures B.1, B.2 and B.3), is the change of slope driven by the redder WISE bands (purple points and upper limits) with respect to optical an bluer IR data. When the lowest frequency WISE data is not an upper limit, indeed, it has always a luminosity at least half a decade larger than one would expect extrapolating the flux from larger frequencies. This could be ascribed to the presence of a different component, such as the synchrotron hump or an emission from the dusty torus (Calderone, Sbarrato & Ghisellini 2012). This cannot be confirmed in the case of B2 1023+25, since this source has an upper limit on the redder WISE band. This specific object is in fact slightly fainter than the others, being at the largest redshift.

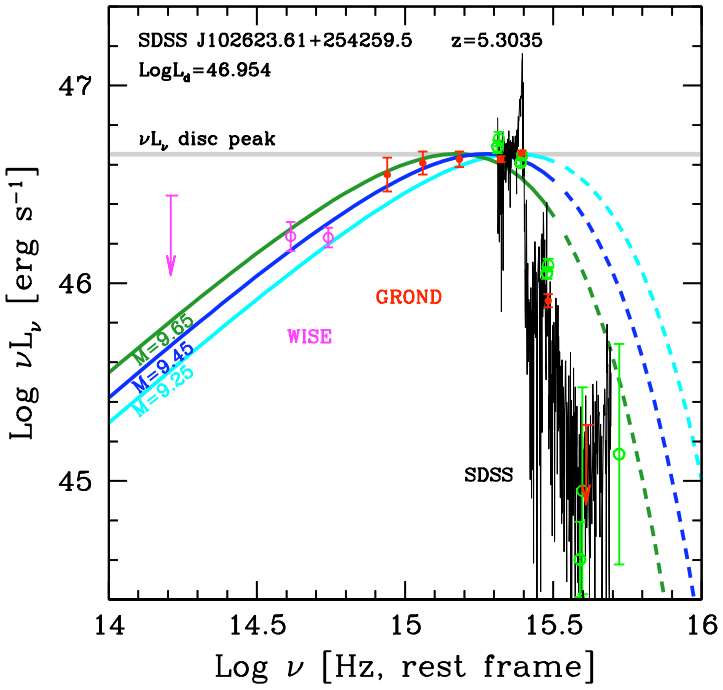

Figure 4.2: UV–Optical–IR SED of B2 1023+25 in the rest frame, together with models of standard accretion disc emission (described in Section 2.2.3). Data from WISE and GROND, and the SDSS spectrum are labelled. Green points are archival data taken from ASDC SED builder. The grey stripe indicates the νL_ν peak luminosity of the disc. We show the spectrum of three accretion disc models with the same luminosity and different $M_{\rm BH}$: $\log(M_{\rm BH}/M_\odot)$=9.65 (green), 9.45 (blue) and 9.25 (cyan). Note that outside this range of masses, the model cannot fit satisfactory the data.

The most useful feature that characterizes the optical–NIR spectra of our sources is the possibility to directly observe the νL_ν peak of the accretion disc spectrum. Just before the Lyα forest absorption the SDSS data highlight a peak in the νL_ν emitted spectrum, that ends the clear increasing trend of the flux from GROND. The highest redshift objects show this peak even in the GROND bands. B2 1023+25 is among them, and in Figure 4.2 the peak of the disc emission is clearly visible.

The visibility of the accretion disc, along with its νL_ν peak, allows us to reliably fit it with a theoretical model, in order to derive the black hole mass.

4.2.1 The disc luminosity

To derive a reliable estimate of the black hole mass, as detailed in Section 2.2.3, a reliable estimate of the disc luminosity is needed. The multicolor black body spectrum model depends in fact on two parameters only: $M_{\rm BH}$ itself and accretion rate ($\dot{M}$), directly linked to $L_{\rm d}$.

One way to derive the overall disc luminosity is through the total luminosity emitted from the broad line region (Section 2.2.3). As described in Section 2.1.1, a radiatively efficient accretion disc is the principal source of UV photons that ionize the BLR, hence the BLR re–emits a fraction of the luminosity emitted from the disc itself, that corresponds to its covering factor ($\sim$ 10%). All our sources show in their optical spectra prominent broad emission lines (Lyα is present in all of them, CIV at $z < 4.7$), therefore we are sure that our whole sample accretes through a radiatively efficient accretion disc. The luminosity emitted from the whole BLR can be derived from the luminosities of the principal broad emission lines through the templates calculated by Francis et al. (1991) and Vanden Berk et al. (2001). In this way we obtain a range of possible values of the disc luminosity, determined by the uncertain value of the covering factor, that can range between 5% and 20% and on the template uncertainties.

On the other hand, when the peak of the accretion disc component is directly visible, we can strongly reduce the uncertainties on its bolometric luminosity. This often occurs for the sources in our sample, despite the possible contribution of the jet synchrotron emission. This is due to the large redshift of the sources, redshifting the peak of the disc component within the optical band, red–ward of the Lyman–α limit, and because our sources, being very powerful, all have a synchrotron component peaking in the far IR or mm band. Hence, with the good coverage of the optical–NIR band given by

the SDSS, GROND and WISE data, we obtain for all our blazar candidates the peak luminosities and can constrain the total disc luminosity. The uncertainty of our method is hence associated only to the measurement errors of the flux and to its possible variability, since the GROND, WISE and SDSS data are not simultaneous. Anyway, we do not expect large variability in this range. In fact, B2 1023+25 was observed twice with GROND (see Section 4.3.1), and the data points are perfectly consistent.

An estimate of the thermal emission from a quasar is commonly obtained by applying a *bolometric correction* to the flux at fixed rest–frame wavelengths (see e.g. Richards et al. 2006). The *bolometric luminosity* ($L_{\rm bol}$) derived in this way is all the thermal emission from the nucleus, and includes accretion disc, torus and corona emission. Richards et al. (2006) show that the emission from the accretion disc is half the bolometric luminosity as derived with their bolometric correction.

The $L_{\rm bol}$ estimate is based on the assumption that all quasars have roughly the same thermal emission, but does not take into account possible contamination from other non–thermal emissions, such as the jet emission. Specifically, in blazars the optical flux is often contaminated by the synchrotron emission. By comparing our estimates of the disc luminosity with the canonically derived bolometric luminosity, we can estimate if the IR–optical–UV emission we observe in the objects from our sample is truly not contaminated by the jet. This comparison can be easily performed, since we selected our objects from the SDSS DR7 Quasar Catalog, that was spectroscopically analyzed by Shen et al. (2011). In their study, the authors derived also various virial estimates of the black hole mass, and an estimate of the bolometric luminosity emitted from the sources. The left panel of Figure 4.3 shows the comparison. Note that no peculiar trend nor an evident offset is present between the two lu-

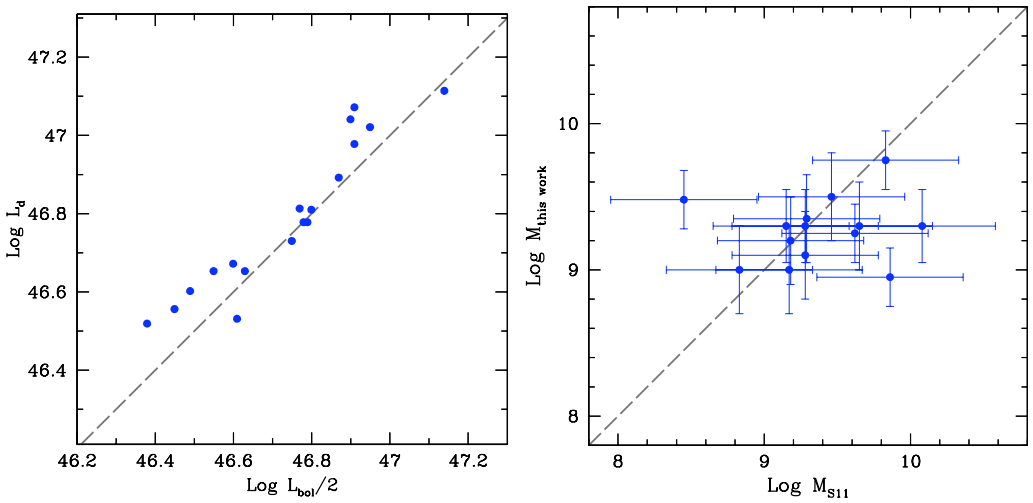

Figure 4.3: Comparison of canonical estimates of L_d and M_{BH} with our results. *Left:* the disc luminosity we obtain with the accretion disc fitting compared to half the bolometric luminosity (Calderone et al. 2013) as derived by Shen et al. (2011). B2 1023+25 is not included in this plot, since its redshift excludes from the SDSS wavelength window all the wavelengths from which the bolometric luminosity is typically derived (Richards et al. 2006). *Right:* Values of the black hole masses as derived in this work with the accretion disc fitting (along with our error), compared with the virial masses derived by Shen et al. (2011). This plot shows only the 14 objects with redshift that allows the virial black hole mass estimate. The 5 candidates with the highest redshift do not show the CIV broad line in the SDSS wavelength interval. We assigned to the virial masses an average uncertainty of a factor 3.5 (Vestergaard & Peterson, 2006). Note that the distribution of our M_{BH} estimates is definitely less dispersed than the distribution of the virial results (as can be clearly seen in Fig. 4.4. Our results show no systematics with respect to the results obtained by Shen et al. (2011).

minosities, but they are clearly linearly correlated. This represents a further confirmation of the “naked" accretion disc. If the observed flux used to derive L_{bol} was a combination of the emissions from the accretion disc and an additional component, e.g. the synchrotron emission, it would not be a good tracer of the accretion disc emission. In that case, it would not be so tightly correlated with our estimate of the overall accretion disc luminosity, that suffers less from possible contaminations, being directly derived from the peak of the disc emission.

4.2.2 Black Hole Mass Estimates

The black hole mass is a key feature to describe the quasars in our sample. The high redshift, however, introduces some difficulties in applying the commonly used virial method. Indeed, the CIV line is present only for $z < 4.7$ in the SDSS spectral range, hence it is not possible to obtain the virial masses for the whole sample. Therefore, to derive the $M_{\rm BH}$ coherently for all our objects, we fit the IR–optical–UV SED with a Shakura–Sunyaev model of radiatively efficient accretion disc (Section 2.2.3).

As mentioned above, the extreme power of these objects ensures that the synchrotron hump is at frequencies low enough to leave “naked" the spectrum produced by the accretion disc, that peaks in the optical–IR band. This allows us to directly derive the disc luminosity $L_{\rm d}$ of all our sources [i.e. $L_{\rm d} = 2\nu_{\rm p} L_{\nu_{\rm p}}$, where $\nu_{\rm p}$ is the peak frequency of the disc spectrum (Calderone et al. (2013)].

With the total disc luminosity fixed by the νL_ν peak, we are left with only the black hole mass as a free model parameter. In a multicolor blackbody model, for a fixed value of the disc luminosity, the black hole mass affects only the peak frequency (see Figure 2.5), since it determines the emitting surface and its temperature. In other words, a larger black hole mass implies a larger disc surface, that needs to be colder to emit a fixed $L_{\rm d}$. This implies a rigid shift of the νL_ν peak towards smaller frequencies. Therefore, if the overall disc luminosity is determined through the $\nu_{\rm p} L_{\nu_{\rm p}}$, it is straightforward to estimate the black hole mass, with a good sampling of the optical–NIR energy range.

We have derived the black hole mass for all the sources in our sample. Figures B.2, B.2 and B.3 show the SEDs of our objects together with three models with same disc luminosity (fixed thanks to the visibility of the emission peak; see Section 2.2.3) but different masses. The lowest and highest masses indicate the uncertainty associated to the measurement errors, possible presence

RA DEC	z	$\log L_{\rm d}$	$\log M_{\rm S11}$	$\log M_{\rm SED}$
[1]	[2]	[3]	[4]	[5]
021043.16 -001818.4	4.733	46.98	-	9.25±0.25
030437.21 +004653.5	4.305	46.53	9.65	9.30±0.30
085111.59 +142337.7	4.307	46.89	-	9.45±0.30
091824.38 +063653.3	4.192	47.07	9.83	9.75±0.20
102623.61 +254259.5	5.3035	46.95	-	9.45±0.20
103717.72 +182303.0	4.051	46.56	8.45	9.48±0.20
105320.42 -001649.7	4.304	47.04	8.83	9.00±0.30
123503.03 -000331.7	4.723	46.52	9.18	9.50±0.30
130738.83 +150752.0	4.111	46.78	9.62	9.25±0.20
131121.32 +222738.6	4.612	46.60	9.29	9.55±0.30
132512.49 +112329.7	4.412	47.11	9.46	9.50±0.30
141209.96 +062406.9	4.467	47.02	9.86	8.95±0.20
142048.01 +120545.9	4.034	46.73	9.28	9.30±0.25
143003.96 +144354.8	4.834	46.65	10.08	9.30±0.25
143413.05 +162852.7	4.195	46.78	9.17	9.00±0.30
145212.86 +023526.3	4.889	46.67	-	9.40±0.30
152028.14 +183556.1	4.123	46.81	9.28	9.10±0.30
165913.23 +210115.8	4.784	46.65	-	9.60±0.30
222032.50 +002537.5	4.205	46.65	9.15	9.30±0.25

Table 4.6: Sources from the DR7 Quasar Catalog with $z > 4$ and radio–loudness $R > 100$, seen by GROND. Col. [1]: right ascension and declination (i.e. SDSS name: "SDSS J..."); Col. [2]: redshift; Col. [3]: logarithm of the disc luminosity in $\mathrm{erg\,s^{-1}}$, as derived in this work; Col. [4]: logarithm of the BH mass, as derived by Shen et al. 2011 (solar masses); Col. [5]: logarithm of the BH mass as derived in this work (solar masses), with the confidence interval.

of other contributions, and non strict simultaneity of the data. The best values of the black hole masses we derived are listed in Table 4.6. The indicated errors are not formal errors, but the mass range determined by applying the three models to the same data.

Since our sample is composed of highly luminous sources, given the survey flux limit and the high redshift, we expect a large black hole mass, if the objects emit at some large Eddington fraction, but do not exceed the Eddington limit. This is indeed what we find: all quasars in our sample host black holes with masses $M_{\rm BH} > 10^9 M_\odot$. The red histogram in Figure 4.4 shows the distribution of masses that we obtain for our sample using the fitting method. Our results are distributed on a lognormal distribution, with an average value:

$$\left\langle \log \frac{M_{\rm BH}}{M_\odot} \right\rangle_{\rm this\,work} = 9.31 \pm 0.21 \tag{4.6}$$

The blue histogram shown in Figure 4.4 corresponds to the values of the black hole mass derived by Shen et al. (2011) through the virial method (namely, through the FWHM of the CIV line).

$$\left\langle \log \frac{M_{\rm BH}}{M_\odot} \right\rangle_{\rm S11} = 9.37 \pm 0.43 \tag{4.7}$$

Comparing the two distributions, despite the paucity of objects, we note that the average value is the same, but the dispersion obtained with the accretion disc fitting method is smaller. The difference in dispersion is evident from the right panel of Figure 4.3, too. This plot compares directly our $M_{\rm BH}$ estimates with the virial results (we include only the 14 sources for which Shen et al. (2011) were able to virially derive $M_{\rm BH}$). The large dispersion of the virial results prevents us from a clear “source by source" comparison, but it is reasonable to assess that no systematic error seems to affect our estimates with

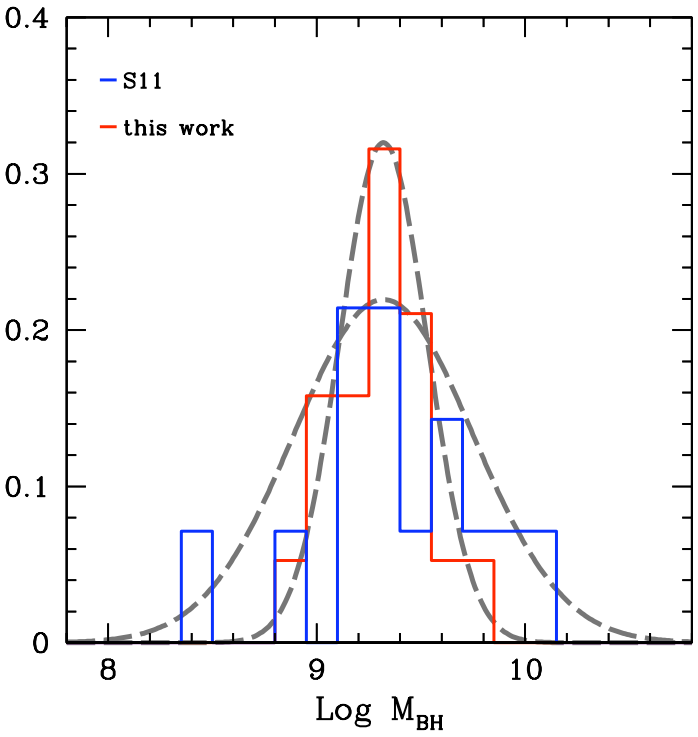

Figure 4.4: Normalized distribution of the black hole masses of the quasars in our sample. In blue, the histogram of the results obtained by Shen et al. (2011) in their work. In red, our results. The dashed lines are best fit log–normal distributions, with values: $\langle \log M_{\rm BH}/M_{\odot} \rangle = 9.37$; $\sigma = 0.43$ (blue histogram, results by Shen et al. 2011), $\langle \log M_{\rm BH}/M_{\odot} \rangle = 9.31$; $\sigma = 0.21$ (red histogram, this work).

respect to the virial black hole mass estimates. Nevertheless, the great difference between the dispersions of the two methods is clearly an interesting issue.

It is worth noticing that, once we assume an accretion disc model, the uncertainty of this method is strictly linked to the data uncertainties (i.e. the larger the data errors, the less constrained our estimate). The wavelength coverage that we have in the IR–optical–UV band and the good precision of the available data, allow us to achieve an **uncertainty of a factor of two**. Note that, in principle, we can obtain even more precise results with more accurate data. In the virial method, instead, the precision of the mass esti-

mates are driven by the uncertainties of the calibrating model, that cannot be reduced below a factor 3–4 (Vestergaard & Peterson, 2006; see Section 2.2.2). Furthermore, the FWHM of the broad emission lines could be affected by two systematic effects. The first is related to the geometry of the BLR. If the clouds forming the BLR are distributed in a flattened geometry, their FWHM would be viewing angle dependent, being smaller for small viewing angles (Decarli, Dotti & Treves 2011). In turn, small viewing angles are expected for sources with a large radio–loudness. Therefore, if such an effect plays a role, our sources would have virial black hole mass estimates that are systematically smaller than what derived from the same sources viewed at larger angles. Note however that in our sample only the broad CIV line is used to virially derive $M_{\rm BH}$, that is the line less affected by this geometric effect (Decarli, Dotti & Treves 2011). Anyway, our accretion disc fitting is much less viewing angle dependent, and thus the comparison between the two black hole mass distributions can tell something about the BLR geometry.

The second effect concerns the effect of radiation pressure upon the line emitting clouds, as discussed by Marconi et al. (2008, 2009). Accounting for this extra force makes the virial estimate of the black hole mass larger, and more so for near–Eddington disc luminosities. Again, if the Shakura–Sunyaev disc is a reasonable description of the reality even at luminosities near Eddington, then the estimate of the black hole mass is independent of the disc to Eddington luminosity ratio $L_{\rm d}/L_{\rm Edd}$.

The comparison of the two black hole mass distributions gives these important results:

The average black hole mass is the same This suggests that the effect of both a flattened distribution of the clouds and/or the radiation pressure of the disc radiation play a small role. What inhibits a stronger conclu-

sion is only the small number of objects, but this issue surely deserves some attention in the future, when larger samples will be available.

The intrinsic width of the distribution must be narrow As explained above, the virial method relies on calibrating some scaling relation, as the size–luminosity relation, whose intrinsic scatter does not allow a determination of the black hole mass more accurate than a factor 3 or 4. The disc fitting method, instead, does not suffer from these limitations, but depends only on the precision of the data. For our sources, on average, we can assign an uncertainty of a factor 2. Figure 4.4 shows indeed that our results are less dispersed than the results obtained by Shen et al. (2011). Each observed dispersion ($\sigma_{\rm obs}$) is actually the convolution of the intrinsic dispersion of the black hole masses ($\sigma_{M_{\rm BH}}$) with the typical error that is done during each of the two measurements ($\sigma_{\rm err}$):

$$\sigma^2_{\rm obs} = \sigma^2_{M_{\rm BH}} + \sigma^2_{\rm err}. \tag{4.8}$$

Therefore, with two different observed distributions, we could be able to estimate the intrinsic dispersion of masses in our sample.

Bearing in mind that the sample is composed by only 19 objects, and that Shen et al. (2011) obtained virial black hole masses for only 14 of these sources, we can compare the observed dispersions obtained by Shen et al. (2011) ($\sigma^{\rm S11}_{\rm obs} = 0.43$) with our dispersion ($\sigma^{\rm this\,work}_{\rm obs} = 0.21$). They are of the same order of the typical errors of the two methods ($\sigma^{\rm S11}_{\rm err} \sim 0.4-0.5$ and $\sigma^{\rm this\,work}_{\rm err} \sim 0.2-0.3$). This suggests a narrow intrinsic distribution. This result has to be considered carefully. First of all, we still have too few objects to draw statistically relevant conclusions. Moreover, the distribution of masses that we obtain could be affected by

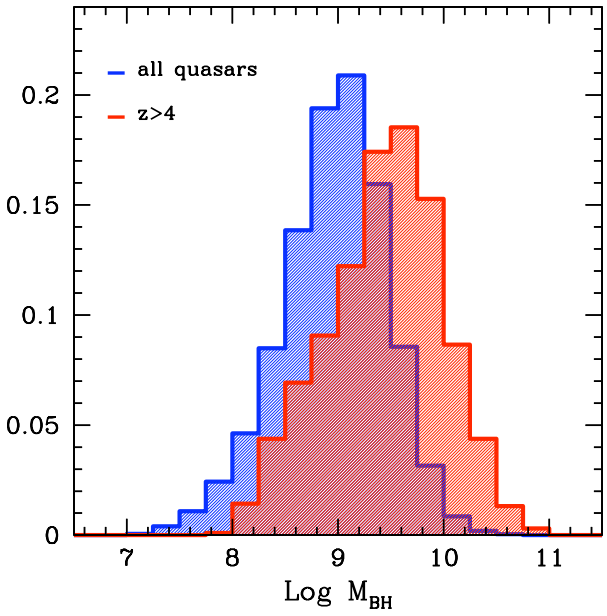

Figure 4.5: Normalized distributions of black hole masses of all the quasars studied by Shen et al. (2011; blue histogram), and only the objects at $z > 4$ (red histogram). The black hole masses are estimated with virial methods. Note that the average masses are significantly different ($\langle \log M_{\rm BH}/M_\odot \rangle_{\rm all} \sim 9$, $\langle \log M_{\rm BH}/M_\odot \rangle_{z>4} \sim 9.5$).

a selection effects. In fact, our selection criteria collect the most luminous radio–loud quasars from the SDSS, that are likely composed of the “tip of the iceberg" of the quasar population at high redshift. Since it is reasonable to expect that the most luminous are also the most massive quasars, our sample likely includes the objects with the most extreme black hole masses. This selection effect may partially justify the narrowness of the intrinsic distribution. Bearing this in mind, we can conclude that our small sample leads to the suggestion that the **extremely radio–loud quasars located at $z > 4$, and present in the SDSS, tend to have the same black hole mass, always larger than $10^9 M_\odot$.**

To confirm that our $z > 4$ quasars have larger masses than the average, we can compare our sample with the entire SDSS Quasar Catalog (analyzed

by Shen et al. 2011) without any cut in redshift. Figure 4.5 shows the $M_{\rm BH}$ normalized distribution for the whole sample and for only the $z > 4$ quasars (red and blue histograms, respectively). In this case, the masses are derived by Shen et al. (2011) through virial methods. The two distributions peak at significantly different values, $\langle \log M_{\rm BH}/M_{\odot} \rangle_{\rm all} \sim 9$ and $\langle \log M_{\rm BH}/M_{\odot} \rangle_{z>4} \sim 9.5$, respectively. Note that these two average values are also different from the average mass value found in our sample ($\langle \log M_{\rm BH}/M_{\odot} \rangle \simeq 9.3$, see Figure 4.4). Figure 4.5 shows that both the whole sample and the $z > 4$ quasars are characterized by black hole mass distributions with $\sigma_{\rm obs} \gtrsim 0.5$, i.e. more than the typical error that occurs during the measurement. The distributions shown in Figure 4.5 are broader than what we find for our sample of blazar candidates. We can further compare these results with the black hole mass distributions of Narrow–Line Seyfert 1 galaxies studied by Calderone et al. (2013), and *Fermi* blazars distributed at lower redshift analyzed by Ghisellini & Tavecchio (2014). All these subsamples selected from the SDSS Quasar Catalog are characterized by different average black hole masses, with different distribution widths.

We conclude that our selection of extremely radio–loud, $z > 4$ quasars is biased towards larger masses than the average observed at all redshift. This can justify the narrowness of our black hole mass distribution.

4.2.3 A first glance at the other high–z AGN

Other than comparing our results to the virial–based ones obtained by Shen et al. (2011) on the same small sample, we can also focus on where our sources are located, compared to the disc and black hole properties of radio–loud and radio–quiet AGN at $z > 4$. In the large SDSS DR7 Quasar Catalog studied by Shen et al. (2011), in fact, the vast majority of the sources are radio–

quiet. Therefore, a comparison between radio–loud and radio–quiet quasars included in the SDSS spectroscopic survey can be performed. Figure 4.6 shows this comparison: it shows the overall disc luminosity as a function of the black hole mass for the objects in our sample, as measured both by Shen et al. (2011; blue squares) and with our method (red dots), compared with all the radio–quiet AGN studied by Shen et al. (2011; yellow dots) above $z = 4$. For the data obtained by Shen et al. (2011), to estimate the disc luminosity we used half the bolometric luminosity calculated in their work, following Richards et al. (2006) and Calderone et al. (2013).

Same thermal emission from radio–loud and radio–quiet AGN Figure 4.6 shows that there are *no intrinsic differences between high–z radio–loud and radio–quiet AGN in their black hole mass and accretion luminosities*. Therefore the thermal emission from the accretion disc and the mass of the central black hole of AGN, in presence or absence of a jet, do not seem to differ.

Extremely radio–loud AGN at high redshift have high accretion rates Figure 4.6 illustrates also the range of accretion rates of the objects in our sample, in units of the Eddington one. The two grey dashed lines in fact correspond to the Eddington rate ($L_{\rm d} = L_{\rm Edd}$) and a hundredth of Eddington ($L_{\rm d} = 10^{-2} L_{\rm Edd}$). They are generally considered as the two physical limits of a radiatively efficient accretion operated by a Shakura–Sunyaev accretion disc. Note that two extremely radio–loud objects, with the data obtained by Shen et al. (2011), have a super–Eddington accretion rate. On the contrary, our results never exceed this limit. This suggests that at least in these cases our method is more reliable. It is also clear from Fig. 4.6 that *all our sources have high accretion rates*. Thus our sources, besides having a relatively large black hole mass,

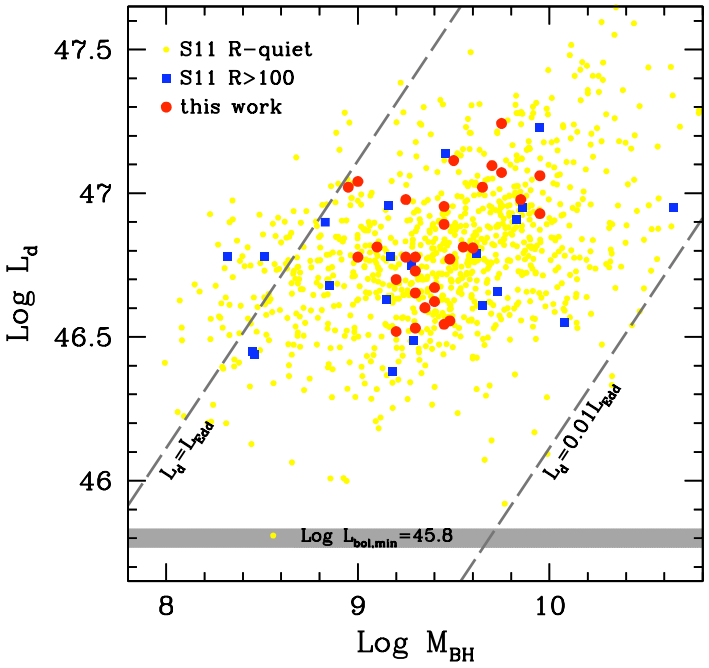

Figure 4.6: Disc luminosity as a function of the black hole mass, both in logarithmic scale. Blue squares are the results obtained by Shen et al. (2011) for the objects in our sample. Specifically, the $M_{\rm BH}$ is obtained with virial methods, while the $L_{\rm d}$ is half the bolometric luminosity derived as in Richards et al. (2006) (Calderone et al. 2013). Red dots are the results of the method used in this work for the 19 objects in our sample. Yellow dots are all the $z > 4$ radio–quiet AGN included studied by Shen et al. (2011), with $L_{\rm d} = L_{\rm bol}/2$. The grey stripe highlights the minimum luminosity measured by Shen et al. (2011) among the radio–quiet AGN. The dashed lines indicate accretion regimes at the Eddington rate and at a hundredth of Eddington rate, as labelled. Note that Shen et al. (2011) obtain disc luminosities larger than the Eddington limit.

$[\log(M_{\rm BH}/M_{\odot}) = 9.3]$, accrete at ∼10% Eddington, on average. High rates of accretion could justify the presence of many extremely massive black holes at high redshift, that perhaps are just ending the “fast growing age" through accretion at the Eddington rate. Indeed, the formation and growth of the first supermassive black hole is an open issue, that our results will hopefully help to solve.

4.3 Classification of blazar candidates

The sample of high–redshift quasars we collected, being selected through a cut in radio–loudness, preferentially includes jets roughly directed near our line–of–sight. Among them, we expect to find a number of blazar, namely sources with a viewing angle that is smaller or comparable to the jet beaming angle ($1/\Gamma$). The importance of blazar identification resides in their statistical relevance: if we knew the exact viewing angle of our sources, we could reconstruct the number density of their entire parent population. Specifically, if a source has a viewing angle smaller than the jet beaming angle, and its Lorentz factor Γ is known thanks to modeling or superluminal motion, we would be able to derive the total number of analogous objects. This is in fact the final goal of our whole project.

To classify a source as a blazar, and derive a reliable estimate of the viewing angle of its jet and its beaming factor, we need to characterize the high–energy component of the jet emission, that is more sensitive to orientation and beaming (see Section 4.3.2). This is not as easy as it is at low redshift. At $z > 4$, in fact, we expect to find only the most powerful sources of their kind. Therefore, their non–thermal emission peaks at small frequencies, if they follow the blazar sequence (Section 1.2.1). This effect is enhanced by the high redshift itself. *Fermi*/LAT cannot detect them any longer, because the emission does not peak in LAT energy range. X–ray data are therefore needed to map the first part of the high–energy SED component. We used *Swift*/XRT (Burrows et al. 2005) and *NuSTAR* (Harrison et al. 2010) to study some of our candidates and derive their orientation details.

We identified as blazars the highest–redshift quasar of our sample (B2 1023+25, $z = 5.3$; Sbarrato et al. 2012b; 2013b) and three sources in the $4 < z < 5$ redshift bin (SDSS J142048.01+120545.9, SDSS

J222032.50+002537.5 and PMN J2134–0419; Sbarrato et al. 2014a). The details of each source classification are described in the following Sections. In the frame of our selection and classification method, another highly radio–loud high–redshift quasar was classified as a blazar by our group. SDSS J114657.79+403708.6 ($z = 5$; Ghisellini et al. 2014b) is not included in our sample of blazar candidates since it is not visible from La Silla (where GROND is), but is included in the SDSS+FIRST survey. Therefore it is relevant to study the distribution of highly massive jetted systems in the early Universe (Section 5.2).

4.3.1 B2 1023+25: the second most distant blazar known

SDSS J102623.61+254259.5 (= B2 1023+25) is the best blazar candidate from this list, because of its very high redshift and extreme radio–loudness ($R \sim 5200$). The precise value of the redshift is somewhat uncertain, since it is $z = 5.284$ in NED, taken from the 6th Data Release of the Sloan survey (DR6), while $z = 5.3035$ in DR7, and $z = 5.266$ in DR8. In this paper we assumed therefore a value of z=5.3. This is a known quasar, observed for the first time in the B2 Catalog of radio sources (Colla et al. 1972). The radio position of this source is RA=10h26m23.62s, DEC=+25d42m59.4s and, according to the CRATES All–Sky Survey (Healey et al. 2007), the source has a flat spectrum with $\alpha_{1.4/4.8} = 0.489$ [between 1.4 and 4.8 GHz; $F(\nu) \propto \nu^{-\alpha}$] and $\alpha_{1.4/8.4} = 0.504$ with a radio flux of $F_{1.4\mathrm{GHz}} = 260.7$mJy and $F_{8.4\mathrm{GHz}} = 105.7$ mJy. We retrieved a number of radio fluxes from ASDC. Moreover, B2 1023+25 is included in the WISE All–Sky Source Catalog[3], with clear detections in the two bands at lower wavelengths of the instrument, i.e. $\lambda = 3.4\mu$m and $\lambda = 4.6\mu$m.

[3]Data retrieved from http://irsa.ipac.caltech.edu/

We retrieved and analyzed *Fermi*/LAT data collected in the period 2008 August 4th – 2012 June 14th ($\sim$ 3.8 yrs). Photons of class 2 ("source"), with energies in the range 0.1–100 GeV, collected in a region of 10° radius from the source position, were analyzed by using LAT Science Tools v. 9.27.1, Instrument Response Function P7, and the corresponding background maps. The followed procedures are described in detail in the analysis threads of the *Fermi* Science Support Center[4]. Particularly, B2 1023+25 was fitted with a power law model, together with any other source of the 2FGL catalog (Nolan et al., 2012) within 10° from their sky coordinates. The analysis resulted in no detection, with a 5σ upper limit on the photon flux above 100 MeV of 3.0×10^{-9} ph cm^{-2} s^{-1}.

Since B2 1023+25 is our best blazar candidate, we first requested a Target of Opportunity (ToO) observation from the *Swift* team, in order to have X–ray data to confirm our hypothesis. A longer observation performed simultaneously with *NuSTAR* and *Swift* allowed a reliable classification of this object as a blazar, specifically the second most distant blazar known after Q0906+6930 (Romani et al. 2004; Romani 2006).

$L_{\rm d}$ and $M_{\rm BH}$ estimates

To reliably derive the black hole mass for B2 1023+25, we can assume that the optical–IR luminosity is emitted from the accretion disc, and fit its emission with a standard Shakura–Sunyaev model, as detailed in Section 2.5. The two fitting parameters are $L_{\rm d}$ and $M_{\rm BH}$ itself. The disc luminosity can be calculated in two different ways, as already explained: through the broad line region emission and from the peak luminosity of the spectrum.

B2 1023+25 shows a prominent broad Lyα, that unfortunately is absorbed

[4] http://fermi.gsfc.nasa.gov/ssc/data/analysis/

in its blue wing. Using only the red wing, and subtracting the continuum in the same frequency range (adopting a power law model), we derive $L_{\mathrm{Ly}\alpha} \sim 2 \times 10^{45}\,\mathrm{erg\,s^{-1}}$ and a FWHM=4000 km $\mathrm{s^{-1}}$. These are twice the values we measured for the red wing only, implicitly assuming that the line is intrinsically symmetric. The ratio between the entire BLR luminosity and $L_{\mathrm{Ly}\alpha}$ has been calculated by Francis et al. (1991) and Vanden Berk et al. (2001). The former gives a $L_{\mathrm{BLR}}/L_{\mathrm{Ly}\alpha} = 5.55$, while the latter gives a $L_{\mathrm{BLR}}/L_{\mathrm{Ly}\alpha} = 2.7$. Therefore $L_{\mathrm{BLR}} \sim$(5–10)$\times 10^{45}$ erg $\mathrm{s^{-1}}$. Finally, assuming a covering factor (i.e. amount of re–emitted light) $C = 0.1$, the estimate for the disc luminosity is $L_{\mathrm{d}} \sim$(5–10)$\times 10^{46}$ erg $\mathrm{s^{-1}}$.

Another option to estimate L_{d} is to derive peak luminosity of the accretion disc emission. The rather good set of IR–optical data obtained for B2 1023+25 shows that the peak of the disc emission is at frequencies just below the absorption caused by intervening clouds (see Figure 4.2). Since the overall L_{d} is about twice the νL_ν peak luminosity, we directly derive $L_{\mathrm{d}} \simeq 9 \times 10^{46}\,\mathrm{erg\,s^{-1}}$. Although the estimate derived from L_{BLR} is affected by relevant uncertainties (e.g. partially absorbed Lyα line and uncertain value of C), the range we estimate through that method encompasses the value found with the disc–fitting method.

Once L_{d} is derived, we are left with M_{BH} as the only remaining free parameter for a Shakura–Sunyaev accretion disc model. For a given $\dot{M}$, the black hole mass determines the peak frequency of the disc emission. A larger mass implies a larger disc surface and hence a lower temperature emitting a given luminosity. Therefore, for a fixed L_{d}, a larger M_{BH} shifts the peak to lower frequencies. Then the best agreement with the data fixes M_{BH}. We adopt $L_{\mathrm{d}} = 9 \times 10^{46}$ erg $\mathrm{s^{-1}}$, as discussed above, and calculate the overall spectrum from a standard Shakura & Sunjaev (1973) disc. Figure 4.2 shows the data

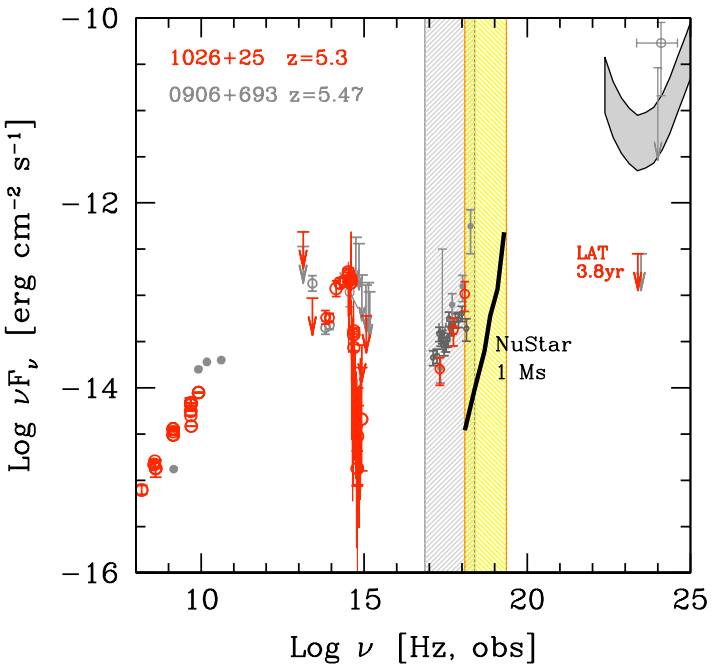

Figure 4.7: Comparison between the SEDs of B2 1023+25 (red symbols) and Q0906+6930 (grey symbols). As can be seen, the two sources are very similar. The grey vertical stripe marks the [0.3–10 keV] energy range of XRT, while the yellow vertical stripe corresponds to the [5–80 keV] energy range of the *NuSTAR* satellite. The curved grey stripe corresponds to the sensitivity of *Fermi*LAT after 1 yrs of operation (5σ, lower bound) and of 3 months ($10\ \sigma$, upper bounds). We show the expected (pre–launch) sensitivity (3σ) of the *NuStar* satellite for an exposure of 1 Ms.

in the IR–optical band (as labelled) and three disc emission spectra calculated assuming the same $L_{\rm d}$ and three different mass values: $M_{\rm BH} = 4.5 \times 10^9 M_\odot$ (green line), $2.8 \times 10^9 M_\odot$ (blue) and $1.8 \times 10^9 M_\odot$ (cyan). Figure 4.2 shows that, outside this range of masses, the model does not satisfactory reproduce the data any longer.

First X–ray observation: comparison with Q0906+6930

We first requested a ToO observation of B2 1023+25, to have a first hint of its X–ray spectrum. The *Swift* satellite observed B2 1023+25 twice: on 2012, June 21st (ObsID: 00032500001) and on 2012, June 22nd (ObsID:

00032500002). Data of the X–ray Telescope (XRT, Burrows et al. 2005) and the UltraViolet Optical Telescope (UVOT, Roming et al. 2005) were downloaded from HEASARC public archive, processed with the specific *Swift* software included in the package `HEASoft v. 6.12`[5], and analysed. The calibration database used for these data was updated on July 16, 2012. We did not consider the data from BAT, given the weak X–ray flux.

The total exposure on the XRT was of ∼10 ks and resulted in 26 counts. Given the low statistics, the fit with a power law model with Galactic absorption ($N_{\rm H} = 1.50 \times 10^{20}$ cm^{-2}, Kalberla et al. 2005) was done by using the likelihood (Cash 1979). The output parameters of the model were $\Gamma = 1.1 \pm 0.5$ and an integrated observed flux $F_{0.3-10\,\rm keV} = (1.7 \pm 0.4) \times 10^{-13}$ erg cm^{-2} s^{-1} (de–absorbed). UVOT observed the source with two filters only: U, with 8.4 ks exposure, and $UVW1$, with 1.6 ks. Both resulted in no detection with 3σ upper limits of the observed magnitudes equal to 21.70 and 20.76 mag, respectively.

Figure 4.7 shows how the SED of B2 1023+25 compares with the SED of Q0906+693. As can be seen, the two SEDs are very similar. The only, remarkable, difference could be in the γ–ray band, if the tentative EGRET association with Q0906+6930 is real. On the other hand, the upper limits of *Fermi*/LAT are the same for the two sources. This may suggest that the EGRET flux is not produced by Q0906+6930, although variations of even more than two orders of magnitude of the γ–ray flux are not uncommon for blazars (see e.g. Abdo et al. 2011; Ghirlanda et al. 2011).

Figure 4.7 shows, as vertical stripes, the energy bands of XRT and of *NuSTAR*. We report also the pre–launch estimated *NuSTAR* sensitivity for an exposure of 1 Ms. We noticed that both sources have an X–ray flux lying one order

[5]Including the XRT Data Analysis Software (XRTDAS) developed under the responsibility of ASDC.

of magnitude above the *NuSTAR* sensitivity, making their detection possible even with a moderate exposure time, and even at the high energy limit of the instrument, i.e. at ∼80 keV. Note that 80 keV correspond, in the rest frame of a $z = 5.3$ source, to ∼500 keV, that could be rather close to the peak of the high energy emission. For this reason, we observed B2 1023+25 with *NuSTAR*, as detailed in the following.

NuSTAR observational campaign

The *NuSTAR* observations were carried out during an observational campaign that also involved *Swift*, GROND and two radio instruments: the Combined Array for Research in Millimeter–wave Astronomy (CARMA; Bock et al. 2006) and the 40–meter telescope at the Owens Valley Radio Observatory (OVRO). CARMA observed at 31 and 91 GHz (1 cm and 3 mm), while OVRO provided data at 15 GHz (2 cm). To these data, we added a previous *Chandra* observation (Wu et al. 2013), to increase the statistics of the soft–X energy band, WISE IR photometry and archival data from NED and ASDC. The observations and data reductions are presented in the following[6].

NuSTAR The *NuSTAR* satellite observed B2 1023+25 beginning on UT 2012 December 31 (sequence 60001107002) for a net exposure time of 59.3 ks. The two data sets obtained with the *NuSTAR* Focal Plane Modules A and B (FPMA and FPMB) were first processed with the NuSTARDAS software package (v.1.2.0) jointly developed by the ASDC and the California Institute of Technology (Caltech). Event files were calibrated and cleaned with standard filtering criteria with the `nupipeline` task using version 20130509 of the *NuSTAR* Calibration Database (CALDB).

[6]The observations and data reductions were carried out by various collaborators, and therefore I am reporting the procedures as described in Sbarrato et al. 2013b.

The FPMA and FPMB spectra were extracted from the cleaned event files using a circular aperture of 12 pixel ($\sim$ 30") radius, while the background was extracted from two distinct nearby circular regions of 30 pixel radius. The ancillary response files were generated with the `numkarf` task, applying corrections for the PSF losses, exposure maps and vignetting. The source was detected up to 20 keV, and the source spectrum in the $4-20$ keV energy band was formed from a total of 79 counts (of which ~ 44 are from the background) for FPMA and 113 counts (of which ~ 58 are from the background) for FPMB. Both spectra were binned to ensure a minimum of 1 count per bin.

Swift The *Swift* satellite observed the source three times: on UT 2012 June 21 (sequence 00032500001), on UT 2012 June 22 (sequence 00032500002) and on UT 2012 December 31 (sequence 00080499001). All XRT observations were carried out using the most sensitive Photon Counting (PC) readout mode.

The XRT data set was first processed with the XRTDAS software package (v.2.8.0) developed at the ASDC and distributed by HEASARC within the HEASoft package (v. 6.13). Event files were calibrated and cleaned with standard filtering criteria with the `xrtpipeline` task using the latest calibration files available in the *Swift* CALDB.

The spectra obtained from the single observations are perfectly consistent, with an uncertainty on each measurement of $\sim 20-25\%$, showing no variability among the three observations. We therefore merge the individual XRT event files, using the XSELECT package for a total net exposure time of 20.3 ks. Next we extracted the average spectrum from the summed cleaned event file. Events for the spectral analysis were selected within a circular aperture of 10 pixel ($\sim$ 23") radius, which

encloses about 80% of the PSF, centered on the source position. The background was extracted from a nearby circular region of 100 pixel radius. The ancillary response files were generated with the `xrtmkarf` task applying corrections for the PSF losses and CCD defects using the cumulative exposure map. The latest response matrices available in the *Swift* CALDB were used. The source spectrum in the $0.3-10$ keV energy band was formed from a total of 41 counts (of which ~ 3 are from the background) and it was binned to ensure a minimum of 1 count per bin.

Chandra B2 1023+25 was observed by *Chandra* on 2011 March for a total of ∼5 ksec with the ACIS camera. These data were presented in Wu et al. (2013). In order to use them together with our other data sets, we re–extracted the *Chandra* spectrum. The data were reduced with the CIAO 4.4 package (Fruscione et al. 2006) using the *Chandra* CALDB version 4.4.7, adopting standard procedures. The source spectrum was extracted in a circular region centered on the peak of the X-ray source emission and with a radius of 3". The background spectrum was extracted from four circular regions with ∼5" radii, located around the source. The source spectrum in the $0.5-7$ keV energy band was formed by a total of 54 counts (of which ~ 1 is from the background) and it was binned to ensure a minimum of 1 count per bin.

GROND We started observing B2 1023+25 with GROND on UT 2013 January 1 at 07:38:43 UTC. We carried out three 8–minute observations simultaneously in all seven bands for a total exposure time of 1379 s in the optical and 1440 s in the NIR bands. Observations were carried out at an average seeing of 1.2" evaluated from the r'–band image, and at an average airmass of 1.8. Table 4.7 reports the observed AB magnitudes, not

	g'	r'	i'	z'	J	H	K_s
$\lambda_{\rm eff}$ (Å)	4587	6220	7641	8999	12399	16468	21706
$m_{\rm AB}$	>23.4	22.16±0.16	19.91±0.04	19.73±0.03	19.52±0.06	19.20±0.09	19.35±0.24

Table 4.7: GROND AB observed magnitudes ($m_{\rm AB}$) of B2 1023+25, taken on UT 2013 January 1 (magnitudes not corrected for Galactic extinction). The first row gives the effective wavelength of the filter (in Angstroms).

corrected for the Galactic extinction of $E(B-V) = 0.02$ from Schlegel et al. (1998). Note that these data are fully consistent with those carried out during the observational campaign for our sample of candidates (see Section 4.1.1 and Table 4.5), showing that the thermal emission of the source did not vary between the two observing times.

CARMA We observed B2 1023+25 at 31 and 91 GHz (1 cm and 3 mm bands, respectively) with CARMA. The observations were carried out simultaneously with the *NuSTAR* observation on UT 2013 January 1, with the array in the SL configuration. This configuration includes eight 3.5-meter antennae on baselines of 5 to 85 meters. Single sideband receivers were used to observe the upper and the lower sideband at 3 mm and 1 cm, respectively, and the correlator was configured to process 8 GHz of bandwidth. After flagging the bad data intervals, the total observation time was 3 hours in each band. Strong nearby sources 0956+252, 0927+390 and planet Jupiter were used as gain, passband and flux calibrators. The data were processed using the Multichannel Image Reconstruction Image Analysis and Display (MIRIAD; Sault, Teuben & Wright 1995) software, optimized for CARMA. The observations reached an RMS of 0.7 (1.5) mJy in the 1 cm (3 mm) band, providing a 47σ (9σ) detection of the target. The absolute flux density calibration, however, adds a systematic uncertainty of 10%, so the flux density values used in further analysis are $f_\nu(31\text{GHz}) = 33 \pm 4$ mJy and $f_\nu(91\text{GHz}) = 14 \pm 3$ mJy.

$N_{\rm H}$ ($\rm cm^{-2}$)	$F_{\rm norm}$ ($\rm ph\,cm^{-2}\,s^{-1}$)	$\Gamma_{\rm X}$	$F_{5-10\rm kev}$ ($\rm erg\,cm^{-2}\,s^{-1}$)	χ^2 / dof
1.5×10^{20} fixed	$1.29^{+0.29}_{-0.26}\times10^{-5}$	$1.29^{+0.14}_{-0.15}$	5.8×10^{-14}	230.5 / 253
$2.8^{+2.0}_{-1.7}\times10^{21}$	$2.26^{+1.16}_{-0.77}\times10^{-5}$	$1.60^{+0.27}_{-0.26}$	5.5×10^{-14}	211.3 / 252

Table 4.8: Parameters of B2 1023+25 X–ray spectral analysis, from simultaneous fit of *NuSTAR*, *Swift*/XRT and *Chandra* data. The errors are at 90% level of confidence for one parameter of interest.

OVRO The OVRO 40–meter telescope obtained a 15 GHz observation of B2 1023+25 simultaneous with *NuSTAR* on UT 2013 January 1. The telescope uses off-axis dual-beam optics and a cryogenic high electron mobility transistor (HEMT) low-noise amplifier with a 3 GHz bandwidth. The two sky beams are Dicke switched using the off-source beam as a reference, and the source is alternated between the two beams in an ON-ON fashion to remove atmospheric and ground contamination. A noise level of approximately 3–4 mJy in quadrature with about 2% additional uncertainty mostly due to pointing errors, is achieved in a 70-second integration cycle. The weighted average of 9 consecutive integrations was used to derive the 15 GHz flux density $f_\nu(15\rm GHz) = 55 \pm 4$ mJy, where the systematic uncertainty in the absolute flux calibration has already been included. Calibration is routinely achieved using a temperature-stable diode noise source to remove receiver gain drifts and the flux density scale was derived from observations of 3C 286 assuming the Baars et al. (1977) value of 3.44 Jy at 15 GHz. Details of the reduction and calibration procedure can be found in Richards et al. (2011).

A comparison of the current and previous *Swift*/XRT observations show that the source did not vary between these epochs (as is the case for the thermal emission observed in optical–IR with GROND). If we fit the data of each satellite alone, we find a good agreement among *NuSTAR*, XRT and *Chan-*

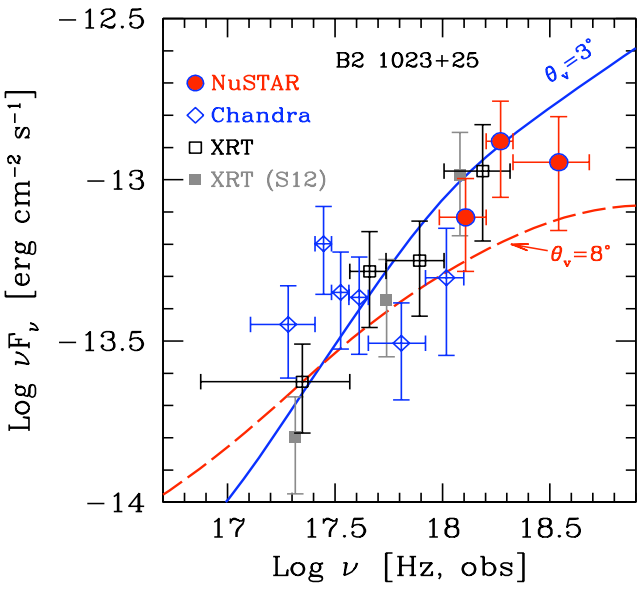

Figure 4.8: X–ray spectrum of B2 1023+25, along with the two SED models discussed in the text. *NuSTAR*/FPMB data are red circles filled in blue; *Chandra* data are blue empty diamonds, while *Swift*/XRT data are black empty squares. The solid blue line is the model with $\theta_v = 3°$, $\Gamma = 13$ and parameters as in the first row of Table 4.9. The dashed red line is the model with $\theta_v = 8°$, $\Gamma = 10$ and parameters as in the second row of Table 4.9.

dra, but due to the faintness of the source the uncertainties are quite large. Since there is no evidence for variability we performed a simultaneous fit of the *Swift*/XRT, *Chandra* and *NuSTAR* spectra using the XSPEC package, and adopting C–statistics.

In prior works the XRT and *Chandra* data were fit with a simple power law model plus Galactic absorption (see the previous section describing the ToO *Swift* observation; Sbarrato et al. 2012b; Wu et al. 2013). In the present analysis, if we leave N_H free to vary, we find a high value for the absorption and a slightly steeper spectrum than previously reported. The statistical quality of the data is, however, not sufficient to distinguish between no absorption and spectral curvature and a higher level of intervening absorption and steeper spectral index. X–ray absorption in the host of blazars is unlikely (the jet is able to completely ionize host ISM), but intervening material in high–redshift

objects could be responsible for extra absorption. The presence or absence of extra absorption due to intervening material in quasar X–ray spectra is a matter of debate (see e.g. Vignali et al. 2005; Shemmer et al. 2005; 2006; Yuan et al. 2006; for a different point of view, see Behar et al. 2011), so we investigate fits with the column both fixed to the Galactic value and free to vary. Both models provided a good description of the observed spectra (see Table 4.8). If we leave $N_{\rm H}$ free to vary, we find a high value of 2.8×10^{21} cm^{-2} assuming the absorbing material is at $z = 0$ (for higher redshift absorbers this column increases). A simple power–law plus Galactic absorption also provides an acceptable fit to the data: χ^2=230.5 for 253 degree of freedom, to be compared with χ^2=211.3 for 252 degree of freedom for the case with $N_{\rm H}$ free to vary. Although the χ^2 clearly improves when $N_{\rm H}$ is free to vary, the reduced χ^2 is already < 1 with $N_{\rm H}$ fixed to the Galactic value; therefore, we cannot discriminate between the two possibilities from a statistical point of view. The results of the spectral fits are shown in Table 4.8. The photon spectral index in the two cases varies from $\Gamma_{\rm X} = 1.29^{+0.14}_{-0.15}$ to $\Gamma_{\rm X} = 1.60^{+0.27}_{-0.26}$. In the following analysis we take this level of uncertainty in the spectral index into account, in particular in constraining the jet viewing angle. In Figure 4.8 we plot the X-ray SED of the source as derived with the spectral fit performed with $N_{\rm H}$ free to vary.

Understanding the jet orientation: B2 1023+25 blazar classification

Figure 4.8 shows the X–ray data of B2 1023+25. The X–ray SED data points were all absorption corrected and rebinned to have a 3σ detection in each bin. Note that the *Swift*/XRT data are similar to those obtained thanks to the ToO observation, since variability is negligible. Given the rapid variability seen routinely in blazars at many wavelengths, this lack of variability is

evidence that the electrons responsible for the hard X-ray emission have relatively small energies, and thus lose energy slowly. This is consistent with X–rays produced through the so–called external Compton process (Sikora et al. 1994), in which relatively cold electrons scatter broad line photons. Also the optical–UV emission is steady, but for a completely different reason. This radiation is, in fact, emitted by the accretion disk, which is not expected to vary on short timescales.

The radio part of the spectrum shows flux variability both at 5 GHz and at high frequencies (see Figure 4.9). A 43 GHz flux density measurement was published recently by Frey et al. (2013), based on a VLA A–configuration observation on UT 2002 June 19. A comparison to their $f_\nu(43\ \mathrm{GHz}) = 55 \pm 4$ mJy measurement to our CARMA measurements clearly shows that the radio flux is variable in time, as expected in blazars. The three radio data points obtained in this work define a spectral index α_r ∼0.7 ($F(\nu) \propto \nu^{-\alpha_\mathrm{r}}$), steeper than $\alpha_\mathrm{r} \sim 0.4$ reported by Frey et al. (2013). At least in part, this could be due to the fact that observed frequency of 91 GHz corresponds to ∼570 GHz in the source rest frame, likely sampling the optically thin part of the synchrotron spectrum.

Thanks to the new X–ray flux results, we confirmed the extreme radio–loudness of B2 1023+25. During the sample selection we used the canonical radio–to–optical ratio to define its radio–loudness ($R = F[5\mathrm{GHz}]/F[2500] \simeq 5200$), and this allowed to classify B2 1023+25 as the most radio–loud quasar of our sample. In addition to this, we now calculate the X–ray based radio–loudness $R_\mathrm{X} = \nu L_\nu[5\mathrm{GHz}]/L_\mathrm{X}[2-10\ \mathrm{keV}]$, using the X–ray fluxes and spectral indices listed in Table 4.8. We obtain $\log R_\mathrm{X} = -0.65$ and $\log R_\mathrm{X} = -0.72$ (for fixed and free N_H, respectively). Both values confirm the extreme radio–loudness of B2 1023+25 according to the calibration introduced by Terashima

& Wilson (2003), which classifies quasars as radio-loud if they have $\log R_{\rm X} > -4.5$.

We fit the X–ray observations using the model described in Ghisellini & Tavecchio (2009). In this model, relativistic electrons in the jet emit by synchrotron and IC processes, and their distribution is derived through a continuity equation in which we assume continuous injection, radiative cooling, possible pair production and emission. The particle distribution responsible for the emission is calculated to occur at a time R/c after the injection, where R is the size of the emitting region, located at a distance $R_{\rm diss}$ from the central engine. We observe the jet under a viewing angle $\theta_{\rm v}$ from the jet axis. Besides the jet emission, we take into account the emission from the accretion disc, the dusty torus and the hot thermal corona surrounding the disc itself. Since this is a one–zone model, which assumes that the emitting region is rather compact, it cannot account for radio emission, which in the considered region is severely self–absorbed.

Fitting the overall SED, we obtain a set of parameters describing the source and its emitting condition. Two characterizing parameters are the viewing angle $\theta_{\rm v}$ and the bulk Lorentz factor Γ of the emitting region. In our modeling we keep the parameters associated with the thermal emission from the accretion disk fixed. We assume a black hole mass $M_{\rm BH} = 2.8 \times 10^9 M_\odot$ and an accretion disk luminosity $L_{\rm d} = 9 \times 10^{46}\,{\rm erg\,s^{-1}}$, as derived previously (following the details described in Sections 2.2.3 and 4.2.2). Note that varying the black hole mass value inside the formal confidence range ($M_{\rm BH} = 1.8 - 4.5 \times 10^9 M_\odot$) does not change the results of our SED modeling. Because of the hard and bright X–ray spectrum shown by B2 1023+25, as a best fit we find a small value of $\theta_{\rm v}$ and a large Doppler boosting (i.e. large Γ). We find $\theta_{\rm v} < 1/\Gamma$, as is typical of known blazars. Hence we confirm B2 1023+25 as a blazar. Because of the

Γ [1]	θ_v [2]	R_{diss} [3]	R_{diss}/R_S [4]	P'_i [5]	B [6]	γ_b [7]	γ_{max} [8]	s_1 [9]	s_2 [10]	$\log P_r$ [11]	$\log P_B$ [12]	$\log P_e$ [13]	$\log P_p$ [14]
13	3	504	600	0.01	2.3	70	4e3	0	2.6	45.70	45.93	44.16	46.61
10	8	420	500	0.23	4.4	20	4e3	–1	2.6	46.72	46.11	45.72	48.26
5	20	588	700	7.0	5.5	2e3	4e3	–1	2.6	47.42	45.98	45.28	47.73

Table 4.9: Input parameters used to model the SED. Col. [1]: bulk Lorentz factor; Col. [2]: viewing angle (degrees); Col. [3]: distance of the blob from the black hole in units of 10^{15} cm; Col. [4]: R_{diss} in units of the Schwarzschild radius; Col. [5]: power injected in the blob calculated in the comoving frame, in units of 10^{45} erg s^{-1}; Col. [6]: magnetic field in Gauss; Col. [7] and [8]: minimum and maximum random Lorentz factors of the injected electrons; Col. [9] and [10]: slopes of the injected electron distribution [$Q(\gamma)$] below and above γ_b; Col. [11] logarithm of the jet power in the form of radiation, [12] Poynting flux, [13] bulk motion of electrons and [14] protons (assuming one cold proton per emitting electron). The spectral shape of the corona is assumed to be $\propto \nu^{-1}\exp(-h\nu/150$ keV). For all models we have assumed a radius of the broad line region of $R_{BLR} = 9.2 \times 10^{17}$ cm, a black hole mass of $2.8 \times 10^9 M_\odot$ and an accretion disk luminosity of $L_d = 9 \times 10^{46}$ erg s^{-1}, corresponding to $L_d/L_{Edd} = 0.25$.

limited statistics in the X–ray spectrum, though, we investigate the range of models consistent with the uncertainties. Therefore, in the following we also discuss a case with a larger value of θ_v and a somewhat smaller value of Γ.

Best fit: small viewing angle, large Lorentz factor In our best fit model we find a set of parameters consistent with those typical for a blazar ($\Gamma = 13$, $\theta_v = 3°$). We report these in the first line of Table 4.9 as the best fit to the broad band SED. The case in Table 4.9 corresponds to the best fit to the X-ray data with N_H free to vary. Using N_H fixed to the Galactic value yields a harder spectrum and therefore an even more extreme blazar classification. The model (blue solid line in Figures 4.8 and 4.9) describes a typical blazar, with the viewing angle smaller than the jet beaming angle ($\theta_v < 1/\Gamma$), *firmly classifying B2 1023+25 as a blazar*.

Slightly misaligned jet Figure 4.8 shows that the X–ray data have large error bars. A softer X–ray spectrum cannot be excluded at 90% confidence (see Table 4.8). A softer spectrum implies a larger viewing angle and

therefore a somewhat less extreme bulk Lorentz factor. Specifically, a viewing angle of $\theta_v = 8^\circ$ with $\Gamma = 10$ together with the other parameters in the second line of Table 4.9 still reproduce the broad–band data. The model (red solid line in Figure 4.8 and red dashed line in the top panel of Figure 4.9) represents an alternative interpretation consistent with the X–ray data points at 90% level of confidence. This viewing angle, slightly larger than the jet beaming angle $1/\Gamma$, still classifies B2 1023+25 as a blazar. As a consistency check, we test how an object with the same instrinsic (comoving) properties would look if oriented at $\theta_v = 3^\circ$, i.e. at $\theta_v < 1/\Gamma$. The re–oriented model is shown in the bottom panel of Figure 4.9 by the red dashed line. The resulting X-ray flux would be unusual but not unprecedented, being very similar, for example, to GB 1428+4217 ($z = 4.72$, Worsley et al. 2004), although the latter shows a synchrotron hump much dimmer than our “re–oriented" B2 1023+25. We conclude that $\theta_v = 8^\circ$ is the largest possible viewing angle consistent with the *NuSTAR* data.

Can the jet be at 20° from our line of sight? Frey et al. (2013) claim that a viewing angle of at least $\sim 20^\circ$ with a bulk Lorentz factor $\Gamma \sim 15$ can be inferred for B2 1023+25 from published 5 GHz Very Long Baseline Interferometry (VLBI) imaging data. We therefore attempt to fit our X–ray data with $\theta_v = 20^\circ$ to test this hypothesis. We find that the data are not consistent with both a large viewing angle and a large Lorentz factor, i.e. the values obtained by Frey et al. (2013). In this case the corresponding Doppler factor $\delta = [\Gamma(1 - \beta \cos\theta_v)]^{-1} \sim 1$, and the intrinsic jet power becomes huge, to account for the observed X–ray flux (i.e. $P_{\rm jet} \sim 10^{50}$ erg s^{-1}). In addition, the fit to the observed data is poor. The maximum bulk Lorentz factor providing a good fit to the *NuSTAR* and broad band

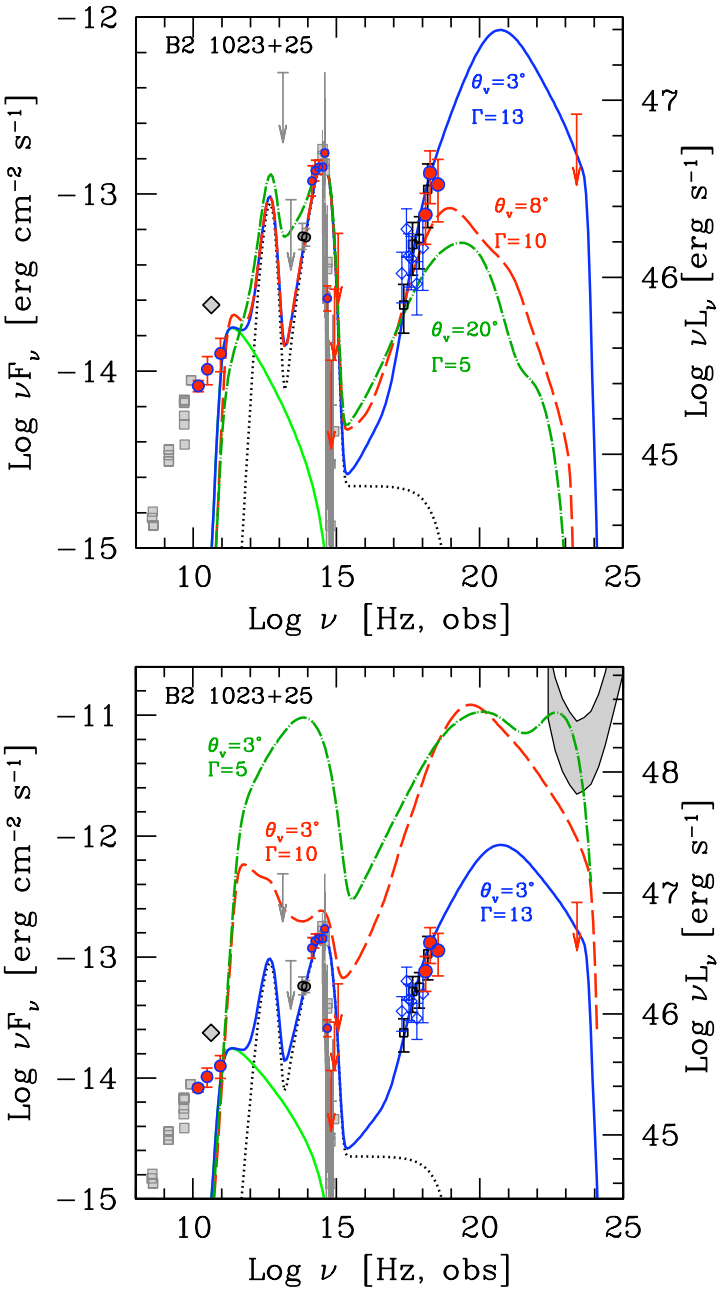

Figure 4.9: Broad–band SED of B2 1023+25 together with the models discussed in the text. Simultaneous OVRO, CARMA, GROND and *NuSTAR* data are red points circled in blue. *Chandra* data are blue empty diamonds, while *Swift*/XRT data are black empty squares. The grey filled symbols are data from literature: squares are archival data from ASDC, the diamond is the radio point from Frey et al. 2013, the circles and the two upper limits are *WISE* data, the line is the SDSS spectrum. The dotted black line is the thermal emission of the source, including the accretion disk, torus and X–ray corona emission. The *Fermi*/LAT upper limit is for 3.8 years, 5σ (red arrow). The solid blue line is the model with parameters as in the first row of Table 4.9. The dashed red lines and the dot–dashed green lines are respectively the models with parameters as in the second and third row of Table 4.9 in the *top panel*, while in the *bottom panel* they are "re–oriented" at $\theta_v = 3°$, as labelled.

data under a viewing angle of $\theta_v = 20^\circ$ is $\Gamma = 5$ (along with the parameters in the third line of Table 4.9). This model is shown in the top panel of Figure 4.9 as the green dot–dashed line. The corresponding beaming factor is $\delta \sim 2.5$. Such a modest beaming factor implies that the intrinsic luminosity would be very high. This would imply a class of objects with an extreme intrinsic luminosity. If such objects existed (at any redshift), we should see a few of them pointing at us. For illustration, we then "re–orient" B2 1023+25 to $\theta_v = 3^\circ$ (dot–dashed green line in the bottom panel of Figure 4.9). Similar SEDs have never been observed, at any redshift. All powerful blazars observed so far have the Compton component dominating the overall SED, contrary to what shown in the bottom panel of Figure 4.9. We therefore believe that it is highly unlikely that B2 1023+25 can be described with $\theta_v = 20^\circ$ in the high–energy emitting region. We cannot exclude the possibility that the jet bends between the X–ray and the radio emitting regions. In this case, it is possible that the large scale jet (i.e. radio emission) is seen at a larger viewing angle than the compact jet.

Furthermore, consider that the 5 GHz VLBI observations analyzed by Frey et al. (2013) correspond to a rest frame frequency of 31.5 GHz. At this frequency, all the VLBI components but the very inner core are emitting thin synchrotron radiation. Since the brightness temperature of a synchrotron source peaks at the self–absorption frequency, we conclude that all the brightness temperature of the resolved components are lower limits. For the core, Frey et al. (2013) indeed performed a fit with a resolved plus an unresolved component. It is very likely that the resolved core is optically thin (thus giving a lower limit to the brightness temperature), while the unresolved core gives a lower limit because of

the upper limit on the size. As a consequence, the derived Doppler factors are all lower limits, and the derived viewing angles are all upper limits.

4.3.2 Three blazars in the $4 < z < 5$ redshift bin

The two best candidates, after the classification of B2 1023+25, are SDSS J222032.50+002537.5 and SDSS J142048.01+120545.9 ($z = 4.205, R = 4521$ and $z = 4.034, R = 1904$, respectively). We therefore proceeded to observe these sources with *Swift*, to derive their jet orientation and beaming factor. Along with these sources, we included in our observations one extremely radio–loud and radio–luminous quasar not included in the SDSS DR7 Quasar Catalog, but coming from a compilation of $z > 4$ quasars made by Djorgovski[7], i.e. PMN J2134–0419 ($z = 4.346, R = 15843$). Even if not selected from our sample of blazar candidates, PMN J2134–0419 is included in the field of the SDSS+FIRST survey. In fact, this object was photometrically observed in the SDSS, but it was not included in the SDSS DR7 Quasar Catalog because it did not fulfill the requirements of the color–based high–redshift quasar selection. Nevertheless, it is included in the same field as SDSS J222032.50+002537.5 and SDSS J142048.01+120545.9. This is important to correctly estimate the number of misaligned quasars inferred from our observations (see Section 5.2).

During our sample selection, we derived black hole mass estimates for SDSS J222032.50+002537.5 and SDSS J142048.01+120545.9, thanks to dedicated GROND observations (Section 4.1.1). We found black hole masses of $\log(M_{\rm BH}/M_{\odot}) = 9.30$ for both sources. PMN J2134–0419, instead, was not included in that observational campaign, and thus lacks GROND data. Nev-

[7] http://www.astro.caltech.edu/~george/z4.qsos

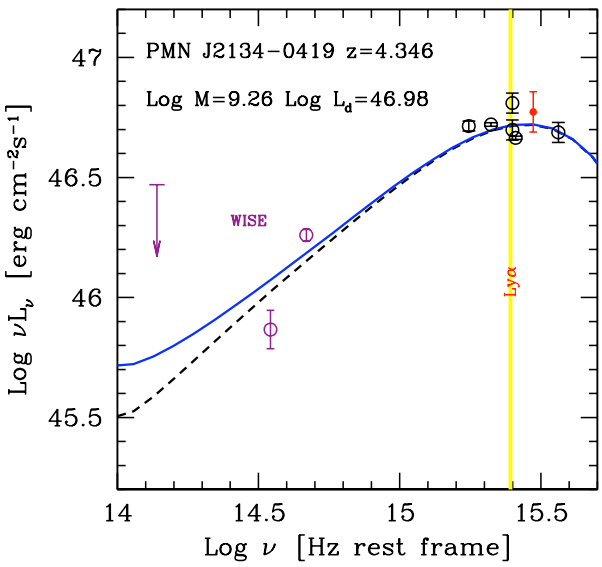

Figure 4.10: Zoom of the SED on the IR–optical–UV wavelength range, to display the accretion disc fitting performed to measure the central black hole mass [$\log(M_{\rm BH}/M_{\odot}) = 9.26$]. The blue solid line shows the best representation of the data, purple data and upper limit are from WISE All–Sky Catalog, black empty data point are archival data, while the red point is the UVOT detection.

ertheless, the peak of the accretion disc emission is visible also in this case (see Figure 4.10), and we can derive a black hole mass estimate for this object following the same method. We obtain a mass of $\log(M_{\rm BH}/M_{\odot}) = 9.26$, confirming that this blazar candidate hosts an extremely massive black hole. The good spectral coverage of the peak of the disk emission limits the uncertainties on the mass value to a factor 2.

The analysis of the data from XRT and UVOT has been done by using HEASoft v 6.16 and the CALDB updated on 2014 September 4 and by following standard procedures as previously described. Because of the low statistics, X–ray data were analysed by using unbinned likelihood. Table 4.10 shows the parameters of our analysis.

Name	Exp [ks]	$N_{\rm H}$ [10^{20}]	$F_{\rm norm}$ [10^{-4}]	$\Gamma_{\rm X}$	$F^{\rm obs}_{0.3-10{\rm keV}}$ [10^{-13}]	Cash/d.o.f.	v [mag]
SDSS J142048.01+120545.9	21.8	1.74	$3.3^{+2.5}_{-1.5}$	1.6 ± 0.3	1.7	64.13/65	20.43 ± 0.10
PMN J2134–0419	25.1	3.34	$2.7^{+2.5}_{-1.3}$	1.6 ± 0.3	1.4	52.36/55	21.11 ± 0.21
SDSS J222032.50+002537.5	30.7	4.41	$1.1^{+1.1}_{-0.6}$	1.4 ± 0.3	1.0	53.30/51	21.16 ± 0.18

Table 4.10: Summary of XRT and UVOT observations of the three candidates. The column "Exp" indicates the effective exposure in ks, while $N_{\rm H}$ is the Galactic absorption column in units of [10^{20} cm^{-2}] from Kalberla et al. (2005). $F_{\rm norm}$ is the normalization flux at 1 keV in units of [10^{-4}ph cm^{-2}s^{-1}keV^{-1}], $\Gamma_{\rm X}$ is the photon index of the power law model [$F(E) \propto E^{-\Gamma}$], $F^{\rm obs}_{0.3-10{\rm keV}}$ is the observed flux in units of [10^{-13} erg cm^{-2} s^{-1}]. The next column indicates the value of the likelihood (Cash 1979) along with the degrees of freedom. The last column reports the observed v magnitude (not corrected for absorption).

Deriving jet features and orientation

With the X–ray data, we complete a good coverage of the SEDs of all our candidates. Figures 4.11 and 4.12 show the SEDs of the 3 blazar candidates. The red points in the X–ray band are the new *Swift*/XRT data. All the other data points are described in the captions. The grey stripes show the sensitivity limit of *Fermi*/LAT. We fitted the observed data with the one–zone leptonic model described in Ghisellini & Tavecchio (2009), as we did for B2 1023+25.

For each of our candidates, we present two models, summarized in Table 4.11. The best representation of the data is shown by the blue lines in Figures 4.11 and 4.12. In all the three cases, this "best fit" describes a source seen under a viewing angle smaller than the jet beaming angle, i.e. $\theta_{\rm v} < 1/\Gamma$. This allows to classify the three candidates as blazars, according to our criterion. The corresponding sets of parameters are consistent with what found for other powerful blazars. The other sets of parameters describe models with the largest possible jet viewing angle consistent with our data. To reproduce the same X–ray and radio fluxes, we have to associate smaller Lorentz factors compared to the "best fit", along with the parameters in the second line of each source of Table 4.11. The models described by these different sets of parameters are represented by green solid lines in Figure 4.11 and 4.12.

Name [1]	$R_{\rm diss}$ [2]	M [3]	$R_{\rm BLR}$ [4]	$P'_{\rm i}$ [5]	$L_{\rm d}$ [6]	B [7]	Γ [8]	$\theta_{\rm v}$ [9]	$\gamma_{\rm b}$ [10]	$\gamma_{\rm max}$ [11]	s_1 [12]	s_2 [13]
1420+1205	360 (600)	2e9	725	6e–3	53 (0.18)	2.6	13	3	100	3e3	1	2.5
	360 (600)	2e9	725	0.2	53 (0.18)	3.4	10	8	10	3e3	–1	2.5
2134–0419	432 (800)	1.8e9	972	7e–3	95 (0.35)	2.9	13	3	70	4e3	0	2.6
	540 (1e3)	1.8e9	972	0.08	95 (0.35)	3.0	10	6	70	4e3	–1	2.6
2220+0025	360 (600)	2e9	671	3e–3	45 (0.15)	2.4	13	3	100	3e3	1	2.2
	540 (900)	2e9	671	0.2	45 (0.15)	2.1	10	8	40	3e3	–1	2.2

Table 4.11: List of parameters used to construct the theoretical SED. Col. [1]: name; Col. [2]: dissipation radius in units of 10^{15} cm and (in parenthesis) in units of Schwarzschild radii; Col. [3]: black hole mass in solar masses; Col. [4]: size of the BLR in units of 10^{15} cm; Col. [5]: power injected in the blob calculated in the comoving frame, in units of 10^{45} erg s^{-1}; Col. [6]: accretion disk luminosity in units of 10^{45} erg s^{-1} and (in parenthesis) in units of $L_{\rm Edd}$; Col. [7]: magnetic field in Gauss; Col. [8]: bulk Lorentz factor at $R_{\rm diss}$; Col. [9]: viewing angle in degrees; Col. [10] and [11]: break and maximum random Lorentz factors of the injected electrons; Col. [12] and [13]: slopes of the injected electron distribution $[Q(\gamma)]$ below and above $\gamma_{\rm b}$; The total X–ray corona luminosity is assumed to be in the range 10–30 per cent of $L_{\rm d}$. Its spectral shape is assumed to be always $\propto \nu^{-1}\exp(-h\nu/150$ keV).

We perform the same consistency check introduced in Section 4.3.1: for each source we test how an object with this last set of parameters would look like if seen at $\theta_{\rm v} < 1/\Gamma$, i.e. under a typical viewing angle for blazars $\theta_{\rm v} = 3°$. These "re–oriented" models are shown in the figures with the dashed green lines.

In the cases of SDSS J142048.01+120545.9 and SDSS J222032.50+002537.5 (Figure 4.11), the resulting SEDs are extremely luminous in the X–rays. Although similar luminosities have already been observed in some known high–redshift blazars, such as GB 1428+4217 ($z = 4.72$; Worsley et al. 2004) and RX J1028–0844 (Zickgraf et al. 1997; Yuan et al. 2000), there are some problems with the radio luminosity. If we extrapolate from the existing radio data of the two sources a slope of $F_\nu \propto \nu^0$ (i.e. the expected flat spectrum for a blazar), the "re–oriented model" would exceed that limit. Moreover, the "re–oriented" version of SDSS J222032.50+002537.5 would also be detected by *Fermi*/LAT in the γ–rays, while so far no such object has been detected by LAT (*Fermi*/LAT sensitivity is shown in Fig. 4.11 and 4.12 with the grey shaded area). These problems lead us to discard this solution, pre-

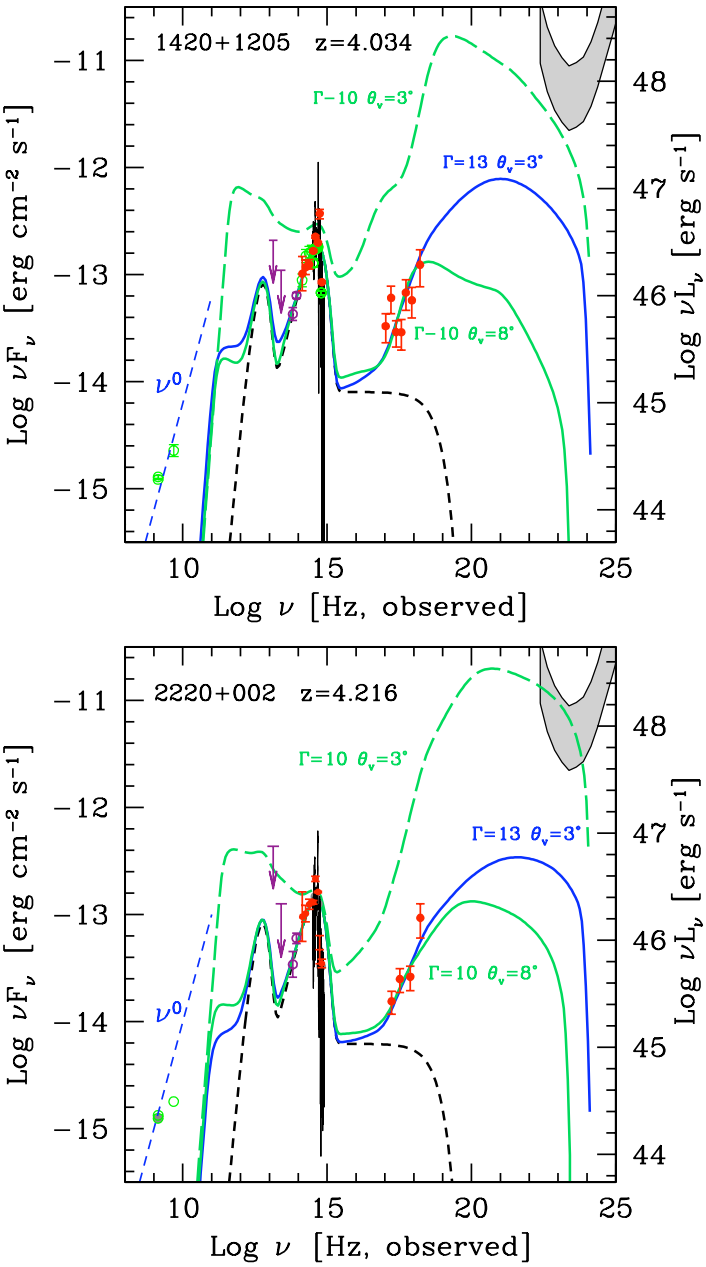

Figure 4.11: SEDs of SDSS J142048.01+120545.9 (*top panel*) and SDSS J222032.50+002537.5 (*bottom panel*). In each figure, the blue solid line shows the best representation of the data. The green solid line is the fit made with largest possible viewing angle (second line of each source in Table 4.11), while the green dashed line is the model with the same parameters, but "re–oriented" with a viewing angle $\theta_v = 3°$. The black dashed line is the thermal emission from accretion disc, torus and corona. The blue dashed line is the extrapolated $F(\nu) \propto \nu^0$ from the observed radio data at lowest frequencies. Red data point are the new *Swift*/XRT and UVOT observations, purple and/or green data points are archival data.

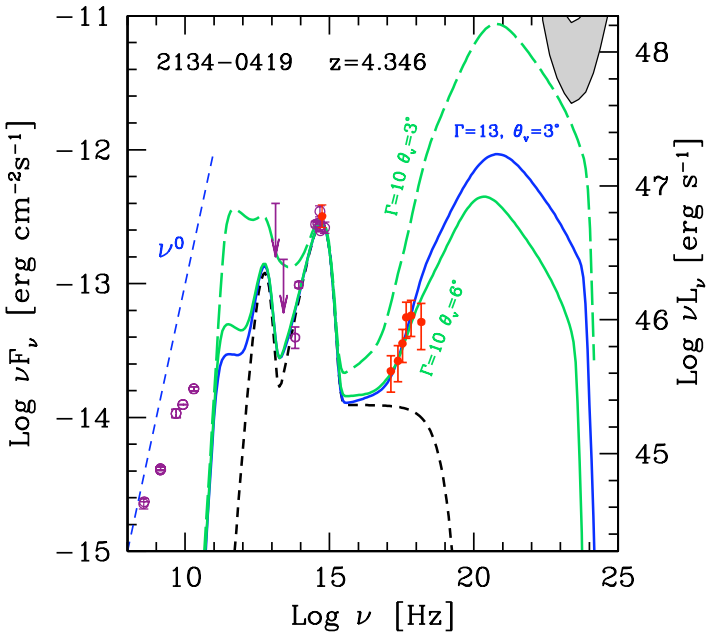

Figure 4.12: Full SED of PMN J2134–0419, with lines and data as in Figure 4.11.

ferring the one with a small viewing angle and a large Γ. Therefore SDSS J142048.01+120545.9 and SDSS J222032.50+002537.5 can be classified as blazars, both with $\Gamma = 13$ and $\theta_v = 3°$.

In the case of PMN J2134–0419, the largest angle solution gives $\theta_v = 6°$. In this case the re–oriented model is not far from the SED at $\theta_v = 6°$, since the viewing angles are closer. The re–oriented model is also not completely unreasonable. For this object, therefore, we can state that the viewing angle is in the range $3° - 6°$, with corresponding Lorentz factors of $13 - 10$.

Comparison with known blazars

To put these three objects in the wider picture of known high–redshift blazars, we compare them with the most studied objects. Fig. 4.13 shows our three blazar candidates compared with the three blazars known at $z > 5$ (Q0906+6930, B2 1023+25, SDSS J1146+403) and the two best studied

blazars at $4 < z < 5$ (GB 1428+4217 and RX J1028–0844). It can be immediately noticed that GB 1428+4217 and RX J1028–0844 are much more luminous in the X–rays than the other blazars considered. This is likely connected to the fact that they were discovered by associating known radio–loud objects to X–ray counterparts from the *ROSAT*[8] all–sky survey (Voges et al. 1999), being among the first high–z blazars ever discovered, and therefore the most luminous sources of their kind. Our systematic approach, instead, chases less extreme blazars, since we start our selection from their optical features, that trace the disc accretion and not the jet, and we selected them from a complete optical quasar catalog.

To understand how our fits are sensitive to the viewing angle, Figure 4.13 also shows how a SED with fixed parameters can vary with small variations in the viewing angle. The difference between the extreme blazars GB 1428+4217 and RX J1028–0844 and our three blazar candidates (along with the three $z > 5$ confirmed blazars) could be just due to a difference in orientation of 4°. Strong beaming is responsible for such extreme variations. The beaming pattern produced by a relativistically moving source that emits for external Compton (as expected in FSRQs as our high–z blazars) is in fact strongly dependent on the viewing angle, through the beaming factor δ. Dermer (1995) calculated that the observed flux of such a relativistic emitting region has a strong dependence on the beaming factor:

$$F_{\rm EC} \propto \delta^{4+2\alpha} \tag{4.9}$$

where α is the energy spectral index of the emitted radiation. This dependence

[8] X–ray telescope that operated between 1990 and 1999.

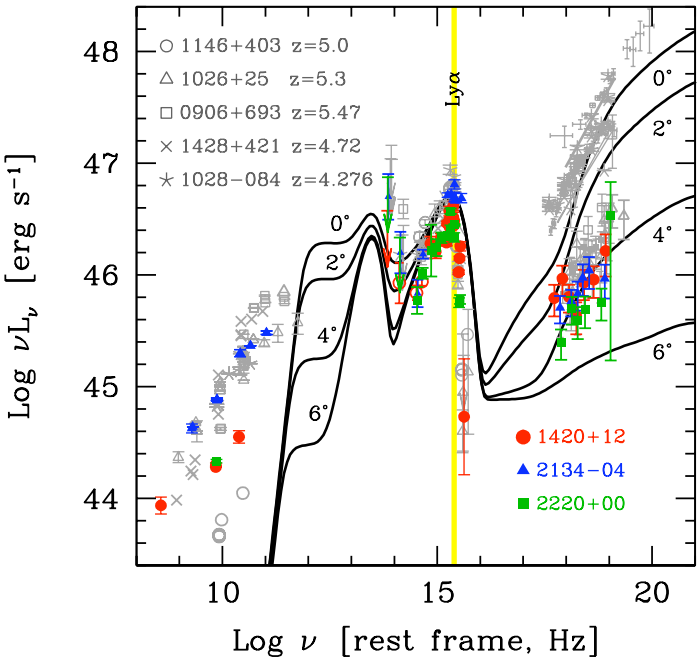

Figure 4.13: Comparison of SDSS J142048.01+120545.9, SDSS J222032.50+002537.5 and PMN J2134–0419 (red filled circles, green filled squares and blue filled triangles, respectively) with the three $z > 5$ and the two most known $z > 4$ blazars (data as labelled). GB 1428+4217 and RX J1028–0844 have X–ray spectra much more luminous than the other objects, as expected in case of objects found serendipitously. Superposed to the data (solid black lines), SEDs of a typical powerful blazar oriented at different viewing angles (as labelled). Note how the observed flux from the external Compton emission is strongly dependent on the viewing angle (Dermer 1995), more than the corresponding synchrotron radiation. This shows why the X–ray data help in finding the correct viewing angle.

is stronger than the one characterizing synchrotron emission, which is

$$F_{\rm synchro} \propto \delta^{3+\alpha}. \tag{4.10}$$

This determines the variations of radio emission as a function of viewing angle[9]. It is worth noticing that this is the reason why observations of high–energy humps are necessary to classify a source as a blazar, while the radio luminosity alone is not enough. The high–energy emission is in fact more sensitive to viewing angle variations than the synchrotron one.

The reason of the different dependence is due to the assumption that the high energy hump is produced by external Compton scattering (Dermer 1995). In this case, the comoving observer sees all photons coming from the forward emiphere, and in particular from a small portion of the sky, of angular size $1/\Gamma$. The inverse Compton luminosity produced by the relativistic electrons distributed isotropically in the comoving frame is greater in the forward direction, because head on collisions are favored with respect to tail on scatterings. Therefore, in the comoving frame, the Compton emission is anisotropic. When observed in the rest frame, this implies a different pattern than the usual $\delta^{3+\alpha}$.

[9] In our one zone model the radio emission is self–absorbed, but the expected change of the flux as we change $\theta_{\rm v}$ can be seen through the far IR synchrotron emission that shows a smaller range of variation than the hard X–rays.

5

SMBHs in the early Universe

Thanks to our systematic approach to look for blazars at very high redshift, we classified 4 extremely radio–loud high–redshift quasars located in the area of the sky covered by both SDSS and FIRST surveys. As a result of this same approach, we classified also the third most distant blazar candidate SDSS J1146+403 ($z = 5$; Ghisellini et al. 2014b). This approach is not merely a compilation of high–redshift rare objects, but can be useful to understand supermassive black hole features and formation in the early stages of the Universe, being blazars good tracers of their parent population (Section 5.1).

The picture is still uncertain, and therefore needs strong observational clues, that our approach can provide. Nevertheless, this is the first time that extremely massive jetted sources are systematically explored at such high redshift. This allows us to have an unprecedented view on early SMBH formation (Section 5.2), but opens some interesting issues, related to role and specific features of the relativistic jet (Sections 5.1.1 and 5.2.1).

5.1 Blazars as tracers of all jetted AGN

As explained in Chapter 4, the peculiar orientation of blazars makes them very efficient tracers for their whole parent population, i.e. those jetted AGN with same features (same mass, same accretion rate,...) but with their jets oriented randomly in the sky. Specifically, for each observed blazar, we can infer the presence of $2\Gamma^2$ analogous jetted objects with jets in other directions. Since the typical Lorentz factor in blazars is $\sim 10 - 15$, one can trace the presence of hundreds of jetted AGN with a few classifications.

Anyway, this is true for all blazars, not only the results of our research. What are the **main advantages of our systematic approach**, compared to the already known high–redshift blazars? Firstly, we selected them systematically, i.e. we compiled a complete sample of candidates from a flux limited quasar survey, instead of detecting them in a serendipitous way. This gives a strong statistical meaning to the results we are obtaining. At the end of the classification procedure, we will be able to reliably estimate *how many blazars are included in a complete survey of quasars*.

The second important advantage of our approach resides in the fact that we selected our blazar candidates from a complete quasar survey, that is also limited to a specific area of the sky (i.e. the solid angle $\Omega_{\mathrm{SDSS+FIRST}}$). It is therefore reasonable to assume that the amount of blazars we find in that specific sky region is a fraction $\Omega_{\mathrm{SDSS+FIRST}}/4\pi$ of the total number of blazars with those features distributed in the whole sky. Knowing the size of the selection area of the blazar candidates allows our results to be more statistically relevant. In other words, the classification of 5 objects is more statistically important than the 7 blazars already known before the beginning of this project: the

observation of one of them traces the presence of $N_{\rm parent}$ jetted AGN, where

$$N_{\rm parent} \simeq 2\Gamma^2 \frac{4\pi}{\Omega_{\rm SDSS+FIRST}} = 2\Gamma^2 \frac{40000\,{\rm deg}^2}{8770\,{\rm deg}^2}. \quad (5.1)$$

We can therefore calculate how many jetted AGN with same black hole mass and accretion rate can be inferred thanks to our results. We are interested in dividing our results in two main redshift bins: $4 < z < 5$ and $5 < z < 6$.

$4 < z < 5$: in this redshift bin, only 7 sources were known before the beginning of our project. Of those, 2 are included in the SDSS DR7 Quasar Catalog from which we selected our candidates (SDSS J083946.22+511202.8 and SDSS J151002.92+570243.3; see Sbarrato et al. 2013a), and are therefore located in the same area of sky as the blazars we classified ($\Omega_{\rm SDSS+FIRST}$). Adding the three sources that we classified in Section 4.3.2 (SDSS J142048.01+120545.9, SDSS J222032.50+002537.5 and PMN J2134–0419; Sbarrato et al. 2014a), there are 5 blazars with a black hole mass $M_{\rm BH} > 10^9 M_\odot$. They allow us to infer the existence of a large number of jetted quasars analogous to them. They are all observed with $\theta_{\rm v} < 1/\Gamma$, with the typical bulk Lorentz factor $\Gamma = 13$. Therefore, each of them traces the presence of $\sim 2\Gamma^2 = 338(\Gamma/13)^2$ quasars with $M_{\rm BH} > 10^9 M_\odot$ in the area covered by the SDSS+FIRST survey (Ghisellini et al. 2010a, Volonteri et al. 2011, Ghisellini et al. 2013). Thanks to our approach, we can therefore infer the presence of

$$N_{\rm parent} = 5 \times \left(2\Gamma^2 \frac{4\pi}{\Omega_{\rm SDSS+FIRST}}\right) \simeq 7700 \left(\frac{\Gamma}{13}\right)^2 \left(\frac{\Omega_{\rm SDSS+FIRST}}{8770}\right)^{-1} \quad (5.2)$$

jetted AGN with similar intrinsic properties to the blazars we classified in

the whole sky, in the $4 < z < 5$ redshift bin. The comoving volume in this redshift frame is $\sim 425\mathrm{Gpc}^3$, and therefore we can conclude that there must be ~ 18 supermassive black holes per Gpc^3 that have $M_{\rm BH} > 10^9 M_\odot$ and are hosted in jetted systems, between $z = 4$ and $z = 5$.

$5 < z < 6$: only one source was known in this redshift bin before the beginning of our work (Q0906+6930; Romani et al. 2004). This source is not included in the area of sky covered by the SDSS+FIRST survey. In the frame of our systematic selection, we were able to classify two blazars at $z > 5$: B2 1023+25 (as described in Section 4.3.1; Sbarrato et al. 2012b; 2013b) and SDSS J1146+403 (Ghisellini et al. 2014b). If $\theta_{\rm v} < 1/\Gamma$ as in our best–fit models, the number of sources similar to B2 1023+25 and SDSS J1146+403 but with their jets oriented outside of our line of sight is $2 \times 2\Gamma^2 = 676(\Gamma/13)^2$ in the portion of the sky covered by SDSS+FIRST. As for the objects in the $4 < z < 5$ redshift bin, we can infer the existence of

$$N_{\rm parent} = 2 \times \left(2\Gamma^2 \frac{4\pi}{\Omega_{\rm SDSS+FIRST}}\right) \simeq 3100 \left(\frac{\Gamma}{13}\right)^2 \left(\frac{\Omega_{\rm SDSS+FIRST}}{8770}\right)^{-1} \tag{5.3}$$

jetted quasars with $M_{\rm BH} > 10^9 M_\odot$ at $z > 5$ in the whole sky. The co–moving volume in the redshift frame $5 < z < 6$ is ~ 380 Gpc^3, hence we can conclude that there must be at least 8 radio–loud AGN per Gpc^3 hosting supermassive black holes with $M_{\rm BH} > 10^9 M_\odot$ in this redshift bin.

We can use these results to study the distribution of early extremely massive black holes, providing constraints for models of supermassive black hole formation and evolution.

5.1.1 A lack of misaligned jetted AGN?

The power that blazars have in tracing a large number of misaligned jetted sources is now clear, but it introduces some issues. The main problem is connected to the expected number of jetted AGN.

We can compare our results with the original quasar sample in which we selected our candidates. From the quasar sample analyzed by Shen et al. (2011), we classified two $z > 5$ and two of the $4 < z < 5$ blazars (SDSS J142048.01+120545.9 and SDSS J222032.50+002537.5). Their classification traces the presence of $4 \times 2\Gamma^2 \simeq 1300$ jetted AGN randomly oriented, that we should find in the SDSS+FIRST. These sources in fact have same black hole and accretion features as the blazars. We expect them to be powerful, highly accreting and highly massive, being therefore included in the SDSS DR7 Quasar Catalog (on which Shen et al. 2011 base their sample). The radio luminosity is emitted from the jet, and is therefore beamed. In the misaligned objects the radio luminosity will be less than in blazars (see Section 3.4), but the corresponding flux should still be brighter than the flux limit in FIRST (1 mJy). Most of the $\sim$ 1300 misaligned radio–loud quasars whose presence is inferred thanks to our blazar classification should be still be present in the sample studied by Shen et al. (2011), as radio–detected $z > 4$ quasars.

Table 4.1 summarizes the numerical composition of the SDSS DR7 Quasar Catalog. There is clearly a large discrepancy with what we expected: Shen et al. (2011) only found 53 $z > 4$ radio–detected quasars in their sample. We predict a factor $\sim$ 24 more objects than what is observed.

This discrepancy was already observed in Ghisellini et al. (2010a), where the authors compared the distribution of jetted AGN inferred from *Swift*/BAT blazars with the detections in the SDSS+FIRST survey. At $z < 3$ there was still agreement, but at higher redshift they found a deficit of at least a factor 10.

Volonteri et al. (2011) discussed this issue and suggested a few possible causes for this relevant discrepancy:

- powerful misaligned radio sources at high redshift do not enter a spectroscopic optical survey like SDSS, because of heavy obscuration of the nucleus in that wavelength range. Therefore, they fall below the detection threshold;
- the radio emission becomes weaker than expected at high redshift, falling below the FIRST detection limit;
- the average Lorentz factor is systematically smaller at high redshift, so that the factor $2\Gamma^2$ that allows us to estimate the parent population is significantly smaller;
- the identification of extended radio sources with their optical counterpart is missing, for some unknown reason.

The possibility of a weaker radio emission was investigated by Ghisellini et al. (2014a). The advanced hypothesis is connected to the possible interaction between the cosmic microwave background (CMB) and the electrons normally emitting synchrotron in blazar jets. At high redshift, the CMB energy density can exceed the magnetic one in the jet structures. In this case, electrons would cool preferentially by scattering over CMB photons. The jet emission would loose radio luminosity and gain X–ray emission. This process is more efficient in regions of the jet where the magnetic energy density is lower. In other words, this process should be more evident in those objects whose radio emission is lobe–dominated, i.e. misaligned jetted quasars instead of blazars. This could be a reasonable process to explain such a huge lack of radio–detected quasars in the SDSS+FIRST survey.

5.2 Two formation epochs for SMBHs?

Regardless the process or feature that originate the lack of misaligned quasars, blazars are certainly the more reliable tracers of extremely massive black holes hosted in jetted systems at high redshift. But *how do the blazars we classified fit in the current paradigm of supermassive black holes in the early Universe?* The main contribution derives from populating the $z > 4$ redshift bin of supermassive black holes hosted in jetted systems. This is particularly useful to understand the distribution of these objects at a time when the Universe had only a billion years of age.

Fig. 5.1 shows the comoving number density of extremely massive black holes (i.e. with $M_{\rm BH} > 10^9 M_{\odot}$) hosted by radio–quiet (blue line, derived as in Ghisellini et al. 2010a from the mass function in Hopkins et al. 2007) and radio–loud AGN. The density function of radio–quiet quasars is derived as in Ghisellini et al. (2010a) from the mass function in Hopkins et al. (2007). On the other hand, the comoving number density of radio–loud quasars is derived from *Fermi*/LAT (Ajello et al. 2012) and *Swift*/BAT (Ajello et al. 2009) blazar luminosity functions, assuming that every blazar traces the existence of $2\Gamma^2$ jetted quasars (Ghisellini et al. 2010a). The blazar survey of *Swift*/BAT is limited at $z < 4$, and *Fermi*/LAT finds blazar up to even lower redshift, therefore at $z > 4$ there is not a complete survey of blazars that provides a reliable number density. For $z > 4$ the density was assumed to decrease exponentially, as the corresponding one for radio–quiet objects.

Nevertheless, a hint of different density distributions between jetted and non–jetted objects was already visible in Ghisellini et al. (2010a) and Ghisellini et al. (2013). While radio–quiet objects seem to be more numerous at redshift $z \sim 2 - 2.5$, the distribution of jetted quasars suggests that they do not show such a peak, but more likely a plateau that extends at least up to

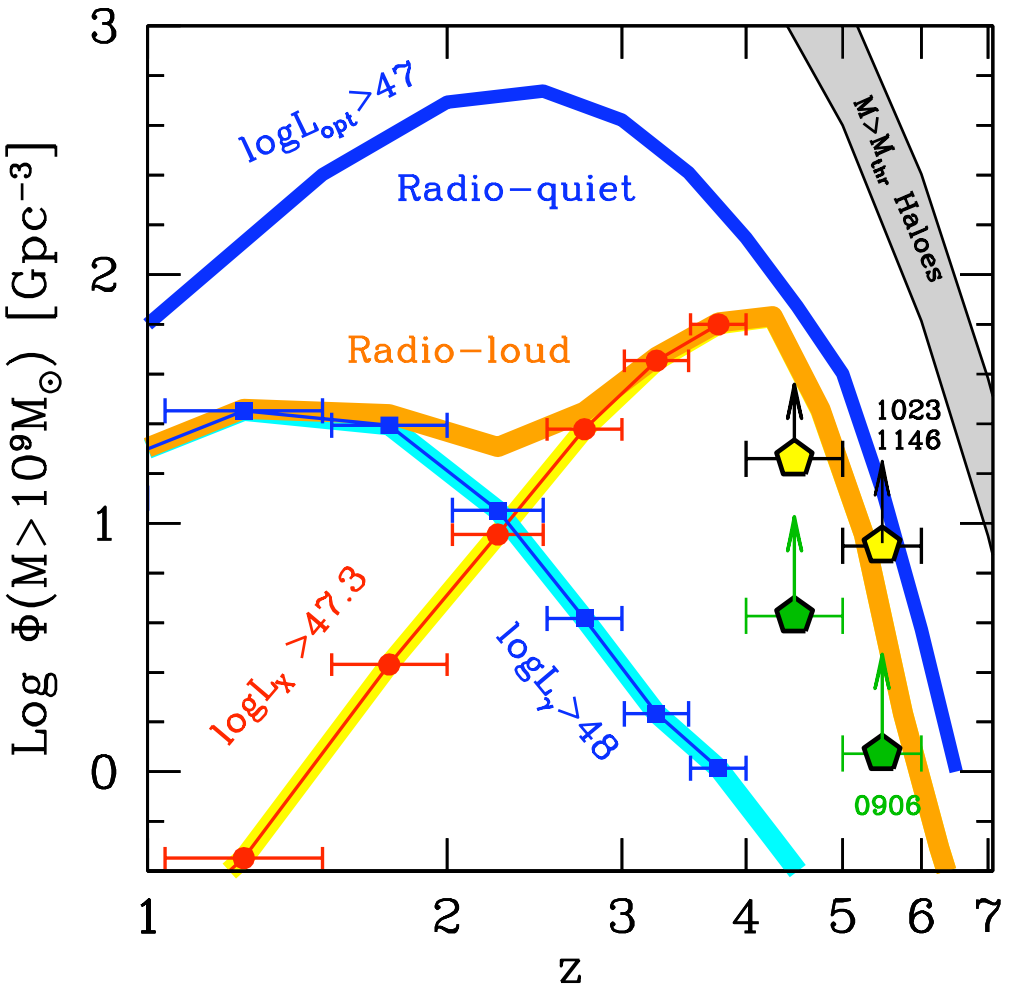

Figure 5.1: Comoving number density of supermassive black holes with $M_{\rm BH} > 10^9 M_\odot$ hosted in radio–quiet (blue line, derived from the luminosity function by Hopkins et al. 2007) and radio–loud quasars (orange line). The radio–loud density is obtained from blazar number densities, by multiplying them by $450 = 2\Gamma^2$ ($\Gamma = 15$). Blue data and the light blue line are derived from the γ–ray luminosity function obtained by *Fermi*/LAT (Ajello et al. 2012). Red data points and the yellow line are derived from the [15–55keV] luminosity function from Ajello et al. (2009), modified as in Ghisellini et al. (2010a). All the number density functions are derived by integrating the corresponding luminosity functions at luminosities larger than what labelled in Figure, to ensure that correspond to $M_{\rm BH} > 10^9 M_\odot$. Green pentagons represent the state of the art before the beginning of our project, with 4 serendipitous blazars in the $4 < z < 5$ bin and the single detection of Q0906+6930 at $z > 5$. The yellow pentagons are instead the number densities derived from our results. In the redshift frame $5 < z < 6$ the data point is given by the two blazars we classified at $z > 5$ (B2 1023+25 and SDSS J1146+403). At $4 < z < 5$ the new (yellow) lower limit is provided by the two already known high–z blazars in the SDSS+FIRST survey (SDSS J083946.22+511202.8 and SDSS J151002.92+570243.3), along with the three blazars classified in Section 4.3.2 (SDSS J142048.01+120545.9, SDSS J222032.50+002537.5 and PMN J2134–0419). Our results confirm the existence of an early peak ($z \sim 4$) of black hole formation in jetted AGN, in contrast to the main formation epoch of massive radio–quiet quasars ($z \sim 2.5$). The yellow pentagons still correspond to lower limits because of other possible blazar candidates that could be confirmed blazars in the near future.

$z \sim 4$, or maybe a different peak at $z \sim 4$. Those papers did not reach a firm conclusion about the real distribution of jetted AGN at $z > 4$, lacking a significant number of objects in that redshift frame. In other words, they could not disentangle between a plateau and a high–redshift peak.

The number densities derived in Section 5.1 from the classifications of the candidates in our sample are instead very significant. Our observations in fact clearly push towards an interesting conclusion: *the density of extremely massive black holes hosted in jetted systems peaks at least around* $z \sim 4$, while the non–jetted systems peak at $z \sim 2 - 2.5$. In other words, the number of heavy black holes hosted in jetted systems increases with cosmic time, and peaks at $z > 4$. This suggests **two different epochs of SMBH formation**. The most striking feature of this result is that *black holes that grow while developing a jet seem to be born earlier, or to grow faster*, than black holes with same masses that do not show jets.

5.2.1 Jets and fast accretion

The presence of a jet in AGN is commonly linked to high values of black hole spin. The black hole rotational energy, in fact, is a possible source of power to launch the jet (Blandford & Znajek 1977; Tchekhovskoy, Narayan & McKinney 2011), while the angular momentum of the black hole itself easily identifies its launching direction.

This does not facilitate a fast accretion, according to common knowledge. Rapidly spinning black holes, in fact, are generally associated to high accretion efficiencies, since the innermost stable orbit of the accretion disc approaches the gravitational radius. Thorne (1974) showed that the maximum spin that a black hole can reach through accretion is $a = 0.998$ (instead of $a = 1$), since the hole slows down by capturing accretion disc radiation, that exert a coun-

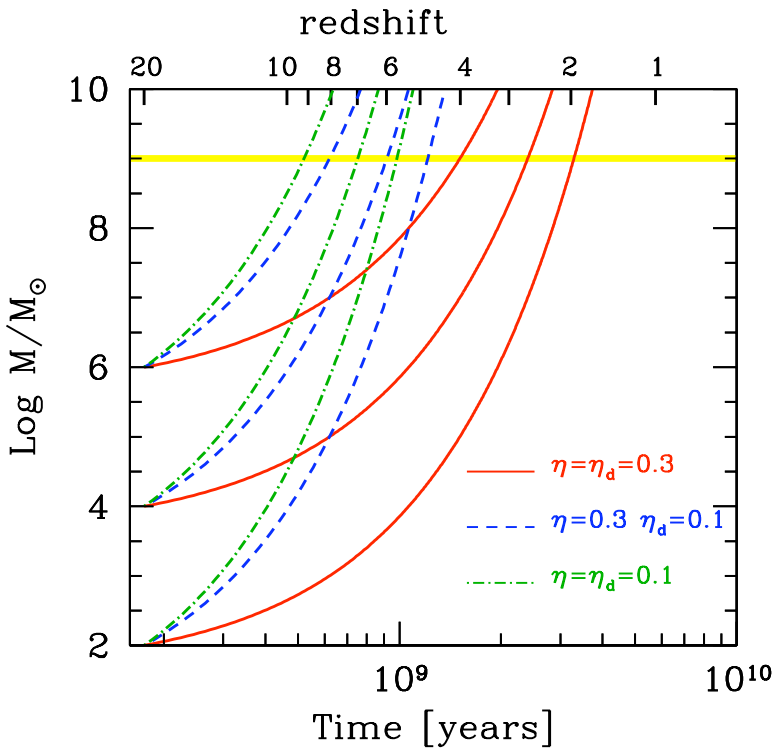

Figure 5.2: The mass of a black hole accreting at the Eddington rate as a function of time (bottom axis) and redshift (top axis), calculated by Ghisellini et al. (2013). The black hole is assumed to double its mass in a Salpeter time (Salpeter 1964). Accretion starts at $z = 20$ from a black hole seed of 10^2, 10^4, or $10^6 M_\odot$, with different efficiencies, as labelled. The horizontal yellow line marks $10^9 M_\odot$, that is the reference mass that we observe in high–z blazars. At larger $\eta_{\rm d}$ corresponds a smaller amount of accretion needed to produce a fixed $L_{\rm d}$, and therefore to a longer black hole growing time. If part of the accretion energy goes into powering a jet (maybe through magnetic field), the growth time decreases, and it is easier to grow a $10^9 M_\odot$ black hole in less time.

teracting torque. The accretion efficiency that corresponds to this spin value is $\eta = 0.3$, larger than the efficiency in the case of a non–rotating black hole ($\eta = 0.08$). A larger efficiency corresponds to a lower overall accretion rate (since $\dot{M} = L_{\rm d}/\eta c^2$). For a fixed luminosity, then, *a black hole accretes less matter and grows slower*. As explained in Ghisellini et al. (2013), a spinning black hole accreting at Eddington rate (i.e. at the highest rate allowed for a standard disc), if we assume that it doubles its mass on a Salpeter (1964) time, would need 3.1 Gyr to grow from a seed of $100 M_\odot$ to $10^9 M_\odot$[1]. Hence, such massive black holes would not be visible at $z > 2.1$ (as shown in Figure 5.2, from Ghisellini et al. 2013), while we see from Figure 5.1 that their preferential formation epoch seems to be around $z \sim 4$.

In Ghisellini et al. (2013) some options for a faster accretion in presence of a jet are explored. The available energy, in fact, is not all radiated away, but it may contribute in amplifying the magnetic field and thus launching the jet. We can define two different contributions to the global efficiency η: one related to the disc luminosity (i.e. the radiative efficiency $\eta_{\rm d}$), and one implied in generating the magnetic field that helps in launching the jet $\eta_{\rm j}$:

$$\eta = \eta_{\rm d} + \eta_{\rm j} \tag{5.4}$$

In this case, to produce a fixed luminosity, we need a larger accretion rate, since part of the gravitational energy is spent for some non radiative processes necessary to form the jet. In other words, a spinning black hole can accrete faster if some of its accretion efficiency is spent for the jet ($\eta_{\rm j} > 0$ and $\eta = 0.3$). Considering this, the accretion is faster, but black holes with $M_{\rm BH} > 10^9 M_\odot$ are

[1] If we ignore black hole mergers, that instead appear necessary in all the simulations. Merging processes would even slow down the accretion process, preventing a coherent accretion over the whole period.

still hard to form before $z \sim 4-5$.

The blazars we found at $z \gtrsim 5$ ($\sim$ 1Gyr) all have $M_{\rm BH} > 10^9 M_\odot$. If this black hole is maximally spinning ($\eta = 0.3$), its mere presence requires $\eta_{\rm j} \gtrsim 0.2$ and $\eta_{\rm d} \lesssim 0.1$, as can be seen in Figure 5.2, if we assume a black hole seed of $100 M_\odot$. Assuming a more massive seed helps, but we are still forced to consider a maximally spinning black hole that does not convert its entire gravitational energy into radiation, but also in generating a magnetic field to launch the jet. This is reasonable and (probably) necessary for high–redshift objects, but is not required to justify the presence of heavy black holes in jetted systems at low redshift. At $z \sim 2$, in fact, more time is available to form such massive black holes. Note also that a fast accretion requires a large amount of cold gas in the surroundings of the black hole, to continuously fuel the accretion. This is a reasonable picture at high redshift, but the black hole environment at lower redshift is generally poorer. This means that other, *less extreme and more plausible* processes can drive supermassive black hole formation and growth. This is the reason why the presence of such massive objects is not a major problem, while their presence at $z > 4$ is harder to be justified.

At this stage, the toy model we just introduced is only a plausible idea to justify such a relevant population of heavy black holes in jetted systems, and therefore the presence of these sources at high redshift still remains an interesting open issue.

6 Conclusions

In this thesis, we explored the relation between jets and accretion structures in AGN, with a specific focus on the high–redshift Universe ($z > 4$). These AGN components, in fact, are the key ingredients to study when and how the most massive black holes formed and grew.

As an insight on the relation between accretion structures and relativistic jets (Chapter 3), we studied a sample of γ–ray detected blazars with broad emission lines and broad–lineless radio–galaxies, all with known redshift, a measure of broad emission lines (or upper limit) and mass measure. To explore both the radiatively efficient (high accretion rate) and inefficient (low accretion rate) accretion regimes, both classes are needed.

Comparing blazars and radio–galaxies, we found that the transition between efficient and inefficient accretion regimes occurs at the critical value $\dot{m}_c \sim 0.1$, i.e. $L_{\rm BLR}/L_{\rm Edd} \sim 5 \times 10^{-4} - 10^{-3}$ with a radiative efficiency $\eta = 0.1$ (Section 3.4). At accretion rates lower than that, the ionizing luminosity from the accretion structure decreases with a slope steeper than $\propto \dot{m}^2$: this is consistent with a **transition from a standard radiatively efficient accretion disc to an inefficient accretion flow** (such as the ADAF model).

A different accretion regime is a good basis to introduce a more physical

subclassification of blazars. They are canonically divided in FSRQs and BL Lacs according to the equivalent width of their broad emission lines, but this does not reflect an intrinsic difference (Section 3.2). A classification based on $L_{\rm BLR}/L_{\rm Edd}$ can instead be connected with intrinsically different accretion features, and is therefore more justified.

While comparing two classes of objects with different viewing angles, their difference affects only the tracer of the jet power, but not the accretion tracer: the first is beamed along the emitting direction, while the second is likely isotropically emitted. We realized that radio and broad line region luminosities can be used in combination to estimate the viewing angle of a specific source (Section 3.4.1). We plan to further investigate on this topic, as a basis to *define a new, reliable tracer of jetted AGN orientation*.

The core project that was developed in this thesis focuses on the search and study of blazars at very high redshift, as tracers of the most massive black holes hosted in jetted systems that form in the early stages of the Universe.

- ✓ We collected a sample of good blazar candidates, by selecting $z > 4$, extremely radio–loud ($R > 100$) broad–line AGN from an optical spectroscopic quasar sample (Section 4.1). We measured their black hole masses and accretion rates by fitting their optical–IR spectra with a standard accretion disc model (Section 4.2). **The accretion disc fitting is a reliable mass measurement method**, from which precise black hole mass estimates can be obtained with only photometric data.

- ✓ The objects we selected have $M_{\rm BH} > 10^9 M_\odot$, and are accreting at high rate ($L_{\rm d} \sim 10\% L_{\rm Edd}$). Therefore, our selection criteria efficiently identify high–redshift, extremely massive, highly accreting jetted quasars.

- ✓ The characterization of our candidates successfully began, with the

classification of the highest redshift object (B2 1023+25, with $z = 5.3$; Section 4.3.1) and three sources at $4 < z < 5$ (SDSS J142048.01+120545.9, SDSS J222032.50+002537.5 and PMN J2134–0419; Section 4.3.2). We managed to classify these objects thanks to ad hoc X–ray observations. The successful classification of these sources confirm that **our selection criteria efficiently select very good blazar candidates**.

✓ These classifications, along with the other two $4 < z < 5$ blazars known in the same area of sky occupied by our sample and another $z > 5$ blazar found by our group (SDSS J1146+403; Ghisellini et al. 2014b), **efficiently trace their parent population** (Section 5.1). Specifically, from the 5 blazars known at $4 < z < 5$ in the SDSS+FIRST field we infer the presence of $\sim 7700(\Gamma/13)^2$ jetted AGN with similar intrinsic properties. This means that there must be ~ 18 jetted quasars per Gpc^3 with $M_{\rm BH} > 10^9 M_\odot$ at $4 < z < 5$. From the two blazars classified at $z > 5$ in SDSS+FIRST, we can infer the presence of $\sim 3100(\Gamma/13)^2$ jetted AGN in the same redshift bin, that means ~ 8 quasars per Gpc^3 with $M_{\rm BH} > 10^9 M_\odot$, hosted in jetted systems at $z > 5$.

These results raise some interesting points on the physics of early supermassive black holes and their relation with relativistic jets, and *open fundamental issues* on their features:

- The comoving number density of extremely massive black holes hosted in jetted systems can be compared with the analogous density of non–jetted AGN. While the latter preferentially form at $z \sim 2-2.5$, our results indicate that **highly massive jetted systems preferentially form at** $z \sim 4$ (Section 5.2). In other words, the ratio between the number of radio–

loud and radio–quiet AGN changes with time, for a still unknown reason.

- At high redshift, very massive black holes can form on a short timescale, most likely producing a jet. If the jet presence is associated with a high accretion efficiency (Section 5.2.1) the black hole should grow slowly. In these conditions, **how such massive black holes can form so fast?** Accreting at Eddington rate with a large efficiency is not fast enough to justify the presence of such massive jetted sources at $z > 4$. On the other hand, if the gravitational energy is distributed in accretion, radiation and another component, possibly related to the jet formation, instead that being only accreted and radiated away, the accretion process could be faster. Solutions different from standard accretion could ease the picture, such as a super–Eddington accretion through a slim disc (Madau et al. 2014). In this case, the black hole should accrete up to a billion solar masses from a stellar–sized seed in a few hundreds Myrs.
  These tentative hypotheses show that early black hole formation is not properly understood yet. An even greater challenge would be to find such massive black holes in jetted quasars at $z > 6$, so this is the natural development for future work.

- Comparing our results with the number of jetted objects actually observed, we find a huge discrepancy: in the sample from which we selected our candidates, randomly oriented jetted objects are a factor $\sim 20 - 24$ less than what we predict from our classification (Section 5.1.1). This is still an open issue, but a few hypotheses can be formulated, such as a heavy obscuration of the nucleus, or an anomalously weakness of the radio jets, maybe due to scattering of photons on the CMB, resulting in a large X–ray luminosity and a faint radio emission.

A

BL Lacs from Shaw et al. (2013)

We show in Figures A.1, A.2, A.3, A.4 and A.5 the SEDs of the 26 objects from Shaw et al. (2013), divided according to the reclassification, discussed in Section 3.2. The SEDs are fitted with a one–zone leptonic model, fully described in Ghisellini & Tavecchio (2009). In each SED, the blue solid line represents the overall model. The green solid line is the synchrotron component, the black dashed line is the thermal emission from accretion disc, torus and corona, while the grey long–dashed line is the Synchrotron–Self–Compton emission.

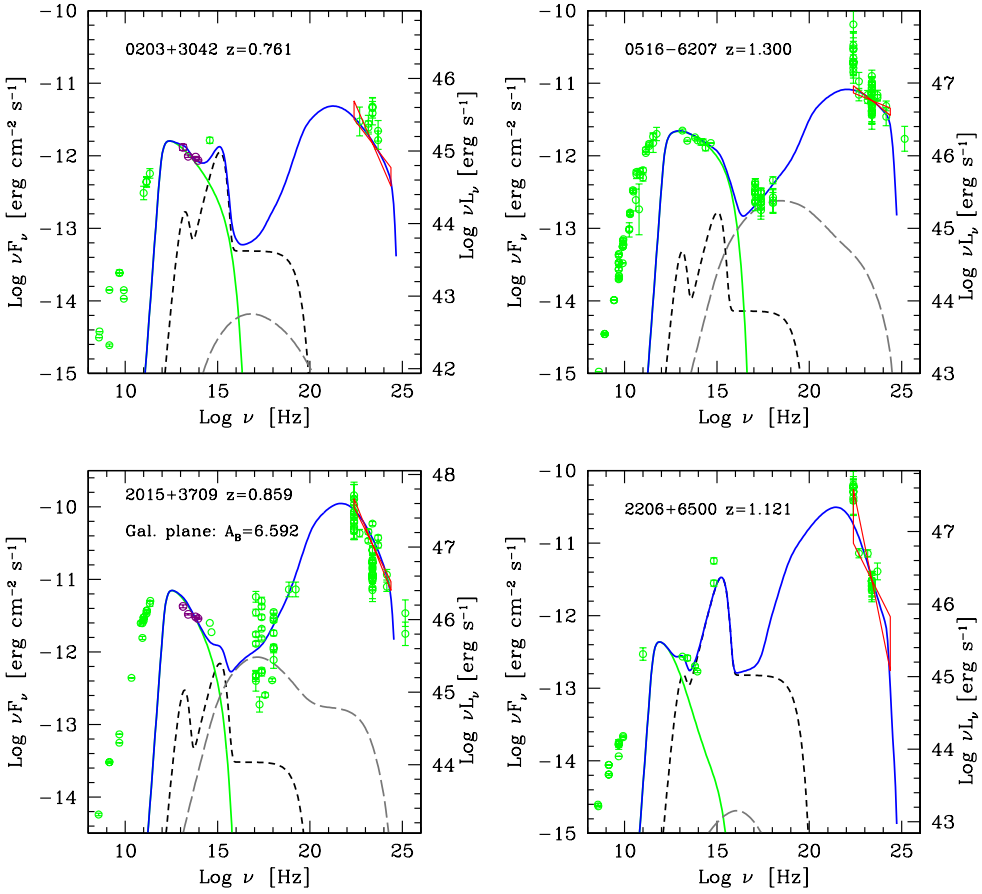

Figure A.1: Sources reclassified as FS.

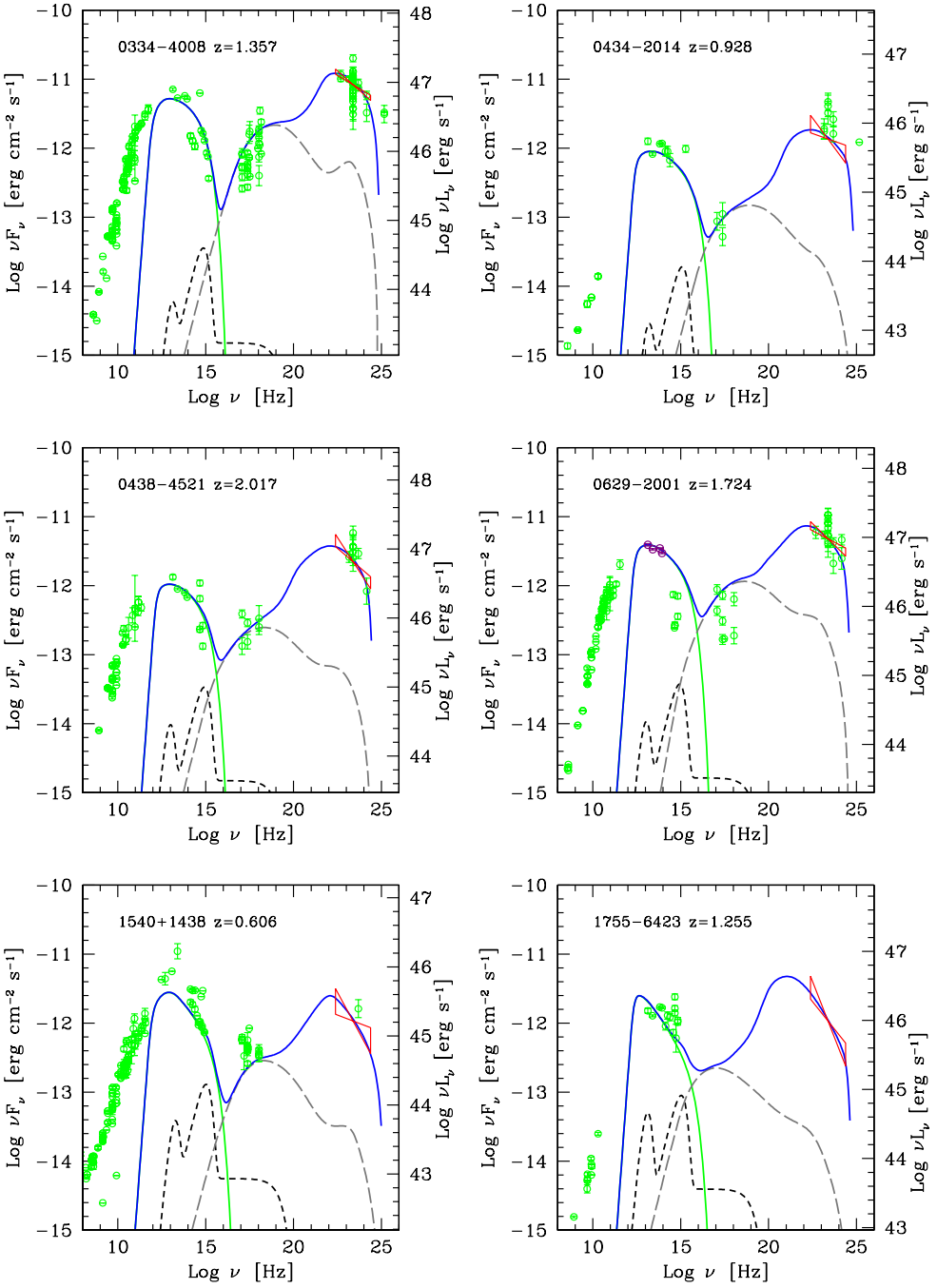

Figure A.2: Sources reclassified as BL/FS, with optical spectra showing weak broad emission lines, but SEDs more typical of FSRQs.

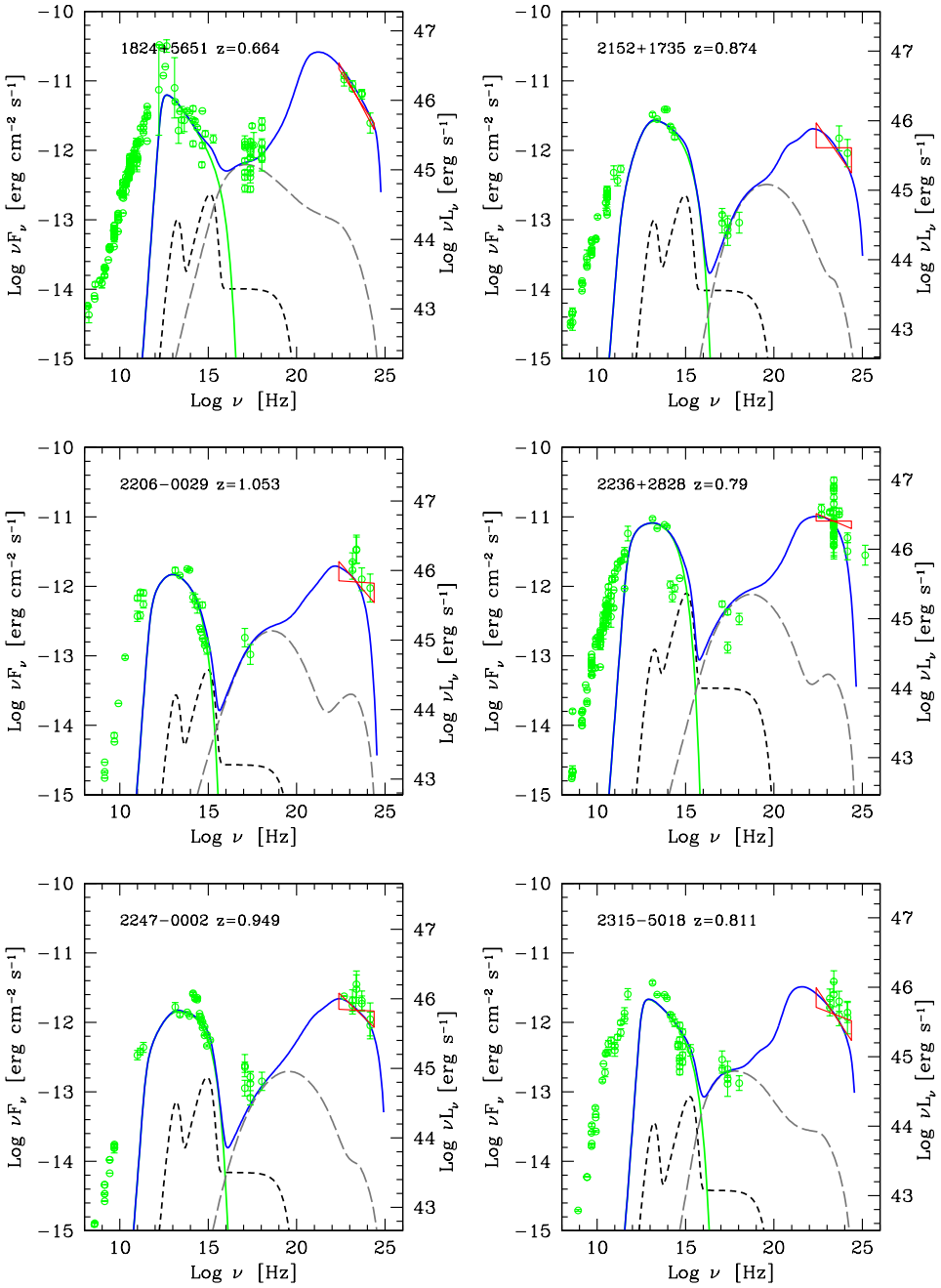

Figure A.3: Sources reclassified as BL/FS, with optical spectra showing weak broad emission lines, but SEDs more typical of FSRQs.

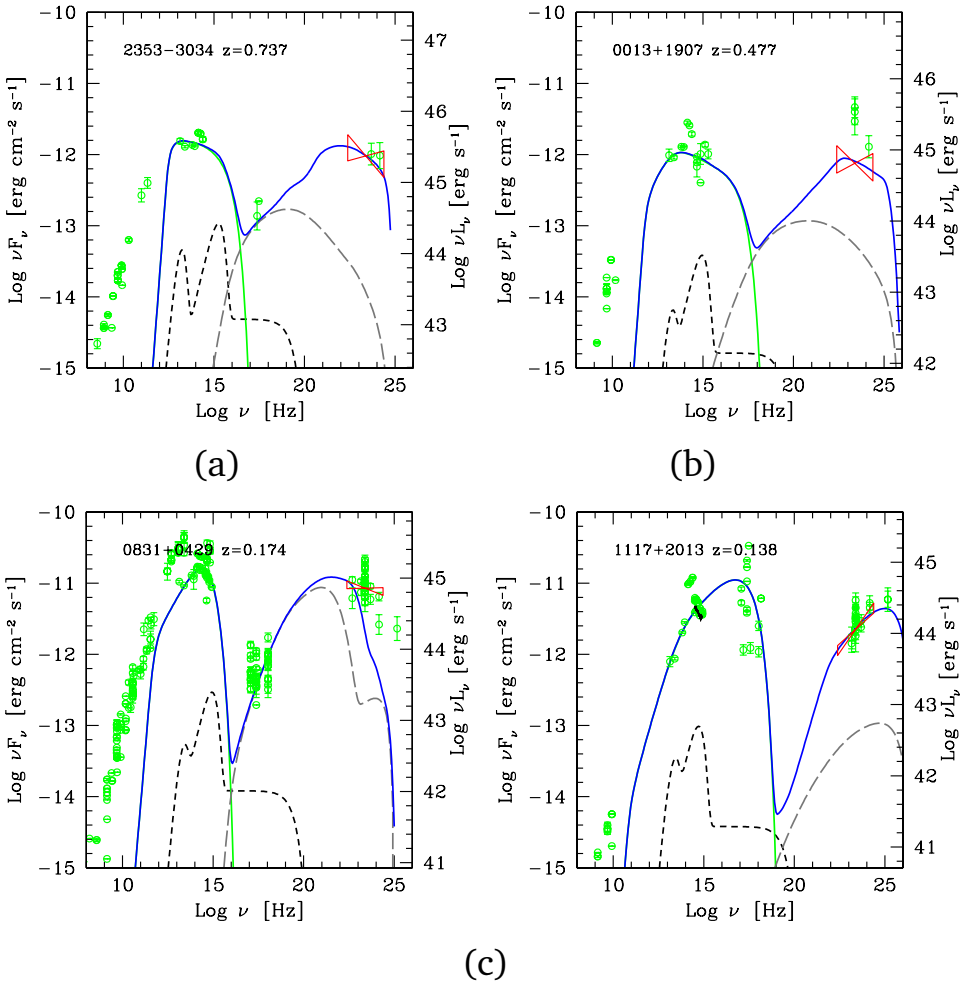

Figure A.4: (a) Source reclassified as BL/FS. (b,c) Sources that can be classified as BL Lacs, both from the optical spectra and from the SED aspect.

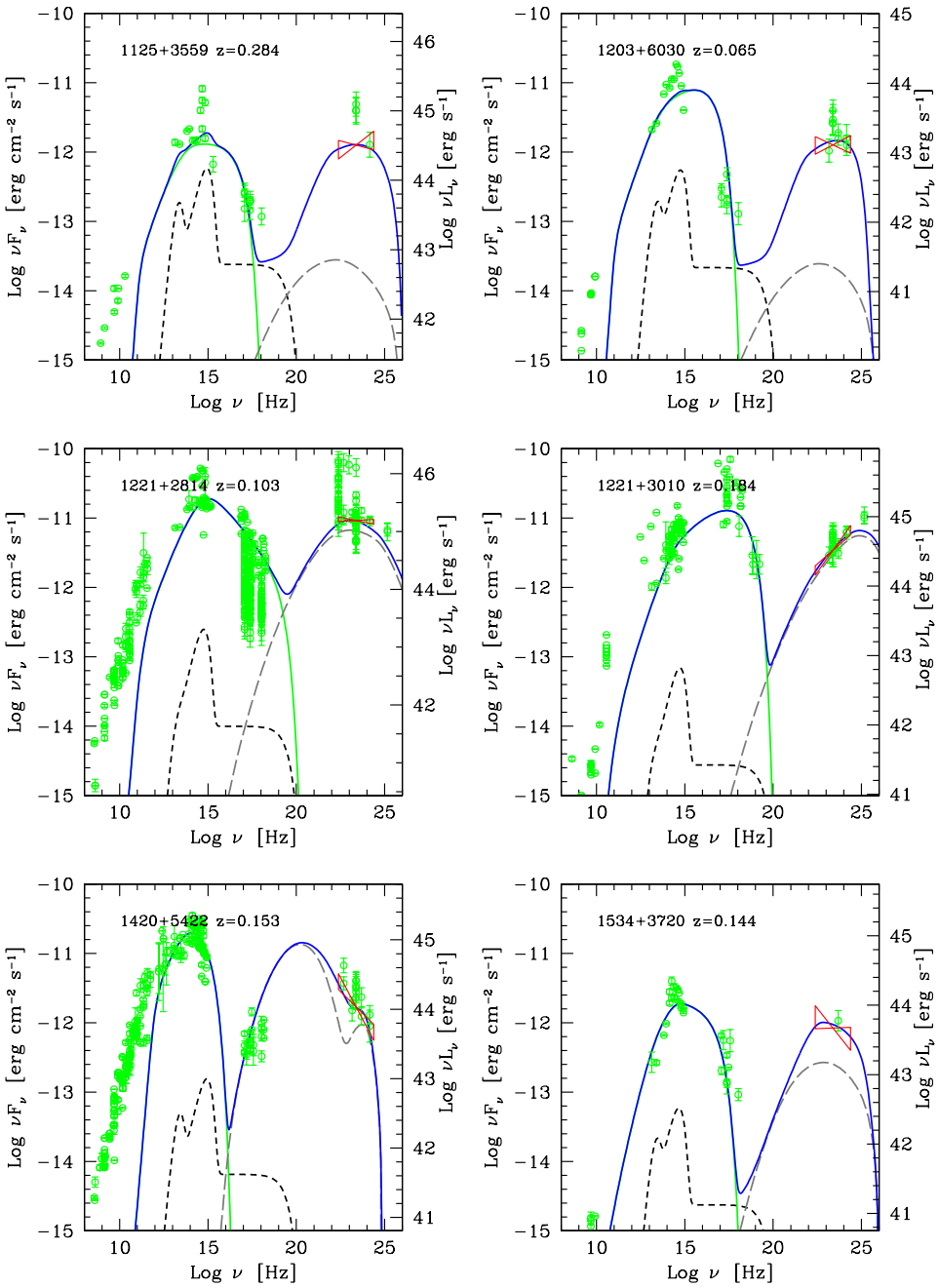

Figure A.5: Sources that can be classified as BL Lacs, both from the optical spectra and from the SED aspect.

B

SEDs of $z > 4$ blazar candidates

Figures B.1, B.2 and B.3 show the IR–optical–UV SEDs of the sample of 19 high–redshift, extremely radio–loud quasars described in Section 4.1, along with models of Shakura–Sunyaev accretion discs. The IR–optical–UV SED of B2 1023+25 is shown in Section 4.2 (Figure 4.2), to explain the details of data and fitting process.

In each figure, the black line is the SDSS spectrum. Red and magenta points are data from GROND and WISE, respectively. Green points are archival data (ASDC SED builder, NED). The grey stripe indicates the νL_ν peak luminosity of the disc. The blue line is the multicolor black body that best fits our data, calculated with L_d and M_BH values reported in each figure. Outside the range marked by the cyan lines, the disc model cannot fit satisfactory the data. Note that at $\log\nu > 15.4$ the models do not fit the data, because of the Lyα forest.

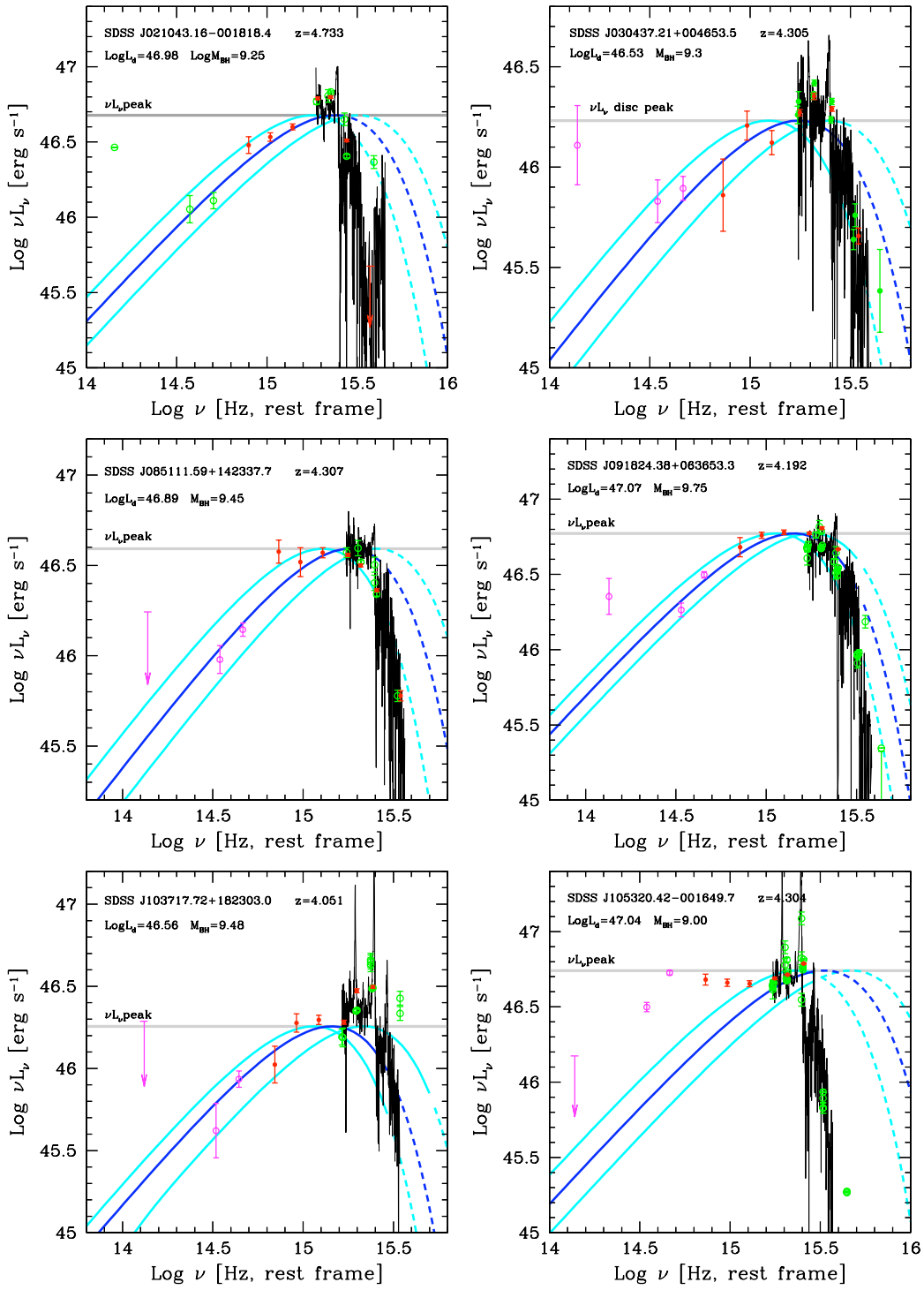

Figure B.1: IR–optical–UV SEDs of blazar candidates

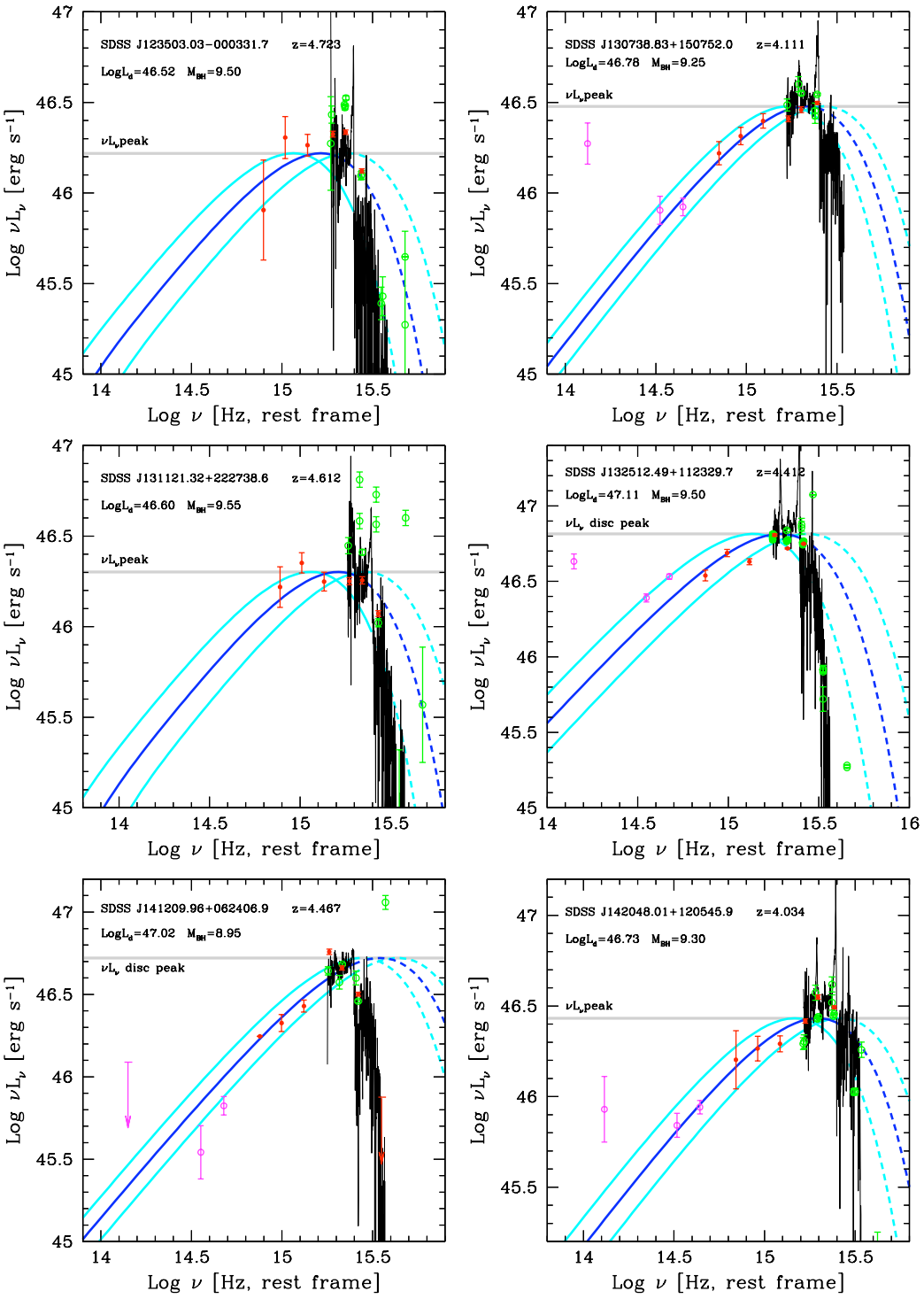

Figure B.2: IR–optical–UV SEDs of blazar candidates

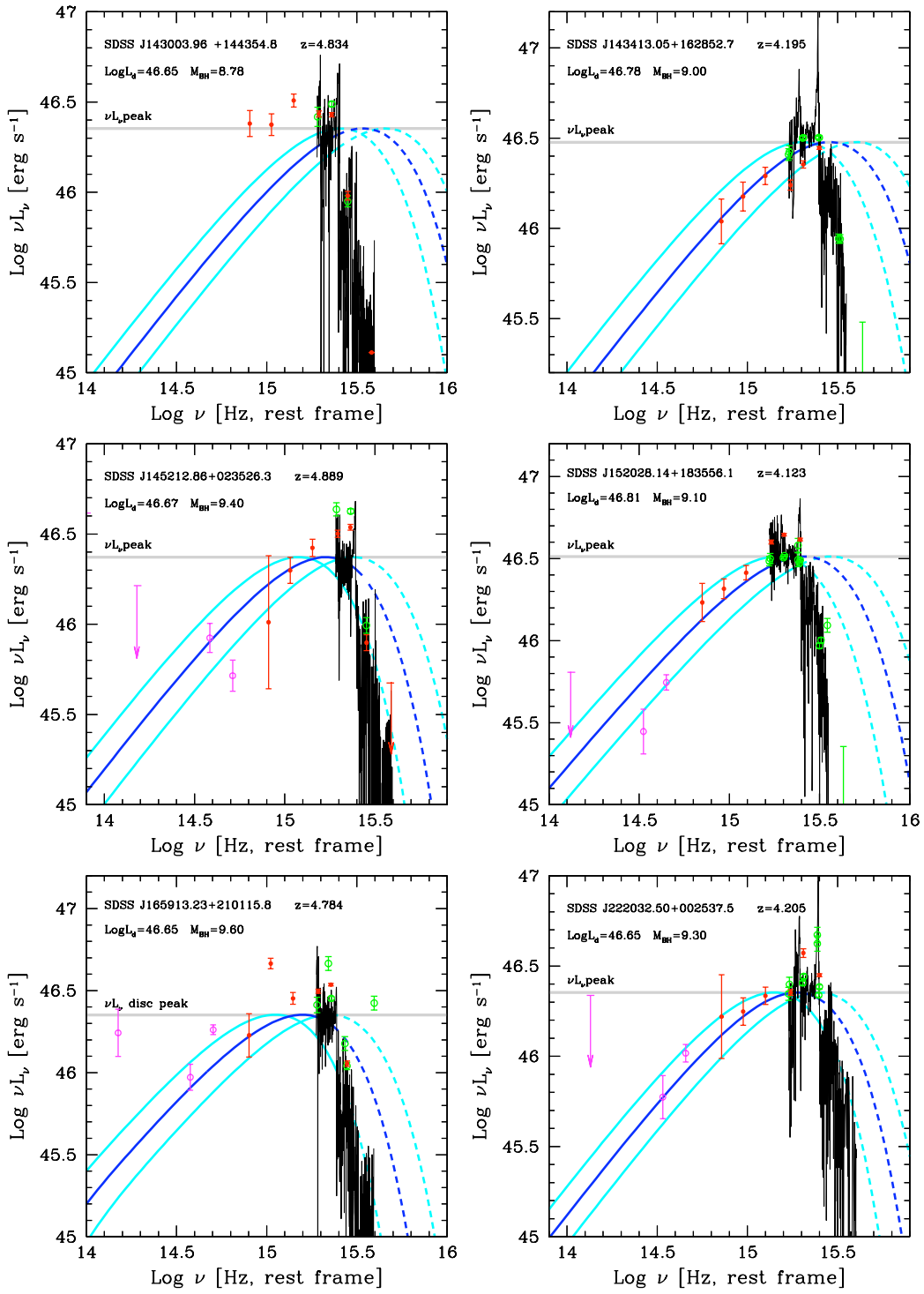

Figure B.3: IR–optical–UV SEDs of blazar candidates

Bibliography

Abdo A.A., Ackermann M., Ajello M., et al., 2010, ApJ, 715, 429

Abdo A.A., Ackermann M., Ajello M., et al., 2011, ApJ, 733, L26

Abramowicz M.A., Chen X., Kato S., et al., 1995, ApJ, 438, L37

Abramowicz M.A., Czerny B., Lasota J.P., Szuszkiewicz E., 1988, ApJ, 332, 646

Ackermann M., Ajello M., Allafort A., et al., 2011, ApJ, 743, 171

Antonucci R.R.J. & Cohen R.D., 1983, ApJ, 271, 567

Antonucci R.R.J. & Miller J.S., 1985, ApJ, 297, 621

Atwood W.B., Abdo A.A., Ackermann M., et al., 2009, ApJ, 697, 1071

Baars J.W.M., Genzel R., Paulini–Toth I.I.K., Witzel A., 1977, A&A, 61, 99

Balbus S.A. & Hawley J.F., 1991, ApJ, 376, 214

Baldwin J.A. & Netzer H., 1978, ApJ, 226, 1

Barthelmy S., Barbier L., Cummings J., et al., 2005, Space Sci. Rev., 120, 143

Bassett L.C., Brandt W.N., Schneider D.P., et al., 2004, AJ, 128, 523

Baum S.A. & Heckman T., 1989a, ApJ, 336, 681

Baum S.A. & Heckman T., 1989b, ApJ, 336, 702

Begelman M.C., 1979, MNRAS, 187, 237

Begelman M.C., Blandford R.D., Rees M.J., 1984, Rev. Mod. Ph., 56, 255

Begelman M.C. & Meier D.L.,1982, ApJ, 253, 873

Behar E., Dado S., Dar A., Laor A., 2011, ApJ, 734, 26

Bentz M.C., Peterson B.M., Pogge R.W., et al., 2006, ApJ, 644, 133

Bettoni D., Falomo R., Fasano G., Govoni F., 2003, A&A, 399, 869

Blandford R.D. & McKee C.F., 1982, ApJ, 255, 419

Blandford R.D. & Payne D.G., 1982, MNRAS, 199, 883

Blandford R.D. & Znajek R.L., 1977, MNRAS, 179, 433

Bondi H., 1952, MNRAS, 112, 195

Burrows D., Hill J., Nousek J., et al., 2005, Space Sci. Rev., 120, 165

Buttiglione S., Capetti A., Celotti A., et al., 2009, A&A, 495, 1033

Buttiglione S., Capetti A., Celotti A., et al., 2010, A&A, 509, 6

Calderone G., Ghisellini G., Colpi M., Dotti M., 2013, MNRAS, 431, 210

Calderone G., Sbarrato T., Ghisellini G., 2012, MNRAS, 425, L41

Cash W., 1979, ApJ, 228, 939

Celotti A. & Ghisellini G., 2008, MNRAS, 385, 283

Celotti A., Padovani P., Ghisellini G., 1997, MNRAS, 286, 415

Chen X., Abramowicz M.A., Lasota J.P., et al., 1995, ApJ, 443, L61

Chiaberge M., Celotti A., Capetti A., Ghisellini G., 2000, A&A, 358, 104

Colla G., Fanti C., Fanti R., et al., 1972, A&AS, 7, 1

Davidson K., 1972, ApJ, 171, 213

Decarli R., Dotti M., Treves A., 2011, MNRAS, 413, 39

Dermer C.D., 1995, ApJ, 446, L63

Donato D., Ghisellini G., Tagliaferri G., Fossati G., 2001, A&A, 375, 739

Edwards P.G. & Piner B.G., 2002, ApJ, 579, 67

Faber S.M., Dressler A., Davies R.L., et al., in Faber S.M. ed., *"Nearly Normal Galaxies: From the Planck Time to the Present*", Springer–Verlag, New York, p. 175

Faber S.M. & Jackson R.E., 1976, ApJ, 204, 668

Fanaroff B.L. & Riley J.M., 1974, MNRAS, 167, 31

Fender R., Belloni T., Gallo E., 2005, Ap&SS, 300, 1

Ferland G.J. & Mushotzky R.F., 1982, ApJ, 262, 564

Ferrarese L. & Merritt D., 2000, ApJ, 539, L9

Fossati G., Maraschi L., Celotti A., et al., 1998, MNRAS, 299, 433

Francis P.J., Hewett P.C., Foltz C.B., et al., 1991, ApJ, 373, 465

Frank J., King A.R., Raine D.J., 1985, *"Accretion Power in Astrophysics*" (Cambridge University Press)

Frey S., Fogasy J.O., Paragi Z., Gurvitis L.I., 2013, MNRAS, 431, 1314

Fruscione A., McDowell J.C., Allen GE., et al., 2006, Proc. SPIE, 6270, 62701V

Gehrels N., Chincarini G., Giommi P., et al., 2004, ApJ, 611, 1005

Genzel R., Eisenhauer F., Gillessen S., 2010, Rev. Mod. Phys., 82, 3121

Genzel R., Pichon C., Eckart A., et al., 2000, MNRAS, 317, 348

Georganopoulos M. & Kazanas D., 2004, ApJ, 604, 81

Ghirlanda G., Ghisellini G., Tavecchio F., et al., 2011, MNRAS, 413, 852

Ghisellini G. & Celotti A., 2001, A&A, 379, L1

Ghisellini G., Celotti A., Tavecchio F., et al., 2014a, MNRAS, 438, 2694

Ghisellini G., Della Ceca R., Volonteri M., et al., 2010a, MRAS, 405, 387

Ghisellini G., Haardt F., Della Ceca R., et al., 2013, MNRAS, 432, 2818

Ghisellini G., Sbarrato T., Tagliaferri G., et al., 2014b, MNRAS, 440, L111

Ghisellini G. & Tavecchio F., 2009, MNRAS, 397, 985

Ghisellini G., Tavecchio F., Chiaberge M., 2005, A&A, 432, 401

Ghisellini G., Tavecchio F., Foschini L., et al., 2010b, MNRAS, 402, 497

Ghisellini G., Tavecchio F., Foschini L, Ghirlanda G., 2011, MNRAS, 414, 2674

Giommi P., Padovani P., Polenta G., 2013, MNRAS, 431, 1914

Giommi P., Padovani P., Polenta G., et al., 2012, MNRAS, 420, 2899

Giovannini G., Taylor G. B., Arbizzani E., et al., 1999, ApJ, 522, 101

GIROLETTI M., GIOVANNINI G., FERETTI L., ET AL., 2004, ApJ, 600, 127

GREINER J., BORNEMANN W., CLEMENS C., ET AL., 2008, PASP, 120, 405

GUBBAY J., LEGG A.J., ROBERTSON D.S., ET AL., 1969, Nature, 224, 1094

HARRISON F.A., BOGGS S., CHRISTENSEN F., ET AL., 2010, SPIE, 7732, 21

HEALEY S.E., ROMANI R.W., TAYLOR G.B., ET AL., 2007, ApJS, 171, 61

ICHIMARU S., 1977, ApJ, 214, 840

KALBERLA P.M.W., BURTON W.B., HARTMANN D., ET AL., 2005, A&A, 440, 775

KASPI S., SMITH P.S., NETZER H., ET AL., 2000, ApJ, 533, 621

KATZ J., 1977, ApJ, 215, 265

KOMISSAROV S.S., 1990, SvA, 16, L284

KORMENDY J. & RICHSTONE D., 1995, ARA&A, 33, 581

KRÜHLER T., KÜPCÜ Y., GREINER J., ET AL., 2008, ApJ, 685, 376

LABIANO A., 2008, A&A, 488, L59

LAING R., 1993, in Burgarella D., Livio M., O'Dea C. eds., *"Astrophysical Jets*", Cambridge University Press, Cambridge, p. 95

LAING R.A., JENKINS C.R., WALL J.V., 1994, in Bicknell G.B., Dopita M.A., Quinn P.J. eds., *"The Physics of Active Galaxies*", ASP Conf. Ser., 54, 201

LYNDEN–BELL D. & PRINGLE J.E., 1974, MNRAS, 168, 603

MADAU P., HAARDT F., DOTTI M., 2014, ApJ, 784, L38

MAGORRIAN J., 1998, AJ, 115, 2285

MAHADEVAN R., 1997, ApJ, 447, 585

Maraschi L., Ghisellini G., Celotti A., 1992, ApJ, 397, L5

Marconi A., Axon D.J., Maiolino R., et al., 2008, ApJ, 678, 693

Marconi A., Axon D.J., Maiolino R., et al., 2009, ApJ, 698, L103

Marconi A. & Hunt L.K., 2003, ApJ, 589, L21

Meyer L., Ghez A.M., Schödel B., et al., 2012, Science, 338, 84

Miller J.S. & Goodrich B.F., 1986, Bull. Am. Astr. Soc., 18, 1001

Miyoshi M., Moran J., Herrnstein J., et al., 1995, Nature, 373, 127

Moran E.C. & Helfand D.J., 1997, ApJ, 484, L95

Morganti R., Tadhunter C.N., Dickson R., Shaw M., 1997, A&A, 326, 130

Narayan R., Garcia M.R., McClintock J.E., 1997, ApJ, 478, L79

Narayan R. & Yi I, 1994, ApJ, 428, L13

Narayan R. & Yi I., 1995a, ApJ, 444, 231

Narayan R. & Yi I., 1995b, ApJ, 452, 710

Nenkova M., Ivezić Ž., Elitzur M., 2002, ApJ, 685, 147

Nolan P.L., Abdo A.A., Ackermann M., et al., 2012, ApJS, 199, 31

Novikov I.D. & Thorne K.S., 1973, in DeWitt C. ed., *"Black Holes – Les Astres Occlus*", Gordon & Breach, New York, p. 346

Onken C.A., Ferrarese L., Merritt D., et al., 2004, ApJ, 615, 645

Oshuga K., Mori M., Nakamoto T., Mineshige S., 2005, ApJ, 628, 368

Owen F.N., Hardee P.E., Cornwell T.J., 1989, ApJ, 340, 698

Padovani P., Bonzini M., Miller N., et al., 2014, IAUS, 304, 79

Padovani P. & Giommi P., 1995, ApJ, 444, 567

Park D., Kelly B.C., Woo J.–H., Treu T., 2012, ApJS, 203, 6

Peterson B.M., 2014, Space Sci. Rev., 2014, 183, 253

Peterson B.M., Wagner R.M., Crenshaw K.A., et al., 1983, AJ, 88, 926

Piner B.G. & Edwards P.G., 2004, ApJ, 600, 115

Plotkin R.M., Markoff S., Trager S.C., Anderson S.F., 2011, MNRAS, 413, 805

Rawlings S. & Saunders R., 1991, Nature, 349, 138

Rawlings S., Saunders R., Eales S.A., Mackay C.D., 1989, MNRAS, 240, 701

Rees M.J., 1966, Nature, 211, 468

Rees M.J., Begelmann M.C., Blandford R.D., Phinney E.S., 1982, Nature, 295, 17

Rybicki G.B. & Lightman A.P., 1985, *"Radiative Processes in Astrophysics*" (Wiley–VCH ed.)

Richards G.T., Lacy M., Storrie–Lombardi L.J., et al., 2006, ApJS, 166, 470

Richards J.L., Max–Moerbeck W., Pavlidou V., et al., 2011, ApJS, 194, 29

Romani R.W., 2006, AJ, 132, 1959

Romani R.W., Sowards–Emmerd D., Greenhill L., Michelson P., 2004, ApJ, 610, L9

Roming P., Kennedy T., Mason K., et al., 2005, Space Sci. Rev., 120, 95

SALPETER E.E., 1964, ApJ, 140, 796

SAULT R.J., TEUBEN P.J., WRIGHT M.C.H., 1995, ASPC Series (eds. R.A. Shaw, H.E. Payne, and J.J.E. Hayes), 77, 433

SBARRATO T., GHISELLINI G., MARASCHI L., COLPI M., 2012a, MNRAS, 421, 1764

SBARRATO T., GHISELLINI G., NARDINI M., ET AL., 2012b, MNRAS, 426, L91

SBARRATO T., GHISELLINI G., NARDINI M., ET AL., 2013a, MNRAS, 433, 2182

SBARRATO T., GHISELLINI G., TAGLIAFERRI G., ET AL., 2014a, MNRAS, *in press*, [arXiv:1410.0364]

SBARRATO T., PADOVANI P., GHISELLINI G., 2014b, MNRAS, 445, 81

SBARRATO T., TAGLIAFERRI G., GHISELLINI G., ET AL., 2013b, ApJ, 777, 147

SBARUFATTI B., TREVES A., FALOMO R., 2005, ApJ, 635, 173

SCHLAFLY E.F. & FINKBEINER D.P., 2011, ApJ, 737, 103

SCHNEIDER D.P., RICHARDS, G.T., HALL P.B., ET AL., 2010, AJ, 139, 2360S

SEYFERT C.K., 1943, ApJ, 97, 28

SHAKURA N.I. & SUNYAEV R.A., 1973, A&A, 24, 337

SHAPIRO S.L., LIGHTMAN A.P., EARDLEY D.M., 1976, ApJ, 204, 187

SHAPIRO S.L. & TEUKOLSKY S.A., 1983, *"Black Holes, White Dwarfs and Neutron Stars* (Wiley Interscience)

SHARMA P., QUATAERT E., HAMMET G.H., STONE J.M., 2007, ApJ, 667, 714

SHAW M.S., ROMANI R.W., COTTER G., ET AL., 2012, ApJ, 748, 49

SHAW M.S., ROMANI R.W., COTTER G., ET AL., 2013, ApJ, 764, 135

SHEMMER O., BRANDT W.N., SCHNEIDER D.P., ET AL., 2006, ApJ, 644, 86

SHEMMER O., BRANDT W.N., VIGNALI C., ET AL., 2005, ApJ, 630, 729

SHEN Y., RICHARDS G.T., STRAUSS M.A. ET AL., 2011, ApJS, 194, 45

SIKORA M., BEGELMAN M.C., REES M.J., 1994, ApJ, 421, 153

SKRUTSKIE M.F., CUTRI R.M., STIENING R., ET AL., 2006, AJ, 131, 1163

SMITH J.A., TUCKER D.L., KENT S., ET AL., 2002, AJ, 123, 2121

SMITH M.G., CARSWELL R.F., WHELAN J.A.J., ET AL., 1981, MNRAS 195, 437

STALEVSKI M., FRITZ J., BAES M., ET AL., 2012, MNRAS, 420, 2756

SWAIN M.R., BRIDLE A.H., BAUM S.A., 1998, ApJ, 507, 29

TCHEKHOVSKOY A., NARAYAN R., MCKINNEY J.C., 2011, MNRAS, 418, L79

TERASHIMA Y. & WILSON A.S., 2003, ApJ, 583, 145

THORNE K.S., 1974, ApJ, 191, 507

TODY D., 1993, Astronomical Data Analysis Software and Systems II, 52, 173

TRUMP J.R., IMPEY C.D., KELLY B.C., ET AL., 2011, ApJ, 733, 60

ULRICH M.–H., BOKSENBERG A., PENSTON M.V., ET AL., 1991, ApJ, 382, 483

URRY C.M. & PADOVANI P., 1995, PASP, 107, 803

VANDEN BERK D.E., RICHARDS G.T., BAUER A., ET AL., 2001, AJ, 122, 549

VESTERGAARD M. & PETERSON B.M., 2006, ApJ, 641, 689

VIGNALI C., BRANDT W.N., SCHNEIDER D.P., KASPI S., 2005, AJ, 129, 2519

VOGES W., ASCHENBACH B., BOLLER T., ET AL., 1999, A&A, 349, 389

Volonteri M., Haardt F., Ghisellini G., Della Ceca R., 2011, MNRAS, 416, 216

Ward M.J., Wright G., Blanco P., 1988, UKIRT Newsletter, 18

White R.L., Becker R.H., Helfand D.J., Gregg M.D., 1997, ApJ, 475, 479

Willott C.J., Rawlings S., Blundell K.M., Lacy M., 1999, MNRAS, 309,1017

Woo J.-H., Treu T., Barth A.J., et al., 2010, ApJ, 716, 269

Worsley M.A., Fabian A.C., Celotti A., Iwasawa K., 2004, MNRAS, 350, L67

Wu J., Brandt W.N., Miller B.P., et al., 2013, ApJ, 763, 109

York D.G., Adelman J., Anderson J.E., et al., 2000, AJ, 120, 1579

Young M., Elvis M., Risaliti G., 2009, ApJS, 183, 17

Yuan W., Fabian A.C., Worsley M.A., McMahon R.G., 2006, MNRAS, 368, 985

Yuan W., Matsuoka M., Wang T., et al., 2000, ApJ, 545, 625

Zickgraf F.–J., Voges W., Krautter J., et al., 1997, A&A, 323, L21

Acknowledgement

Time has come for the warmest "Thank you". These lines will randomly be in Italian or English, so that everyone will be able to understand enough.

Arriva finalmente il momento per ringraziare. Il percorso (per me tanto importante) che mi ha portata a poter scrivere quest'ultima pagina non sarebbe stato percorribile senza l'aiuto, l'appoggio e la presenza di alcune persone.

Innanzitutto, desidero ringraziare di cuore i miei relatori. Un primo, sentito, Grazie va a Gabriele Ghisellini, che ha continuato sin dalla tesi triennale a starmi accanto, mostrandomi il vero divertimento della ricerca, e la passione intensa con cui la si puo' affrontare. Accanto a lui voglio ringraziare Paolo Padovani, che in un anno ha saputo trasmettermi molto più di quanto io potessi sperare, permettendomi di conoscere un ambiente di ricerca del tutto nuovo, e trasmettendomi una passione ancora diversa, più pratica, intrisa di lavoro frenetico. Grazie a entrambi, perché è per merito vostro che mi posso sentire tanto soddisfatta di questi tre anni e di queste pagine.

Un ringraziamento particolare inoltre lo devo a Gianpiero Tagliaferri, per quanto mi ha aiutata ed ha contribuito a questa tesi.

Un grosso Grazie va al neo–rinominato (con tanto di blog) High–Energy Astrophysics Group. Fabrizio, Giancarlo e Luigi: grazie per le tante discussioni, i commenti e il grande aiuto di questi anni. Francesco (che ringrazio di esistere), Alessio e Om: continuate così, grazie anche per tutte le risate.

Un pensiero speciale va al buon Giorgio, che anche se ora è finalmente riuscito ad avvicinarsi al mare, rimarrà sempre il mio primo colleguccio: torna presto!

Grazie a tutti i "Meratesi" per i pranzi, le risate e i pettegolezzi: tutti quanti, con in testa Grazia LaCri e Perri, siete stati la luce perfetta anche in mezzo alle giornate più storte e piene di nervosismo delle ultime settimane.

A fast jump into English, to be able to thank properly the amazing people that I met in my year at ESO. Those months literally flew in front of me, but I'm happy and proud, since I had the opportunity to meet beautiful and rich people, that will always stay in my hearth. Thanks Bitten for being such a good friend. Thanks Clau for showing me how strong and amazing a woman can be. Thanks Kate, Anna, Marco, Alice, Laura, Maud, Izaskun, Rodrigo, Tim, Neale, Grant and Stephan for the teas, the dinners, the nights out, Oktoberfest and Starkbierfest: it was a very good year! And thanks to everyone else that made this year unforgettable.

Torno di nuovo all'italiano, perchè tutti questi passi in mezzo alla ricerca non sarebbero comunque stati possibili senza l'appoggio dei miei amici più cari, che mi hanno supportata e sopportata in ogni momento, nonostante ogni tanto mi butti in discorsi entusiasti sui buchi neri, che finiscono quando le ore non sono più nemmeno troppo piccole, di mattina. Per questo abbraccio Chiara e Martina, insostituibili mie risate e coscienza da ormai molti anni: grazie. Lascio qui degli abbracci anche per Paolo e Stefano, e per Federico: chi da vicino, chi per telefono, chi da oltremanica mi sa far perdere nelle risate più incredibili e deliranti. Le serate fra donne con anche Fede e Ila mettono le risate finali a questi abbracci.

I meandri della Bicocca mi hanno permesso di muovere i primi passi accademici insieme a delle persone speciali, che anche qui voglio ricordare: Pozz e i nostri percorsi sempre vicini (ed il tuo dottorato in dirittura d'arrivo), Davide e i tanti esami fatti insieme, il buon Freddi e i nostri aperitivi, la Piccola Eli, Giorgia.

Lascio per ultimi i ringraziamenti dettati dal cuore. Voglio ringraziare Ago, il mio sorriso, per aver portato tanta gioia e sicurezza nella mia vita. Non pensavo di poter essere così felice, e ti ringrazio per avermelo fatto capire. Grazie di essermi stato accanto in questi ultimi mesi stressanti, ed avermi aiutata a superare la nostalgia durante i mesi tedeschi. Grazie per avermi camminato accanto, e grazie per volerlo fare ancora.

Infine, il pensiero più importante va ai miei genitori. Grazie per avermi insegnato a credere nei miei progetti, nonostante sembrino strani, difficili e lontani. Grazie per avermi sostenuta incondizionatamente, anche se a volte vi ringhio addosso stanchezza e stress. So di potermi affidare sempre al vostro amore. Grazie di avermi messo su questa emozionante ed insolita strada, affiancandomi in una scelta inusuale e apparentemente non facile, ma tanto appagante. Grazie per avermi reso la persona che sono.
Questa tesi è per voi.